# MSc Thesis

## Sensitivity study on a Reverse turbo-Brayton cryocooler for zero boil-off on an airborne liquid hydrogen tank

Thomas Britting

Delft University of Technology

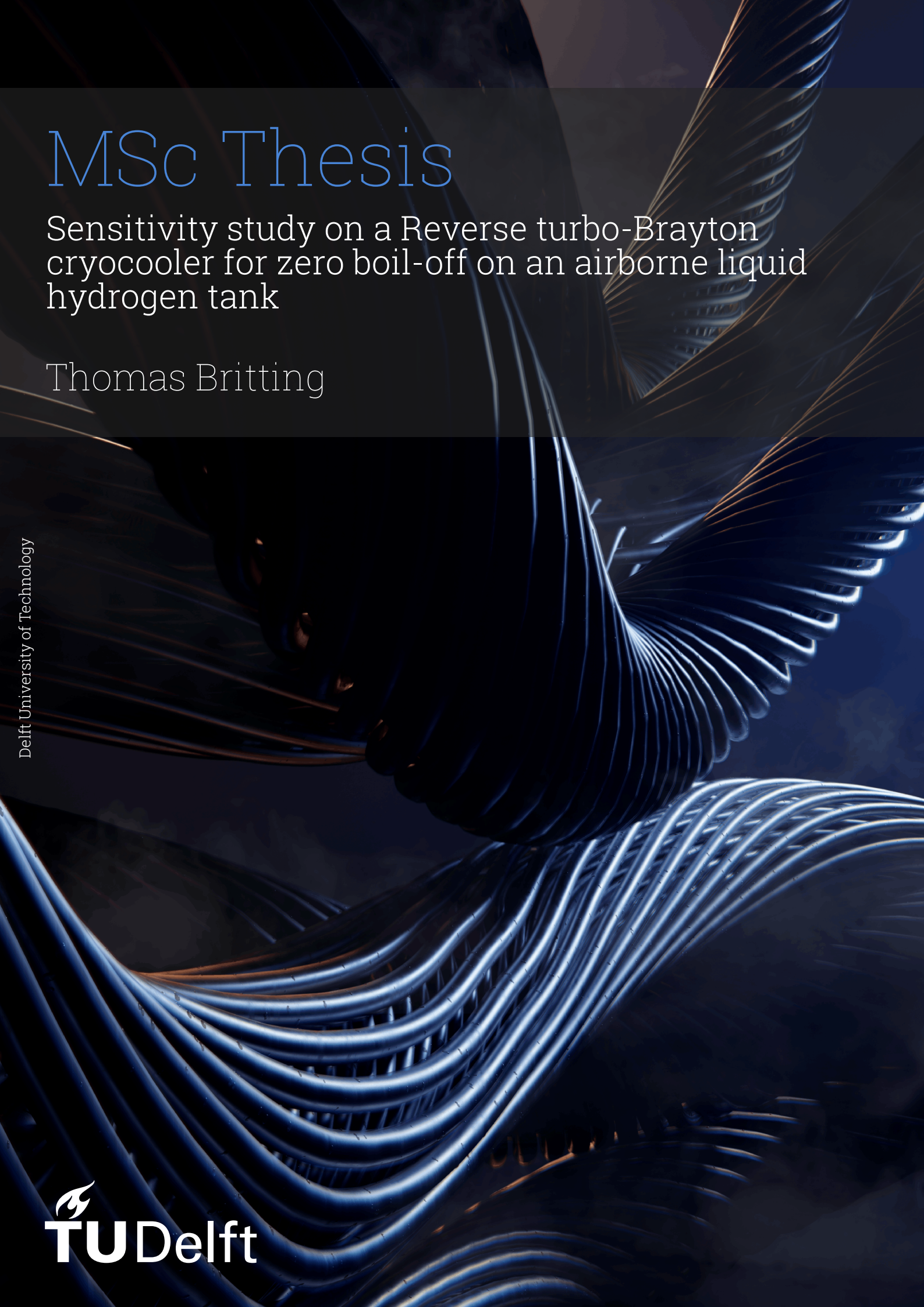

TU Delft

# MSc Thesis

## Sensitivity study on a Reverse turbo-Brayton cryocooler for zero boil-off on an airborne liquid hydrogen tank

by

Thomas Britting

Student number: 4554116

In partial fulfilment of the Master of Sciences at TU Delft.

| | |
|---|---|
| Instructor: | Prof. dr. ir. C. De Servi (TU Delft) |
| Teaching Assistant: | F. Beltrame (TU Delft) |
| Faculty: | Faculty of Aerospace Engineering, Delft |
| Thesis committee: | Prof. dr. ir. C. De Servi (TU Delft) |
| | Prof. dr. ir. M. Pini (TU Delft) |
| | Prof. dr. ir. A. Cervone (TU Delft) |

TU Delft

# Preface

This thesis marks the end of my time as a student at the TU Delft aerospace faculty. I would like to thank all the people that made it possible for me pursue this path and aided in my personal development throughout the years. Particularly my roommates, parents, and the people at DARE who have always supported me.

*Thomas Britting*
*Delft, May 2024*

# Table of contents

# Sensitivity study on a Reverse turbo-Brayton cryocooler for zero boil-off on an airborne liquid hydrogen tank

**Thomas Britting**

Delft University of Technology, 2629HS Delft, the Netherlands

Liquid hydrogen has been identified as a low-emission alternative to hydrocarbon fuel sources for aircraft. Although there has been a notable increase in the number of studies and technology readiness of liquid hydrogen technologies in the recent decade, there is still more research and development necessary to realize commercially viable hydrogen-fueled aviation. Achieving zero boil-off by using active cooling has been identified as a potential method of decreasing the mass and volume of a future liquid hydrogen fueled aircraft. However the lack of literature or data on the thermal performance and specific power of cryocoolers for this application makes it difficult to assess its feasibility. Therefore, a study was performed to develop a reverse turbo-Brayton cryocooler simulation tool, focused on the three heat exchangers of this cooler type. This paper presents the methodology for the development of this tool alongside a case study on a liquid hydrogen fuel tank for TU Delft's flying-V concept. From the case study it has been concluded that the considered RTBC design offers a reduction in the liquid hydrogen mass, however not significant enough to offset the cryocooler's own weight. An improved performance and specific power of the individual components would be required to achieve a net weight reduction.

## Introduction

The use of liquid hydrogen as a fuel source for aircraft has already been demonstrated by project Bee in the 1950s, when a B-57 aircraft was modified to use liquid hydrogen intermittently during flight as a technology demonstrator.[1] Later, in the 1980s, a modified Tu-155 flew using liquid hydrogen during parts of its flights.[2] However the use of liquid hydrogen as sole fuel source for aircraft is still very much a new and untested concept. There have been numerous studies on conceptual liquid hydrogen aircraft such as for example a liquid hydrogen variant of TU Delft's flying-V.

The use of cryocoolers to cool a liquid hydrogen tankto achieve zero boil-off (ZBO) for liquid hydrogen in itself has already been demonstrated multiple times in recent decades. NASA has, for example, performed a series of test programs where a pulse-tube cryocooler was used to prevent boil-off in a well-insulated liquid hydrogen tank.[3][4][5] One of the major challenges is to effectively distribute the cooling power over the volume of the liquid hydrogen. The low thermal conductivity of fluids at cryogenic temperatures and the drawbacks associated with the installment of a mixer make it challenging to provide effective cooling, especially for large tanks. In 2012, NASA modified an existing 125000 liter liquid hydrogen tank by installing a tubular heat exchanger inside.[6] Zero boil-off was achieved by connecting the tank's heat exchanger to a commercially available RTBC using helium as the working fluid.[7] This project, called the Ground Operations Demonstration Unit (GODU), demonstrated the feasibility of achieving zero boil-off for liquid hydrogen in large tanks and has been one of the most relevant references for this study.

Although cryocoolers have not yet been used to achieve ZBO on aircraft fuel tanks, few cryocoolers have already found use onboard aircraft for different applications, for example, pulse-tube coolers for the optical instruments of the SOFIA airborne telescope,[8] an RTBC for in-flight air liquefaction,[9] or coolers for optical sensors. Cryocoolers have been used more frequently on satellites, primarily to cool optical sensors. These have been almost exclusively reciprocating cryocoolers, such as pulse-tube coolers. However there have also been experiments with the use of sorption,[10] adiabatic demagnetization,[11] and reverse Brayton coolers. A notable case of the latter is the NICMOS reverse turbo-Brayton cooler by Creare, a research and development firm, that was installed on the Hubble space telescope. This represents the first use of an RTBC on a spacecraft.[12] Apart from

supplying cooling power to small dewars, no large scale zero boil-off experiments have been done in space, to the author's knowledge. However, the importance and need for such a technology for future space exploration has been highlighted by multiple organizations, including but not limited to NASA[13] and ESA.[14]

Achieving zero boil-off in large fuel tanks without mixer requires distributed cooling. Reciprocating coolers such as pulse-tube, Stirling, or Gifford-McMahon coolers only provide localized cooling. Cryocoolers that operate in a continuous cycle are much better suited for the purpose of providing cooling to large fuel tanks. Sorption and Joule-Thomson coolers are typically used for small scale applications due to their low efficiency and specific power. Reverse turbo-Brayton cryocoolers have been identified as a more effective way to achieve ZBO for large volumes and heat loads. The reason is that their specific power and efficiency scales well with increasing cooling power, even at low temperatures near the boiling point of hydrogen.[15]

Among the components of an RTBC, the recuperator is the most critical with respect to the cooler's specific power and coefficient of performance (COP). RTBC recuperator effectiveness values are typically in the high 90 percentages in order to avoid large pressure ratios that lead to low COP and high temperatures on the compressor side of the cycle. The study by Qian et al.[16] identified that the majority of RTBCs use plate-fin heat exchangers[9171819] or coil-wound heat exchangers[15] as recuperator. However the use of shell-tube HEXs,[20] stacked plate HEXs,[21] and slotted plate HEXs[22] as recuperators for RTBCs have also been demonstrated. For the present study, a counter-flow coil-wound heat exchanger (CWHEX) was chosen for its ability to handle high pressure differences and large temperature gradients. The coiling of the tubes inside a CWHEX is advantageous to cope with large temperature difference as it reduces the effects of differential thermal expansion and longitudinal heat conduction through the tube walls.

## 1. Previous research

This section provides a highlight of the current state of the art RTBC technology and ongoing research.

First of all, a literature survey was performed to identify the typical operational regimes, efficiencies, and specific power of the different types of cryocoolers that are commercially available or currently under development. Fig. 1 and Fig. 2 show their performance as function of the cold end temperature for five common types of cryocoolers. This data is generally in good agreement with surveys carried out by other authors such as that of ter Brake,[23] which expanded upon the one from Strobridge.[24] An in-depth analysis and discussion of the results of this cryocooler survey can be found in Section 3.3 of the literature study report that is attached to this document.

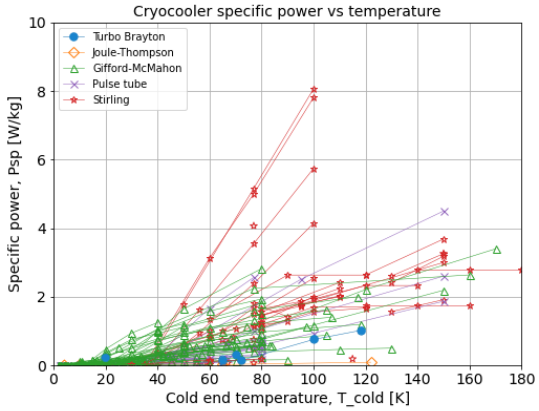


Fig. 1: Specific power for different types of cryocoolers as function of the load temperature.

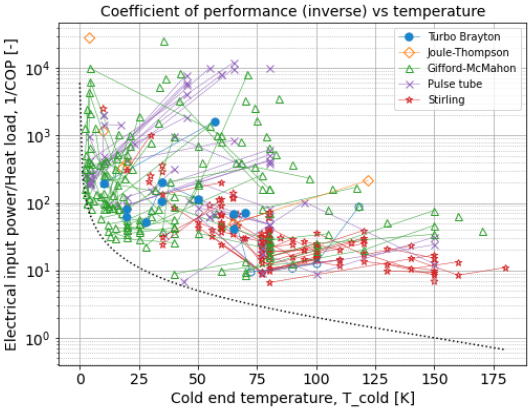


Fig. 2: Inverse of the coefficient of performance (1/COP) for different types of cryocoolers as function of the load temperature. The dotted line represents the maximum possible efficiency using a perfect Carnot cycle.

### 1.1 Reverse Turbo-Brayton Cryocoolers

A significant amount of research has been published by M. V. Zagarola and colleagues on the development of RTBCs at Creare. Over the last decades, they have developed multiple RTBCs for different applications, including that for the Hubble space telescope.[12] Several of their publications highlight the advancements on individual components of RTBCs such as the turbomachinery,[25,26] recuperators,[22,20] and bearings.[27] Additionally Creare has also been active with the development of RTBCs to achieve ZBO onboard future spacecraft as a technology demonstrator.[28]

Although Creare has been at the forefront of RTBC development, it is not the only institution that has successfully developed RTBCs. Several recent papers present the development of a cryogenic RTBC in China, such as that described by Chen et al.[29] and by Yang et al.[18,19] In 2020, K. Lee et al. also published on the development of a 1.35 kW RTBC with a lower temperature of 77K for superconducting cables by the Japanese company Taiyo Nippon Sanso.[17] Air Liquide has also been developing large RTBCs with heat loads in the order of several kilowatt for industrial use.[30] Additionally, Linde produces piston-based compression RTBCs (e.g. LR1620 and LR1420), of which one was used for NASA's liquid hydrogen ZBO GODU experiment.[7] With the exception of the Creare RTBCs, the aforementioned cryocoolers were designed for ground operations where the power efficiency of the cooler is the key design target rather than the specific power. To the author's knowledge, there are no RTBCs that were optimized for airborne applications with exception for those developed by Creare that are designed for orbital applications.

### 1.2 Recuperative cryogenic heat exchangers

As mentioned in subsection 1.1, different types of recuperators have been used in RTBCs. Plate-fin HEXs and coil-wound heat exchangers (CWHEX) have been the most common. CWHEXs have often been used for industrial large scale LNG liquefaction facilities, especially for their ability to effectively deal with high differential pressures and large temperature gradients. Therefore CWHEX technology has been selected for the recuperator of the RTBC in this study.

Heat exchangers have been studied for a long time. Handbooks such that of Shah and Sekulic provide a complete and detailed overview of the design and simulation methods for heat exchangers.[31] The design of heat exchangers for cryogenic applications typically involves several challenges related to the relatively high share of thermal losses occurring at low temperatures and the large temperature differences along the flow path. The study by Pacio and Dorao[32] provides a detailed overview of the typical design considerations and modeling approaches of cryogenic heat exchangers. They identify the following four effects that contribute most towards the ineffectiveness of cryogenic heat exchangers:

- Change in fluid properties
- Flow maldistribution
- Longitudinal heat conduction
- Heat exchange with the environment

In their review, Pacio and Dorao concluded that most studies in the literature focus on the modeling of a single loss source and only few include two or more.[32]

With the increased demand for LNG and other cryogenic fluids in recent decades, there has been a rise in the number of publications on CWHEXs. Several recent papers present their approach towards the modeling of CWHEXs for cryogenic applications. For example, Wang et al.[33] published a paper on the use of a distributed parameter model to simulate a LNG CWHEX with multiple flow circuits. Several other authors have resorted to the use of computational fluid dynamics to calculate the CWHEX performance, such as for example the study by Ren et al.[34] A discretized numerical model of CWHEXs has also been described in several papers, such as the one by by Hosseinian et al.[35] The methodology of the present study is similar that of Abolmaali and Afshin[36] where the effects of longitudinal heat conduction, change in fluid properties, and heat transfer with the environment are taken into account.

### 1.3 Zero boil-off heat exchangers

Significant progress has been made on the development of heat exchangers to achieve zero boil-off in cryogenic fuel tanks. One of the major challenges of designing such a heat exchanger is the temperature stratification of the fluid as a consequence of the low thermal conductivity of the cryogenic fluid. Since the end of the twentieth century, NASA has been performing several ground test campaigns to prove the feasibility of zero boil-off for liquid hydrogen fuel tanks using reciprocating cryocoolers.[3,4,5] The use of reciprocating cry-

ocoolers is however not favorable for large fuel tanks. Several studies have indicated that distributed cooling is preferential for large cryogenic fuel tanks.[15] The feasibility of ZBO in large liquid hydrogen fuel tanks was successfully demonstrated by NASA's GODU experiment, where a distributed tubular heat exchanger was installed inside a 125000 liter liquid hydrogen tank. In this experiment, an RTBC was used to supply helium as a cooling fluid.[6]

## 2. Methodology

The aim of this study is to provide an estimate for the specific power and COP of an RTBC for a liquid hydrogen aircraft fuel tank to assess the feasibility of zero boil-off. In order to calculate these performance parameters, an RTBC model was created that simulates the reverse turbo-Brayton cycle. The cycle can be represented by six thermodynamic states, as shown in Fig. 3. This figure also indicates the different loss sources that cause deviations from an ideal reverse turbo-Brayton cycle. The process between each point is modeled by separate programs that corresponds to the representative components, as explained below.

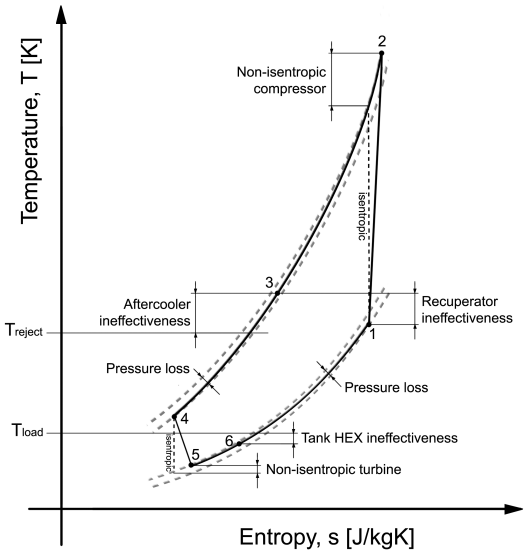


Fig. 3: Temperature-entropy diagram of a non-ideal reverse turbo-Brayton cycle, highlighting the different loss sources

- 1-2: Non-isentropic compression by compressor
- 2-3: Heat rejection to the environment by a HEX, called as aftercooler
- 3-4: Heat rejection on the hot side of recuperator
- 4-5: Non-isentropic expansion in a turbine
- 5-6: Heat absorption by the tank heat exchanger
- 6-1: Heat absorption by cold side of recuperator

The following set of variables is provided as an input to the RTBC model:

- Heat duty of the RTBC
- Turbine pressure ratio
- Turbomachinery isentropic efficiencies
- Maximum length of the recuperator
- Pressure at point 3
- Geometry of the recuperator (except for its length)
- Effectiveness of the recuperator
- Effectiveness of the aftercooler
- Length and inner radius of the fuel tank
- Fluid media that are used for the cooling fluid, tank fluid, and environment
- Properties of the materials used for the realization of the RTBC components
- Temperature and pressure of the fluid in the tank
- Environmental conditions

The RTBC model described in this chapter is based on several assumptions. First of all, the model assumes the steady state operation of the RTBC. Furthermore, at each stage of the cycle the fluid and flow properties are assumed to be uniform and represent a local average. The piping between the different components is not included in the current model. Hence the associated heat leak and hydraulic resistance are neglected. Gravitational effects can also be neglected due to the low density of the working fluid (helium) and small height differences in the circuit. These assumptions apply to the whole RTBC model, however the assumptions that are used to simulate the individual components are mentioned in the respective sections below.

### 2.1 RTBC analytical model

An analytical model is derived that approximates an RTBC's COP from the pressure ratio ($PR$), heat rejection temperature ($T_{reject}$), load temperature ($T_{load}$), as well as the performance of the individual system components. The equations of this analytical model can be found in Appendix A while their full derivation is provided in Section 4.4 of the literature study attached to this document.

To derive this analytical model, several assumptions were made. Firstly, no pressure drops in the fluid loop are taken into account. Secondly, the fluid properties ($c_p$ and $\gamma$) are only evaluated at two discrete points of the cycle, namely the hot end ($T_1$) and cold end ($T_5$). The continuous variation of fluid properties throughout the cooler is thus neglected. However, the model still captures the global change in fluid properties to some extent. Additionally, the analytical model doesn't take into account any heat leak from the environment. Note also that this analytical model only provides an estimate for the COP of the cooler and not the specific power.

A simplified analytical equation has also been presented by Zagarola et al. which assumes a 100% effective recuperator, aftercooler, and tank heat exchanger. It does however account for the heat leak from the environment in the recuperator, expressed by a non-dimensional coefficient $\beta$, which is the heat leak relative to the turbine power.[28] When using the same assumptions, the analytical model of this study (Equation 47) provides the same results as the analytical equation of Zagarola et al, see Equation 1.

$$COP = \eta_{comp} \cdot \eta_{turb} \cdot (1-\beta) \cdot \frac{1}{PR^{\frac{\gamma-1}{\gamma}}} \cdot \left(1 - \frac{T_{load}}{T_{reject}}\right) \cdot \eta_{carnot} \qquad [1]$$

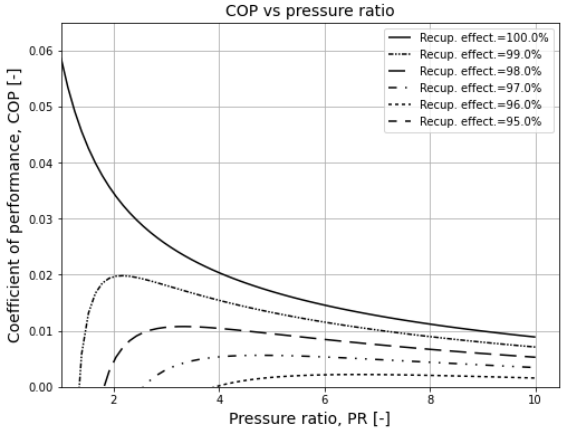


Fig. 4: Analytical solution for the COP as function of the RTBC pressure ratio and recuperator effectiveness in case of an 80% effective aftercooler, an 80% effective tank heat exchanger, 85% efficient turbine, and 75% efficient compressor, using gaseous helium at a load temperature of 20K and rejection temperature of 250K.

The analytical model is used to define the input ranges of the sensitivity study that is described in section 3. Additionally, it provides an initial estimate of the iteration variables of the RTBC numerical model as well as a verification method for the results of the more detailed model. An example of the results obtained with the analytical model is shown in Fig. 4, where a set of input conditions representative of the sensitivity study has been considered.

## 2.2 RTBC numerical model

The numerical RTBC model differs from the analytical one for the fact that the different components are simulated individually and more loss sources are accounted, thereby providing a more accurate representation of the real RTBC performance. For example, it accounts for the continuous change of fluid properties, pressure losses over the components, and the heat leak from the environment. Additionally, this numerical model also performs the sizing of the heat exchangers and thereby provides an estimate of the RTBC's mass and specific power.

The solution of the RTBC model requires an iterative procedure. There are two independent iterations loops: one for the system of equations defining the process on the cold side (from point 3 to 1) and one for the system of equations pertaining to processes on the hot side of the RTBC (from point 1 to 3). The logic of this program is presented in Fig. 5. In the cold side iteration loop, the mass flow rate of the cycle is the iteration variable, as this quantity can be determined given the turbine efficiency, the cooling capacity, and performing the sizing of the recuperator and tank HEX. The mass flow rate is iterated until its relative change per iteration is lower than a given tolerance of 0.1%. The initial value of the mass flow rate is calculated using the analytical model described in subsection 2.1. Once the mass flow rate of the RTBC has converged, the code will initiate the hot side iteration loop, whose tear variable is the pressure ratio of the compressor.

Initially, the compressor ratio is determined given the isentropic efficiency of the machine, the temperature to be reached in station 3, and the effectiveness of the aftercooler. Once the thermodynamic state at the outlet of the compressor (point 2) is known, the aftercooler performance is calculated, alongside the working fluid's pressure drop. Then the compressor's

pressure ratio is increased by the pressure drop. These steps are repeated until the change in the aftercooler pressure drop is less than 0.1% relative to the compressor's pressure rise.

The continuation of this chapter provides an overview of the models of the different RTBC components that were used to calculate the system performance and weight.

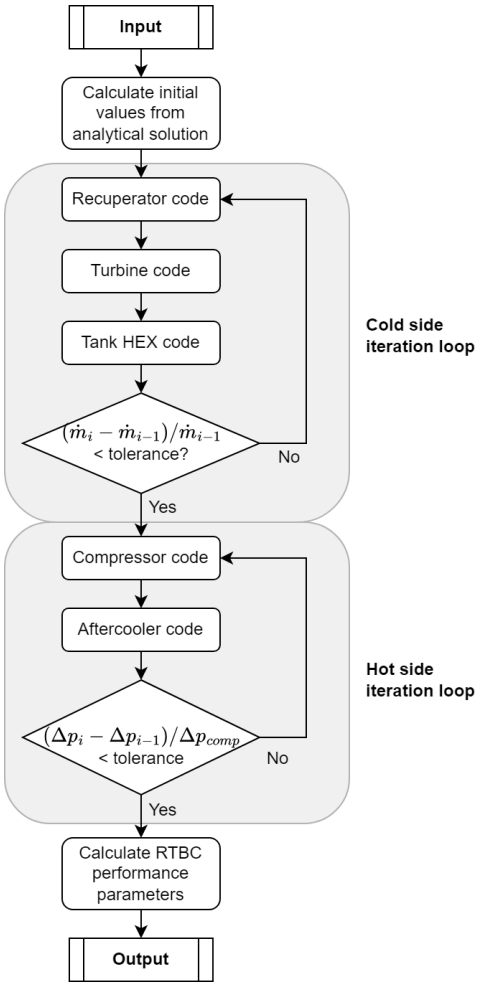


Fig. 5: Schematic overview of the RTBC program.

## 2.3 Turbomachinery models

The primary focus of this study lies on the modeling of the heat exchangers of the RTBC. The compressor and turbine of the RTBC are not modeled in detail and their masses are neglected in the current model. Although still relevant, the mass of the compressor and turbine is typically an order magnitude smaller than that of the heat exchangers, especially the recuperator. The prediction of the turbomachinery efficiency is considered beyond the scope of this study. The specific enthalpy change over the compressor and turbine are modeled using their respective pressure ratios and predefined isentropic efficiency, as shown by Equation 2. The temperature is then calculated from the specific enthalpy and pressure using CoolProp.[37]

$$h_{out} = h_{in} + \eta_{isen} \cdot (h_{out,isen} - h_{in}) \quad [2]$$

The specific enthalpy at the outlet in case of an isentropic process ($h_{out,isen}$) is calculated using CoolProp given the temperature and pressure conditions that follow from the pressure ratio and the isentropic relation, in Equation 3

$$T_{out,isen} = T_{in} \cdot PR^{\frac{\gamma-1}{\gamma}} \quad [3]$$

## 2.4 Recuperator model

The recuperator is one of the most critical components of the RTBC in terms of both system performance and mass. Therefore, a relatively detailed model was constructed that takes into account multiple loss sources such as the change in fluid properties, environmental heat leak, and longitudinal conduction through the walls. The effect of flow maldistribution inside the HEX is not modeled.

The coil-wound HEX model developed for this study calculates the required length of the recuperator to achieve a target effectiveness for a given tube and shell geometry and design specifications. After an initial estimate is made, the length is iterated until the effectiveness matches the target value with a residual of less than $5 \cdot 10^{-5}$. The change in length per iteration is calculated from the ratio of the calculated and target effectiveness, multiplied with a relaxation factor of 0.5 to improve the code stability. Additionally, the change in length per iteration is limited to 25% of the recuperator length.

### 2.4.1 Geometry

The CWHEX contains an inner core around which multiple concentric layers of tubes are wound. The distance between each of these tube layers is set to be the same as the distance between two neighboring tubes. These distances are an often used variable for flow correlations, however in a non-dimensional form

after division by the tube's outer diameter: the non-dimensional transverse and longitudinal tube spacing ($S_T$ and $S_L$ respectively). Due to the limited amount of relevant flow correlations capable of accounting for different tube spacings of a coiled, cross-inclined tube bundle, a fixed value of 1.5 is chosen for both. Multiple tube spacers are placed between each tube layer to ensure a relatively homogeneous spacing, as can be seen in Fig. 6. In this study, 12 rectangular spacers are used per layer of tubes.

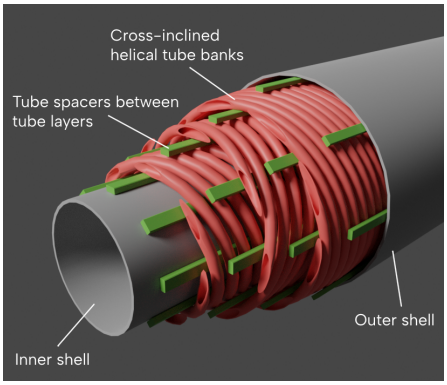


Fig. 6: 3D illustration of a simplified CWHEX with three layers of tubes and spacers in between.

All tube layers feature the same coil or helix angle ($\phi$), here defined as the angle between the longitudinal axis of the HEX and the tube. However each tube layer has an opposite orientation of the helix compared to that of the neighboring ones, making this a cross-inclined configuration. This configuration provides improved thermo-hydraulic performance compared to a parallel-inclined configuration, as demonstrated by Groehn.[38] It was found that for the same coil angle, each tube also has the same length regardless of the coiling diameter. This partially justifies the validity of neglecting flow maldistribution in the HEX as similar pressure losses can be expected in each coil.

The CWHEX includes a zone that allows the shell-side fluid to distribute over the whole crossection of the HEX, as shown in Fig. 8. In this region, the tubes have a straight path instead of a helical one. In this study, the length of this entrance region is set to be equal to the CWHEX's outer radius. The ends of the CWHEX are closed with hemispherical domes. As shown in Fig. 7, all tube ends are attached to a cylindrical plate, called the tubesheet, that connects the tubes to the inlet or outlet ports of the recuperator.

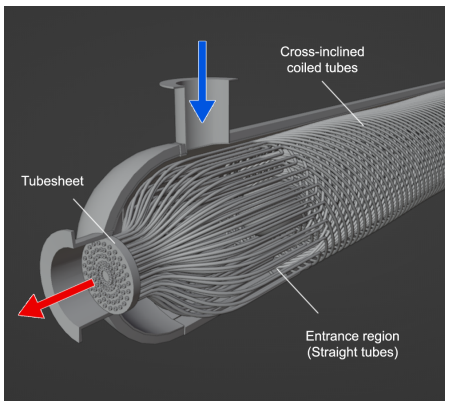


Fig. 7: 3D illustration of the entrance region of the CWHEX.

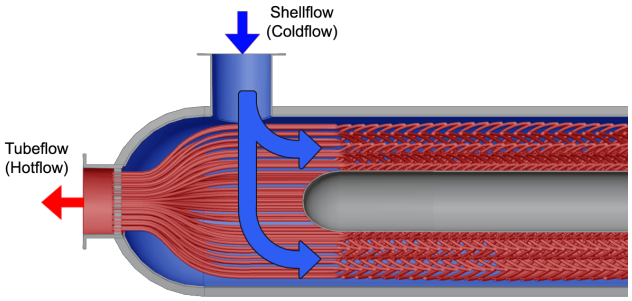


Fig. 8: Illustration of the hot (red) and cold (blue) flow path in the entrance region of the CWHEX.

### 2.4.2 Assumptions

The steady state CWHEX model of this study is based on the following assumptions:

- Axial conduction through the working fluid is neglected. This assumption is justified by the observation that the non-dimensional Péclet number is lower than 100 at any point in the CWHEX.
- The flow through the CWHEX is assumed to be perfectly mixed at each segment, neglecting any effects of flow maldistribution or fluid stratification.
- The flow through the CWHEX is assumed to be fully developed and entrance effects are not taken into account.
- The radial temperature gradients in the walls of the tubes, outer shell, and inner core are assumed

to be negligible because of the thin walls. Instead, the model assumes a uniform radial temperature profile across these walls.
- The outer temperature of the CWHEX's insulation is assumed to be equal to that of the environment. The thermal resistance due to the external convection is thus neglected. This leads to a slight overestimation of the heat transfered from the environment towards the working fluid.
- The conductive heat transfer occurring at the ends of the CWHEX is assumed to be negligible. Hence a zero heat flux boundary conditions is imposed on the ends of each of the control volumes of the CWHEX walls.
- Axial conduction through the insulation is neglected because of the low thermal conductivity and the small longitudinal temperature gradient of the insulation material.
- The flow in the entrance region of the shell is assumed to be perpendicularly to the tubes, instead of following a curved trajectory, as illustrated in Fig. 8.

#### 2.4.3 Structural analysis

Several structural calculations are performed based on the CWHEX's geometry and operating conditions. The structural sizing methods that are used in this study are however only a first-level estimate and it is therefore recommended to develop more in-depth structural models to increase the accuracy of the CWHEX mass estimate in future studies.

The wall thickness of the CWHEX's cylindrical elements (tubes, core, outer shell, and inlet pipes) is calculated given the material's yield strength ($\sigma_y$), the diameter ($D$), and the pressure difference ($\Delta p$) accross the wall. Here a safety factor ($SF$) of 2.5 is applied to the pressure difference. Equation 4 shows the minimum wall thickness using the thin walled assumption, which is only for a diameter to thickness ratio larger than 20. At the same time, a minimum wall thickness was imposed, being 0.25 mm for the tubes, 0.5 mm for the inner and outer shell wall, and 1.5 mm for the inlet/outlet ports.

$$t = max\left(t_{min}; \frac{SF \cdot \Delta p \cdot D}{\sigma_y}\right) \quad [4]$$

The tubesheet can be a relatively thick and heavy component of the CWHEX due to the many perforation that reduce its ability to effectively deal with the pressure difference between the fluids inside the tube inlet port and shell. The TEMA (Tubular Exchanger Manufacturers Association) guidelines for the design of unsupported, fixed tubesheets for shell-tube heat exchangers is used to determine the tubesheet's thickness.[39] It should be noted that the thermal loads associated with differences in the thermal expansion between the shell and tubes are not taken into account as the large coil angle of the tubes reduces the loads on the tubesheet.

The thickness and diameter of the inlet and outlet flanges was determined using data from commercially available pipe flanges for representative pressure ratings.

#### 2.4.4 Finite difference model

The effectiveness of the CWHEX for a given length is calculated from the heat exchanged between the hot and cold fluid ($\dot{Q}$), and the maximum theoretically possible heat exchange ($\dot{Q}_{max}$). The latter is calculated using Equation 5. Here the maximum specific enthalpy change of each flow is calculated using the respective inlet pressure of each flow and the temperature difference between both inlets, assuming that the hot and cold fluid have the same temperature at the inlet and outlet of the HEX.

$$\dot{Q}_{max} = min\left(\dot{m}_{hot} \cdot \Delta h_{hot,max}; \dot{m}_{cold} \cdot \Delta h_{cold,max}\right) \quad [5]$$

The total heat transfer between the two fluids is calculated as the sum of the heat transfer at each of the individual segments discretizing the CWHEX (denoted by subscript $i$), as shown in Equation 6.

$$\dot{Q} = \sum \dot{Q}_i \quad [6]$$

The CWHEX is distributed in multiple segments or cells along its length where each segment is treated as an individual heat exchanger where fluid properties are assumed constant. For each segment a set of steady state conservation equations is solved. Each segment is discretized in six control volumes, which represent the shell-side flow path, the tube-side flow path, the tube wall, the inner core wall, the outer shell wall, and the tube spacers. Fig. 9 shows the interaction between the different control volumes of a segment. A zero heat flux boundary condition is imposed at the outermost wall segments. The specific enthalpy associated with

the flow leaving the control volume is assumed equal to that of the fluid in the control volume itself.

The segments of the CWHEX are distributed with increasingly more elements at the two HEX ends. This is beneficial to properly capture the larger changes in the temperature gradient along the axial direction of the HEX caused by axial conduction, which is observed in the proximity of the two extremes of the tube bundle.

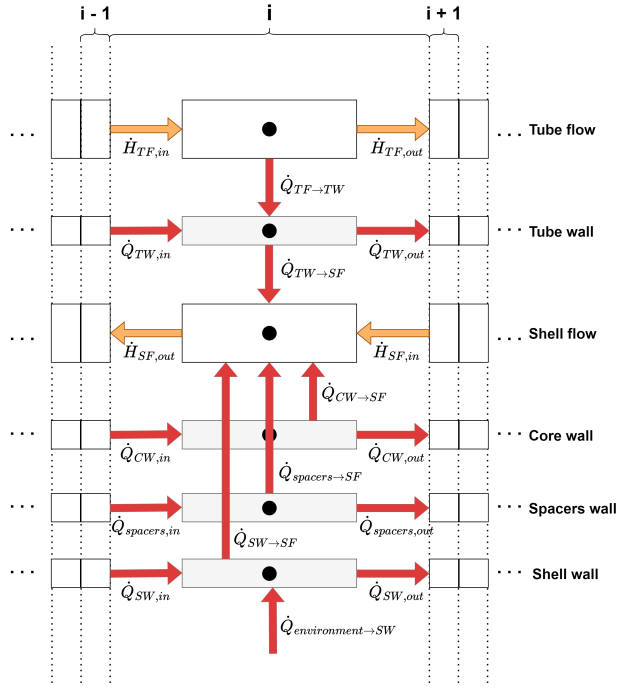


Fig. 9: Interaction between the different control volumes of a CWHEX segment (i), highlighting the heat and mass transfer.

The conservation equations for the six different components are shown below as a function of the heat and mass transfer occurring at the borders of their respective control volumes. The left hand side of these equations represents the residual heat that should converge to zero to achieve a correct solution. The properties of the flow inside the tubes are denoted with subscript $TF$ and those of the fluid on the shell side are denoted with subscript $SF$. The CWHEX tube wall, shell wall, core wall, and spacers are denoted with subscripts $TW$, $SW$, $CW$, and $spacers$, respectively.

$$\dot{Q}_{res,TF} = \dot{m}_{TF} \cdot (h_{TF,in} - h_{TF,out}) - \dot{Q}_{TF\to TW} \quad [7]$$

$$\dot{Q}_{res,SF} = \dot{m}_{SF} \cdot (h_{SF,in} - h_{SF,out}) + \dot{Q}_{TW\to SF} + \dot{Q}_{spacers\to SF} + \dot{Q}_{CW\to SF} + \dot{Q}_{SW\to SF} \quad [8]$$

$$\dot{Q}_{res,TW} = \dot{Q}_{TW,in} - \dot{Q}_{TW,out} + \dot{Q}_{TF\to TW} - \dot{Q}_{TW\to SF} \quad [9]$$

$$\dot{Q}_{res,CW} = \dot{Q}_{CW,in} - \dot{Q}_{CW,out} - \dot{Q}_{CW\to SF} \quad [10]$$

$$\dot{Q}_{res,spacers} = \dot{Q}_{spacers,in} - \dot{Q}_{spacers,out} - \dot{Q}_{spacers\to SF} \quad [11]$$

$$\dot{Q}_{res,SW} = \dot{Q}_{SW,in} - \dot{Q}_{SW,out} - \dot{Q}_{SW\to SF} + \dot{Q}_{environment\to SW} \quad [12]$$

The convective heat transfer between a fluid ($F$) and its neighboring wall ($W$) is calculated using the representative heat transfer coefficient, as shown in Equation 13.

$$\dot{Q}_{F\to W} = U_{F\to W,i} \cdot A_{F\to W,i} \cdot (T_{F,i} - T_{W,i}) \quad [13]$$

The heat transfer coefficients ($U$) are calculated from the Nusselt number ($Nu$), the fluid's thermal conductivity ($k$), and a reference dimension ($x$), as shown in Equation 14. Subsection 2.4.5 explains which correlations are used to calculate the Nusselt numbers for the hot and cold stream.

$$U = \frac{Nu \cdot k}{x} \quad [14]$$

A central difference scheme is used to determine the specific enthalpy inflow and outflow of each of the fluids' control volumes, with exception of the first and last cell. In this scheme, the specific enthalpy that enters and leaves each control volume is equal to the average of the specific enthalpy in this control volume and its respective neighbouring control volume.

The axial conduction between neighboring wall segments ($\dot{Q}_W$) is also modeled using a central difference scheme, as shown in Equation 15 and Equation 16 for

the left and right side of each wall's control volume respectively.

$$\dot{Q}_{W,in} = k_{W,i} \cdot A_{crossec} \cdot \frac{T_{W,i-1} - T_{W,i}}{x_i - x_{i-1}} \quad [15]$$

$$\dot{Q}_{W,out} = k_{W,i} \cdot A_{crossec} \cdot \frac{T_{W,i} - T_{W,i+1}}{x_{i+1} - x_i} \quad [16]$$

The thermal conductivity of the wall material is evaluated at the temperature of the wall segment using Hust-Lankford's model for aluminium-5083 (a commonly used alloy for cryogenic applications), as proposed by A. L. Woodcraft.[40]

The heat flow from the environment towards the outer shell ($\dot{Q}_{environment \to SW}$) is calculated using the method of resistivity, similar to that explained in subsection 2.5. Equation 35 is used to find the thermal resistance of the radial heat flow through the insulation and metal shell wall. The thermal resistance of the insulation ($R_{insulation}$) and shell wall ($R_{SW}$) can simply be added as the heat from the environment passes through them sequentially. As stated in the assumptions, the thermal resistance due to the external convection around the CWHEX is neglected.

$$\dot{Q}_{environment \to SW} = \frac{T_{environment} - T_{SW}}{R_{insulation} + R_{SW}} \quad [17]$$

For each fluid segment, the local pressure is calculated given that of the upstream segment, and subtracting to its value the pressure drop of the upstream element. The empirical correlations used to calculate of the pressure drop in a fluid segment are explained in Subsubsection 2.4.5.

Because this is a counter-flow heat exchanger, an iterative process is required to solve for the temperature distribution. A linear temperature distribution is assumed as an initial guess. The iteration loop will sequentially calculate an updated temperature and pressure for each segment until the maximum non-dimensionalized residual of the conservation equations reaches a value below 1e-5. This iterative process is fully explicit as the temperature and pressure distribution at the previous iteration is used to calculate the updated temperature and pressure in each segment. The program workflow diagram is shown in Fig. 10.

The entrance and exit regions of the CWHEX are modeled as a single control volume with an average heat transfer coefficient based on the correlations for flow through and over a straight tube bundle. Axial conduction through the tube, shell, spacers, and core walls of the entrance regions is not modeled.

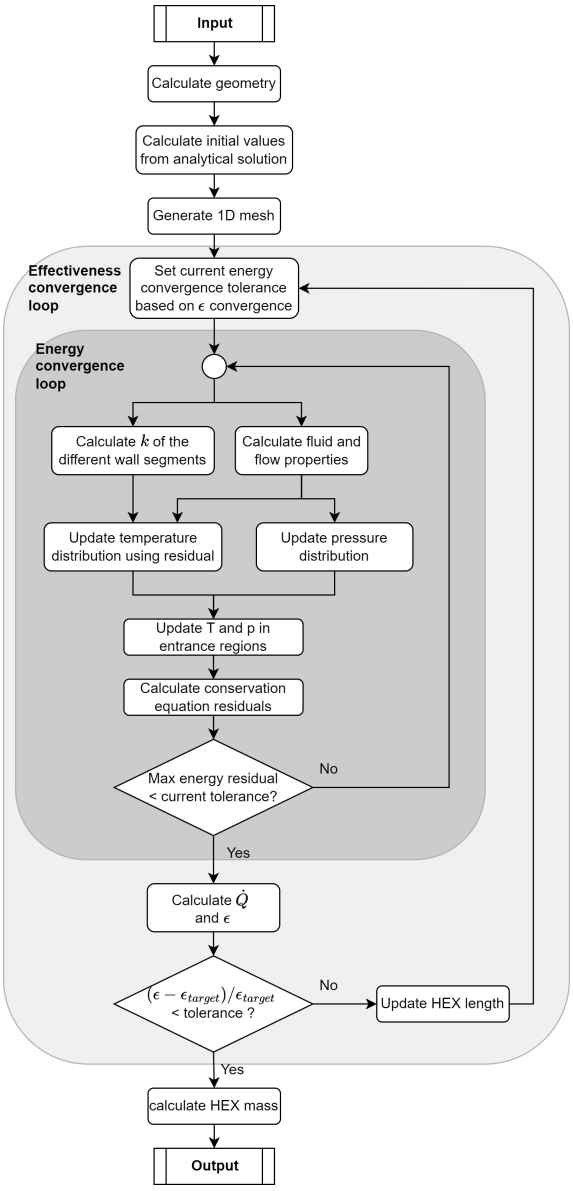


Fig. 10: CWHEX model workflow diagram showing the two iterative loops to achieve convergence of the energy residuals and HEX effectiveness.

2.4.5 Heat transfer and friction factor correlations

For each of the CWHEX elements, a set of empirical correlations is used to calculate the local heat transfer coefficient and pressure drop knowing the Nusselt number ($Nu$) and Fanning friction factor ($f$). This section provides a summary of the correlations that were implemented for the flow in the tube and shell side of the HEX. For a detailed overview of the flow correlations, the reader is referred to Appendix C.

**Flow through straight and coiled tubes**

The Fanning friction factor of the flow through the coiled tubes is modeled by first calculating that of equivalent straight tubes, which varies with the flow regime as shown in Equation 18. The first correlation, being $16/Re$, is valid for laminar flows as suggested by Shah and Sekulic.[31] For transitional and turbulent flows in straight tubes, the correlation from Bhatti and Shah is used.[41]

$$f=\begin{cases} 16/Re & \text{for } Re<2100 \\ 0.00128+0.1143\cdot Re^{-1/3.2154} & \text{for } 2100<Re<3500 \\ 0.00128+0.1143\cdot Re^{-1/3.2154} & \text{for } 3500<Re<10^7 \end{cases} \quad [18]$$

Multiple authors have proposed methods to correct the friction factor for helical tubes using the Dean number ($De$). The definition of this dimensionless quantity is based on the tube's internal diameter ($D_{tube}$) and the coiling radius ($R_{coil}$), as shown in Equation 19.[42]

$$De = Re \cdot \left(\frac{D_{tube}}{2 \cdot R_{coil}}\right)^{0.5} \quad [19]$$

For laminar flows ($1 < De < 3000$), the correction proposed by Mishra and Gupta was implemented, see Equation 20.[43]

$$\frac{f_{lam,coiled}}{f_{lam}} = \left\{1 - \left[1 - \left(\frac{11.6}{De}\right)^{0.45}\right]^{1/0.45}\right\}^{-1} \quad [20]$$

For turbulent flows, Ito's correlation is used in this study.[44] Equation 21 is valid for the range $0.034 < Re \cdot (D_{tube}/(2 \cdot R_{coil}))^2 < 300$.

$$f_{turb,coiled}=\frac{1}{4}\left(\frac{D_{tube}}{2\cdot R_{coil}}\right)^{\frac{1}{2}}\left\{0.029+0.304\left[Re\left(\frac{D_{tube}}{2\cdot R_{coil}}\right)^2\right]^{-0.25}\right\} \quad [21]$$

A linear transition from the laminar to turbulent flow correlation is used to provide continuity between these flow regimes, as there is a lack of correlations for transitional flows in coiled tubes.

The Nusselt number for the flow inside the coiled tubes in case of laminar flow is calculated using the correlation from Manlapaz-Churchill (Equation 22) that assumes a constant radial temperature distribution and uniform heating.[45]

$$Nu_{lam}=\left[\left(48/11+\frac{51/11}{(1+1342/(Pr\cdot He^2))^2}\right)^3+1.816\cdot\left(\frac{He}{1+1.15/Pr}\right)^{3/2}\right]^{1/3} \quad [22]$$

where the helical number ($He$) is defined as:

$$He = \frac{De}{\left[1 + \left(pitch \cdot \frac{\pi}{2} \cdot \frac{D_{tube}}{2}\right)^2\right]^{0.5}} \quad [23]$$

For turbulent flow through the coiled tubes, the correlation from Petukhov-Popov was used, as shown in Equation 24.[46] This correlation is valid for $4 \cdot 10^3 < Re < 5 \cdot 10^6$ and $0.5 < Pr < 10^6$.

$$Nu_{turb} = \frac{Re \cdot Pr \cdot f/2}{C + 12.7 \cdot (f/2)^{0.5} \cdot \left(Pr^{2/3} - 1\right)} \quad [24]$$

where

$$C = 1.07 + \frac{900}{Re} - \frac{-0.63}{1 + 10 \cdot Pr}$$

The laminar Nusselt correlation is used when the Reynolds number of the flow inside the tubes is lower than the critical Reynolds number for coiled tubes as defined by Srinivasan.[47] (Equation 25). However, it should be noted that the flow transition from laminar to turbulent is less well-defined and abrupt compared to straight tubes.

$$Re_{crit} = 2100 \cdot \left[1 + 12 \cdot \left(\frac{D_{tube}}{2 \cdot R_{coil}}\right)^{0.5}\right] \quad [25]$$

Between the critical Reynolds number and that corresponding to the lower limit of the Nusselt number correlation for turbulent flows, e.i. $4 \cdot 10^3$, a linear interpolation between Equation 22 and Equation 24 is used. This interpolation does not accurately capture

the complex behaviour of transitional flow in coiled tubes, but merely serves as a continuity between the laminar and turbulent regime.

Finally, as the present model doesn't simulate the flow through each tube or tube layer individually, an average of the friction coefficient ($f$) and Nusselt number ($Nu$) has to be calculated per segment. This is performed by calculating $f$ and $Nu$ for each tube layer with their respective coiling angle and then averaging the estimated values to arrive at a representative average friction factor and Nusselt number per segment.

**Flow over cross-inclined coiled tube banks**

The amount of literature available on the flow over the tube banks of CWHEXs is very limited. There are however correlations for flows over different configurations of tube banks. The experimental study by Groehn identified that the flow correlations of straight inclined tube banks very well represent those of coiled tube banks, for a similar configuration.[38] The present study has a CWHEX that features a cross-inclined, spiral-wound tube configuration where the coil angle is set to be the same for all tubes. Due to the limited amount of data and correlations predictive for different tube spacings of this type of tube banks, both the longitudinal and transverse tube spacing are fixed to a value of 1.5 $D_{tube}$.

The cross-inclined CWHEXs tested by Groehn very closely resemble the recuperator of present study. No correlations were derived based on these experimental results. Therefore, a Nusselt number and hydraulic resistance correlation was fitted based on Groehn's data and compared to existing correlations for tube banks. An in-depth explanation of this activity and the comparison to other correlations can be found in Appendix C.

The fitted Nusselt number correlation (Equation 26) shows that there is little influence of the non-dimensional tube spacings in the range of 1.15 to 2. It should be noted that the Reynolds number in this equation is based on the outer tube diameter and the maximum local flow velocity, which typically occurs at the narrowest crossection between two cross-inclined tube layers.

$$Nu = 0.4005 \cdot Pr^{0.36} \cdot [Re \cdot sin(\phi)]^{0.5793} \quad [26]$$

$$Re_{tubebank} = \frac{\rho \cdot D_{tube} \cdot V_{max}}{\mu} \quad [27]$$

The pressure drop in the shell-side flow is calculated with a pressure drop coefficient ($\xi$) using Equation 28. Notice that the number of times the fluid flows over a tube ($z$).

$$\Delta p = z \cdot \xi \cdot 0.5 \cdot \rho \cdot V^2 \quad [28]$$

The pressure drop coefficient is estimated using the correlation derived from Groehn's experiment, see Equation 29. It is however important to be aware of the large uncertainties that are associated with the estimation of the pressure drop over these tube banks as there is a large spread in the predictions of different empirical models for pressure drop over helical cross-inclined tube banks as explained in Appendix C.

$$\xi = 69034 \cdot (\phi \cdot 180/\pi)^{-2.6777} \cdot Re^{-58.8943 \cdot (\phi \cdot 180/\pi)^{-1.4619}} \quad [29]$$

2.4.6 Verification and validation

The verification of the CWHEX model was performed by comparing the predicted effectivenss against that estimated by the simple analytical expression for counterflow HEXs.

The value for the maximum allowable residual of the HEX effectiveness and the energy balance equations must be chosen such that the code converges to consistent results within a reasonable computational time. A threshold of 1e-4 was found to ensure the convergece of the solution for the majority of the cases. However, at recuperator effectiveness of 97% or higher, it was found that a threshold lower than 1e-5 was necessary to achieve a converged solution.

After establishing the convergence thresholds, a mesh independence study was performed. It was established that 25 segments are adequate to get accurate results. The adoption of more segments significantly increases the computational time, with marginal gains in accuracy, particularly considering the uncertainty range of the empirical correlations.

The comparison results are shown in Fig. 11 for balanced and imbalanced HEXs. It is apparent that predictions of the both models are in agreement, except for very high values of the number of heat transfer units,

as the value of the threshold selected for the effectiveness equation residual become relatively high compared to the increase in effectiveness observed for increasing values of NTU.

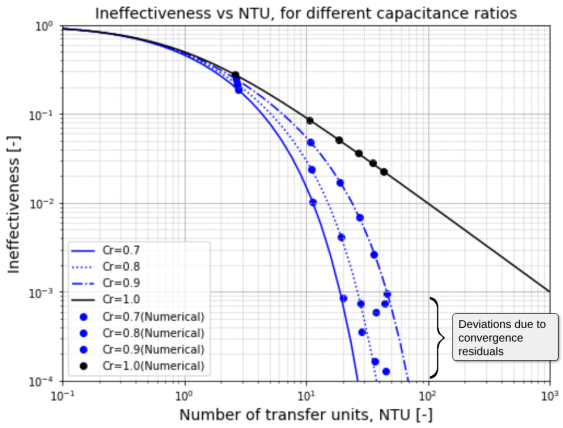


Fig. 11: Complement to 1 of the HEX effectiveness $(1-\epsilon)$ for different heat capacitance ratios $(Cr)$ predicted by the analytical model and the numerical one.

Due to the scarce amount of CWHEX data available in literature, a complete validation of the model was not possible.

The Nusselt number correlations that can be used for coiled tube are those of Kalb-Seadler,[48] Manlapaz-Churchill,[45] Schmidt,[49] Petukhov-Popov,[46] and Rogers-Mayhew.[50] As shown in Fig. 12, there is a generally good agreement between the different models. For the turbulent flow regime, the correlations deviate less than 9%, while for the laminar regime the correlations deviate less than 13%. The Fanning friction factor for smooth coiled tubes is evaluated using the correlations of Mishra-Gupta,[43] White,[51] Ito,[44] and Srinivasan,[47] as shown in Fig. 13. There is an excellent agreement between the two laminar flow correlations less than 5%, as well as between the turbulent flow correlations less than 8% within the applicable Reynolds number range.

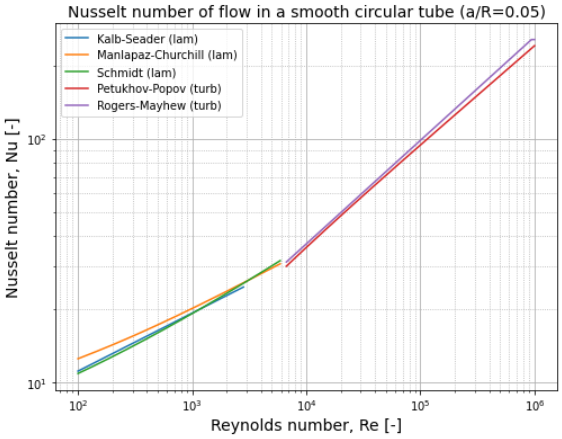


Fig. 12: Nusselt number predicted by various empirical correlations for flow in smooth, coiled tubes with $D_{tube}/(2 \cdot R_{coil}) = 0.05$

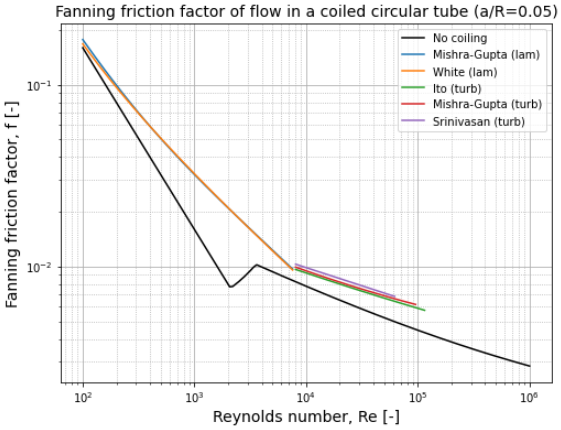


Fig. 13: Fanning friction factor predicted by various empirical correlations for flow in smooth, coiled tubes with $D_{tube}/(2 \cdot R_{coil}) = 0.05$

Several Nusselt number correlations for flow over different tube bank configurations are compared to the correlation that was implemented in this study, using Groehn's data. These correlations are shown in Fig. 14 and include those of Žukauskas,[52] Abazdic,[53] Kim's correction on Zukauskas',[54] and Le Feuvre.[55] It can be seen that the fitted correlation very well agrees with the other correlations. It does however show a slightly lower increase in Nusselt number with increasing Re. The discrepancy between this correlation and the other four is at most 21%, which corresponds to the

typical uncertainty reported in the literature for heat transfer correlations.

There are only very few correlations available to calculate the pressure drop over cross-inclined, coiled tube bundles. The predictions of these correlations are compared in Fig. 15 for different coil angles. Because the different correlations don't use the same variables to calculate the pressure drop, it is difficult to make a direct comparison. Therefore, the correlations from Žukauskas,[52] Le Feuvre,[55] Hua, Dixon, and the fitted correlation from Groehn's data[38] have been compared for several representative test cases, such as the one presented in Fig. 15 for example. The latter correlation provides estimates similar to those of the correlations of Hua ($< 5\%$) and Dixon ($< 16\%$).

Although the trend of the pressure drop with the Reynolds number predicted by the various correlations matches very well, the correlation of Le Feuvre consistently shows a 50% lower pressure drop compared to the correlations from Groehn's data. Moreover, the correlation of Žukauskas leads to pressure drop values about 200% larger compared to the fitted correlation from Groehn's data at Reynolds number above 500.

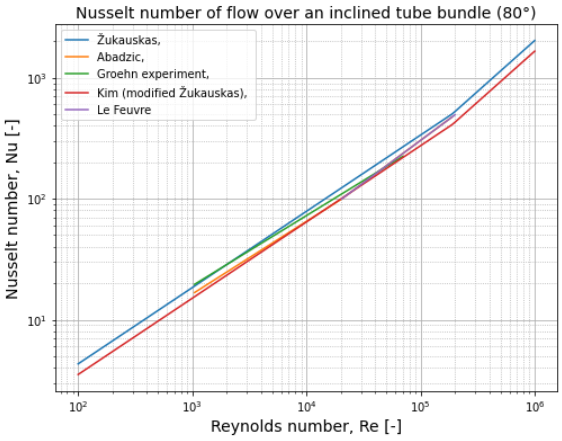


Fig. 14: Nusselt number correlations for flow over tube banks at a coil angle of $80^o$.

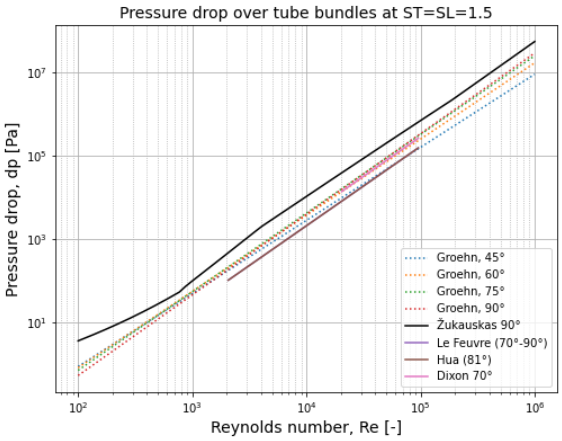


Fig. 15: Pressure drop of flow over tube banks.

## 2.5 Tank HEX model

The tank heat exchanger considered for this study is similar to that of NASA's GODU experiment, where ZBO for a large liquid hydrogen tank was successfully demonstrated.[6] The HEX features two horizontal manifolds, as shown in Fig. 16. The upstream manifold is here called a distributor, while the other is called the collector. The manifolds are connected by several smaller tubes which provide most of the cooling power to the fluid in the tank. The use of orifices at each tube inlet allows for an equal distribution of the helium mass flow rate with less than 1% deviation. In this study, only the mass of the tubes and manifolds is taken into account, whilst the structural supports, orifices, and inlet ports are not included.

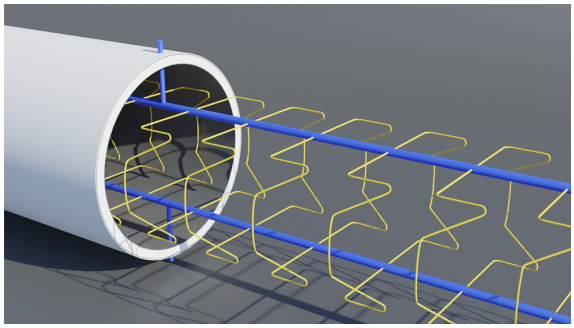

Fig. 16: Visual representation of the tank heat exchanger design of this study, showing how the tubes connect the two horizontal manifolds.

The tank HEX model in this study calculates the component mass and pressure drop on the RTBC working fluid side for a given heat duty ($\dot{Q}$), effectiveness ($\epsilon$), coolant inlet conditions, and fluid conditions. From the imposed heat duty and effectiveness, the working fluid mass flow rate can be calculated using Equation 30.

$$\dot{m} = \frac{\dot{Q}}{\epsilon \cdot (h_{in} - h_{out,max})} \quad [30]$$

The number of tubes connecting the two manifolds is an input of the model, while the diameter of the tubes and manifolds is allowed to vary to match the prescribed HEX effectiveness. The Reynolds numbers of the flow inside the tubes and manifolds are used as design variables of the tank HEX. The corresponding diameters can then be estimated using Equation 31. Here the mass flow through each of the tubes is assumed to be equal, which was proven to be feasible by NASA using orifices.[6]

$$D = \frac{4 \cdot \dot{m}}{\mu \cdot \pi \cdot Re} \quad [31]$$

The Reynolds number that corresponds to the correct effectiveness is found by performing a single-variable Nelder-Mead optimization that aims to minimize the relative effectiveness error down to a value below 1e-5. If the Reynolds number (internal forced convection) or tube Rayleigh number (outside natural convection) falls outside the valid range for the heat transfer correlations, the effectiveness of the HEX is adjusted. In case the pressure drop over the tank HEX is more than 0.3 bar, the optimization is run again with a reduced tube length. The flow diagram of the tank HEX design procedure can be found in Appendix B alongside an in-depth overview of the tank HEX model in the appendix "Tubular heat exchanger model for distributed cooling of a liquid hydrogen tank".

The tank HEX model is based on several assumptions, of which the most significant are explained here. A more detailed list of all the assumptions and their validity can be found in Appendix D. The model assumes a perfectly mixed and fully developed flow through the tubes. Furthermore, the mass flow rate in each tube is assumed to be equal. Additionally, only a quarter of the tank HEX tubes is simulated as the HEX is assumed to be perfectly symmetrical. Thermal radiation, longitudinal conduction, and gravitational effects are considered negligible. Furthermore, the tank HEX is assumed to be fully submerged in the liquid hydrogen. Finally pressure drop effects associated with tube bends, flow mixing, and entrance effects are not taken into account.

The pressure drop of the working fluid and the heat transfer between this and the tank fluid are calculated by discretizing the two distributors and tubes of the HEX. For each individual segment the pressure drop and temperature change are calculated by assuming constant properties in each control volume using empirical correlations. The temperature and pressure inside the tank are assumed to be constant. This prevents the need for an iterative solving method and thereby allows for a step-wise calculation of the fluid and flow properties from the inlet to the outlet of the tank HEX.

The pressure drop over the tubes is set equal to that of the outermost tube pair, which experiences the largest pressure drop. The underlying assumption the use of orifices equalize the mass flow rates across the tubes. The pressure drop in the coolant flow in the outermost tube pair is calculated using a similar approach to that described in subsubsection 2.4.5 for the CWHEX model, albeit for straight tubes. The equation for the pressure drop is shown in Equation 32.

$$\Delta p = 4 \cdot f \cdot L_{segment} \cdot 0.5 \cdot \rho \cdot V^2 / D_{inner} \quad [32]$$

The fluid density ($\rho$) in each control volume is found using CoolProp from the given the temperature and pressure at the outlet of the upstream control volume. The flow velocity is calculated from the steady state mass balance, as shown in Equation 33 The effect of the pressure drop on the density change is however not taken into account the tank HEX. The change in velocity of the flow through the tubes is thus only affected by the temperature change. Therefore this model is only valid for low relative pressure drops.

$$V = \frac{4 \cdot \dot{m}}{\rho \cdot D_{inner}^2 \cdot \pi} \quad [33]$$

The heat transfer between the fluid in the tank and the coolant in each segment is calculated given the estimated equivalent thermal resistance to heat transfer. Three thermal resistance components are considered in series: internal forced convection (1), radial conduction through the tube wall (2), and external natural convection (3).

The thermal resistance due to forced convection is calculated using Equation 34, where the heat transfer coefficient ($U$) is found in a similar manner as for the CWHEX. The same Nusselt number correlations are used, but for straight tubes.

$$R_{conv,inner} = \frac{1}{U \cdot A} = \frac{D_{inner}}{Nu \cdot k \cdot A} \quad [34]$$

The thermal resistance associated with the radial conduction through the tube wall is found by applying Equation 35, which represents the thermal resistance of a hollow cylinder with homogeneous thermal conductivity k.

$$R_{cond,radial} = \frac{ln(D_{outer}/D_{inner})}{2 \cdot \pi \cdot k_{wall} \cdot L_{section}} \quad [35]$$

The thermal conductivity of the material is calculated from an empirical correlation, specifically derived for stainless steel 304 (see Equation 36) by NIST[56] as compiled from Mann[57] and Touloukian and Ho.[58]

$$\begin{aligned} log(k_{steel}) = &-1.4087 + 1.3982 \cdot log(T) + 0.2543 \cdot (log(T))^2 \\ &- 0.6260 \cdot (log(T))^3 + 0.2334 \cdot (log(T))^4 + 0.4256 \cdot (log(T))^5 \\ &- 0.4658 \cdot (log(T))^6 + 0.1650 \cdot (log(T))^7 - 0.0199 \cdot (log(T))^8) \end{aligned} \quad [36]$$

An initial estimate of the wall temperature is used to calculate the thermal conductivity of the material Equation 36, based on a steady state solution from the the internal and external convection towards the wall.

The third thermal resistance is that associated with the natural convection between the tube walls and the fluid in the tank, hydrogen in this case. The same procedure is used as for the internal convective resistance, however a new Nusselt correlation is introduced for natural convection, with the outer tube diameter as reference dimension. The correlation of Churchill-Chu for natural convection in horizontal tubes is used, as shown in Equation 37.[59] However, it should however be noted that the predictions of empirical correlations may be inaccurate, especially in the unique case of a large liquid hydrogen tank. For example, Atayilmaz and Teke compared several natural convection correlations and CFD results for horizontal tubes and found deviations in the order of 20-50%.[60]

$$Nu_{tank} = \left( 0.6 + 0.387 \cdot \left( \frac{Ra}{\left[1 + (0.559/Pr_{tank})^{9/16}\right]^{16/9}} \right)^{1/6} \right)^2 \quad [37]$$

The Rayleigh and Grashof numbers are defined by Equation 38 and Equation 39. Here $\beta$ is the isobaric expansion coefficient of the fluid, which is retrieved from CoolProp, like the other thermodynamic properties of Hydrogen.

$$Ra = Pr_{tank} \cdot Gr \quad [38]$$

$$Gr = g \cdot \beta_{tank} \cdot D_{outer}^3 \cdot (T_{fluid} - T_{wall}) \cdot \left( \frac{\rho_{tank}}{\mu_{tank}} \right)^2 \quad [39]$$

The results of the NASA GODU experiment were used to validate the tank HEX model. One input variable was however not known from the experiment: the working fluid inlet pressure. Therefore, two validation strategies were attempted. In the first one, the inlet pressure was set such that the estimated heat duty matches to that reported for the experiment, while in the second one the inlet pressure was set such that the pressure drop matches the experimental value. The validation was repeated for two experimental datasets, featuring different temperatures of the liquid hydrogen inside the tank. The first dataset is for a hydrogen temperature of 20 K, while the second one for 17 K.

The validation results showed heat duty errors below 3% and pressure drop error values below 30%. The magnitude of these errors is similar to that of the uncertainty range found for the flow correlations. An in-depth report on the verification and validation of the tank HEX model can be found in Appendix D.

Additionally, a mesh independence study was performed to assess the minimum number of segments in which the tubes need to be discretized to properly capture the variation of the properties in the coolant. For the validation case, it was found that with 118 segments the variation in the estimate of the thermal duty was below 0.1%, assuming that the fully converged solution is equal to that of 600 segments. This error is deemed sufficiently low as it is significantly lower than the uncertainty of the flow correlations mentioned earlier.

## 2.6 Aftercooler model

The purpose of the RTBC aftercooler is to reduce the temperature of the cooling fluid after the compression. The heat duty of the aftercooler is determined given helium mass flow rate and the temperature difference between points 2 and 3 in the RTBC cycle. It

is approximately equal in magnitude to the compressor input power, as the thermal load in the tank HEX is limited.

For this study, an already existing plate-fin heat exchanger (PFHEX) optimization tool, developed by F. Beltrame and A. Baglieri, was used to size the aftercooler.[61] This program is capable of optimizing the geometry of PFHEXs for given design specifications and constraints. An offset strip fin (OSF) channel lay-out was selected for both streams of the HEX. This type of geometry is described by three non-dimensional geometric ratios.

- $\alpha$ - Fin spacing / fin height
- $\gamma$ - Fin thickness / fin spacing
- $\delta$ - Fin thickness / fin length

Note that the geometry of both the cold and the hot side of the PFHEX are defined by an independent pair of $\alpha$, $\beta$, and $\gamma$. However to limit the number of optimization variables, the values of $\alpha$, $\delta$, and$\gamma$ on the helium-side (hot side) are fixed to be 0.6, 0.048, and 0.07 respectively. These values were determined through optimization for several representative input conditions to the case study that is described in section 3. Additionally, the fin thickness and plate thickness in this study are fixed to 0.1 mm and 0.5 mm respectively.

The inlet conditions on the air-side of the aftercooler ($T_{reject}$ and $p_{reject}$) are deducted from the ambient temperature and pressure at a cruising altitude of 13 km using the standard atmospheric model, and taking into account the ram air compression in the intake. A velocity of 10 m/s was found to be representative for the average air-side flow inside the aftercooler and is therefore used to calculate the air-side inlet conditions using Equation 40 and Equation 41, which assume an ideal kinetic energy recovery in the intake.

$$\frac{T_{reject}}{T_{amb}} = \frac{1 + (\gamma - 1)/2 \cdot M^2_{cruise})}{1 + (\gamma - 1)/2 \cdot M^2_{HEX}} \quad [40]$$

$$\frac{p_{reject}}{p_{amb}} = \left(\frac{T_{reject}}{T_{env}}\right)^{\frac{\gamma}{\gamma-1}} \quad [41]$$

The mass flow rate of the air is determined by setting the heat capacitance ratio of the aftercooler to be equal to one, as shown in Equation 42.

$$\dot{m}_{air} = \dot{m}_{coolant} \cdot c_{p,coolant}/c_{p,air} \quad [42]$$

Once the heat duty, inlet conditions, and mass flow rates known, the PFHEX geometry is optimized to minimize the component weight using a Particle Swarm Optimization (PSO), within the specified constraints. Additionally, the values assumed for $\alpha$, $\beta$, and $\gamma$ must fall within the range for which the empirical correlations hold, namely:

- $\alpha$: 0.134 to 1.35
- $\gamma$: 0.021 to 0.121
- $\delta$: 0.012 to 0.048

The implemented PFHEX model is the result of several assumptions and simplifications. The model uses a single cell in which the averaged flow properties are evaluated to calculate the pressure drop and heat transfer. Additionally, the model assumes a perfectly developed flow and is not suited for large pressure drops where the effect of a pressure decrease on fluid density and thus on flow velocity is non-negligible.

Furthermore, the range of the Reynolds number on the two HEX sides, which are optimization variables of the design problem, have been constrained too. Notably, the cold side (air) Reynolds number is constrained between a value of 50 and 1000. Although the pressure drop of the helium-side flow is less critical than that of the air side, a lower maximum Reynolds number is imposed to prevent an excessively narrow PFHEX where the assumption of fully developed flow doesn't apply any more. Therefore the hot side (helium) Reynolds number is constrained between a value of 50 and a Reynolds number that corresponds to a HEX aspect ratio of 5.

Once the optimal geometry of the PFHEX is known, the mass of this component is used together with the results of the sizing procedure of the other components to calculate the overall mass and specific power of the RTBC.

## 3. Case study sensitivity analysis

A case study was analyzed to identify the specific power and efficiency range of an RTBC to achieve zero boil-off in a tank of a liquid hydrogen powered aircraft. For this study, the liquid hydrogen variant of TU Delft's flying-V aircraft was considered. The study by van Woensel,[62] "Integration of a Liquid Hydrogen Fuel Tank into the Concept of the Flying-V", was used to set the tank dimensions and the corresponding

boil-off rates.

This section provides an overview of the case study from the required inputs to the results. Finally, some considerations on the feasibility of ZBO for this case study are made.

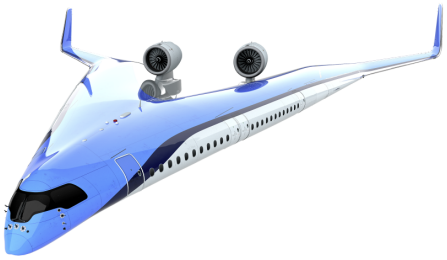

Fig. 17: TU Delft's Flying-V aircraft.[62]

## 3.1 Case study specifications and operating conditions

**Flight conditions**

For simplicity, only one operating condition of the aircraft is considered in the assessment of the RTBC performance, being the cruise phase. Therefore, the atmospheric conditions at a cruising altitude of 13 km are assumed in the study. The ambient pressure and temperature are calculated from the International Standard Atmosphere model, resulting in 0.165 bar and 216.7 K respectively. Furthermore, the cruise Mach number is kept constant at a value of 0.85.

**Turbomachinery**

Representative values for the compressor and turbine isentropic efficiencies were defined based on the results of previous studies.[28,25,63] The amount of available literature on the performance of helium compressors at power levels above 100 kW is however very limited, especially as most RTBCs are smaller than the one considered in this case study. The RTBC design from Lee et al.[17] was found to be most representative because of its relatively large cooling capacity and power consumption (31.3 kW). They demonstrated a compressor efficiency of 75% and a turbo-alternator efficiency of 86%, albeit for neon as a working fluid. A computational study in 2007 by Zhou et al.[64] showed an efficiency of 70-75% for a 2.37 kW compressor. Zagarola et al.[28] state that typical compressor power train efficiencies range from 40 to 70% with the potential of larger values for compressors of higher power levels. In 2011, a 500 W compressor prototype tested at Creare demonstrated an aerodynamic efficiency of 75%.[26] Based on these and other works on turbomachinery for RTBCs, the compressor and turbine isentropic efficiency values were assumed in this case study to be 75% and 85% respectively. Although higher efficiency values are potentially achievable, given that the turbomachinery efficiency tends to increase for larger devices, an in-depth study would be required to demonstrate the possible range of efficiency for helium compressors at power levels close to 100 kW. As mentioned earlier in subsection 2.3, the mass of the turbomachinery is not taken into account in the present RTBC model. Finally, none of the turbine power is recuperated in this case study and it therefore also isn't accounted for in the calculation of the COP.

**Fuel tank conditions**

The temperature and pressure of the liquid hydrogen inside the fuel tank are assumed to be constant and equal to 20 Kelvin and 1.75 bar respectively. Higher pressure values were also considered in the study of van Woensel.[62] However, they resulted in a considerably higher tank mass. Van Woensel's study covers different tank configurations of varying dimensions. Configuration 1 is used in this case study. The length of the fuel tank is fixed to a value of 10 meter. For this case study an equivalent radius of 3 meter is chosen as this allows the tank HEX to fit inside the elliptical fuel tank.

**Tank HEX inputs**

The number of tubes for the tank HEX is set to be 15. It should however be noted that the exact number of tubes that are necessary to provide sufficiently distributed cooling inside the liquid hydrogen tank would have to be determined by means of experimental tests or computational fluid dynamic simulations. The number chosen here is loosely based on the configuration used in NASA's GODU experiment.[6]

**Recuperator inputs**

The geometry of the recuperator is fixed, with exception of the length, which varies with the recuperator effectiveness. Values of CWHEX coil angles typically range from $70^o$ to $90^o$. In this study, a coil angle of $80^o$ has been used. Furthermore, the diameter of the recuperator is fixed to 0.5 meter, while the tubes have an outer diameter of 0.05 meter. The ratio of the recuperator's shell diameter to that of the central core

is fixed to a value of 4, yielding a total of 502 tubes spread over 23 concentric tube layers. An thickness of 10 mm was found to be sufficient for the outer shell insulation layer at a thermal conductivity of 0.02 W/mK, close to that of polyurethane foam at ambient temperatures.

All parts of the recuperator are made from Aluminium-5083, whose thermal conductivity is calculated as a function of the material temperature using Hust-Lankford's method as proposed by A. L. Woodcraft.[40]

**Aftercooler inputs**

The aftercooler effectiveness is fixed to a value of 80% and a maximum height of 0.3 meters is imposed. Due to the high temperatures that the working fluid experiences at high pressure ratios, the aftercooler is made from steel with a density of 8000 kg/m$^3$. The maximum allowable pressure drop of the air flow through the aftercooler was set to be 20% of the air inlet static pressure, namely 5268 Pa.

**Independent variables**

The following inputs are varied in the analysis: the recuperator effectiveness ($\epsilon_{recup}$), RTBC heat duty $\dot{Q}_{load}$, and the cycle pressure ratio ($PR$). Although the pressure ratio varies, the peak pressure of the cycle remains constant to a value of 20 bar.

The boil-off mass flow rates from van Woensel's study[62] were used to determine a relevant range of heat loads for the flying-V RTBC. These boil-off rates are converted to heat loads using the hydrogen's enthalpy of vaporization (445.6 kJ/kg). The range of variation of the pressure ratio was determined using the analytical solution presented in subsection 2.1. Note that not every possible combination of pressure ratio and recuperator effectiveness is feasible, as shown by Fig. 4. The range of variation of the independent variables of the analysis are as follows.

- $\epsilon_{recup}$: 96% to 98% (steps of 5%)
- $\dot{Q}_{load}$: 600, 1000, 1500, 2000 W
- $PR$: 2.5 to 8 (steps of 0.5)

The maximum length of a single recuperator is constrained to 5.5 meters such that it fits next to the fuel tank along the chord of the flying-V's wing. If the recuperator length exceeds this constraint, two (or more) shorter recuperators are used in series. In this case, the extra mass and length of the CWHEX components at both ends of the tube bundle is taken into account. However the additional pressure drops and thermal losses to connect the two shorter recuperators in series is not modeled in this study.

## 3.2 Case study results and discussion

Fig. 18 shows the ratio between the RTBC's COP and that of an ideal Carnot cycle as a measure of the cryocooler efficiency. These results are in good agreement with those predicted using the analytical RTBC model (subsection 2.1). The results confirm that there is an optimum pressure ratio that maximizes the RTBC COP. The influence of the cooling power on the RTBC's efficiency can be attributed to the decrease in the tank HEX effectiveness required to achieve larger cooling powers.

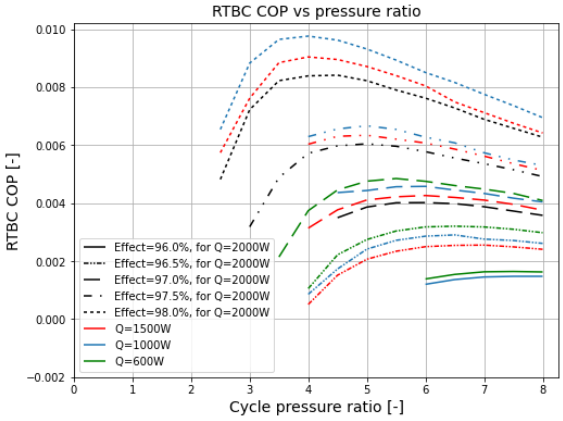


Fig. 18: COP estimated for the RTBC of the Flying-V case study.

The tank heat exchanger effectiveness of the different cases as function of the pressure ratio, recuperator effectiveness, and heat load can be seen in Fig. 19. The coolant mass flow rate was found to be strongly dependent on the tank HEX's effectiveness, which is to be expected. Mass flow rate values ranged from 0.031 kg/s to 0.22 kg/s at a pressure ratio of 8 and increase with decreasing pressure ratio. Particularly the combinations of low pressure ratios, low recuperator effectiveness, and high heat loads result in large mass flow rates.

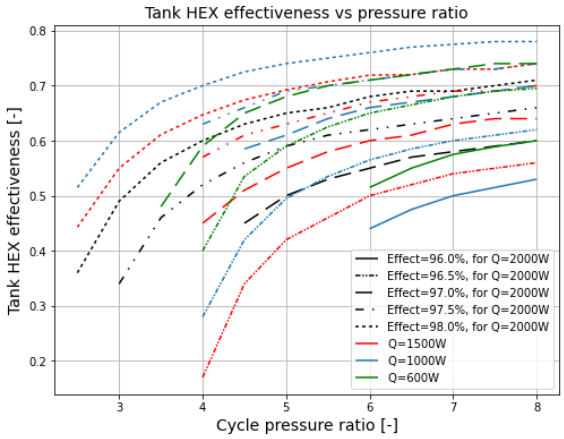


Fig. 19: Tank heat exchanger effectiveness results from the Flying-V case study.

Fig. 20 shows that the RTBC's mass decreases with increasing pressure ratio and that lower heat loads also lead to a lower cryocooler mass. At a pressure ratio of 8, nearly all cases result in an RTBC mass that falls in the range from 200 kg to 500 kg. The primary contributors towards the RTBC mass were found to be the tank HEX and recuperator, whose mass both decreases with increasing pressure ratio.

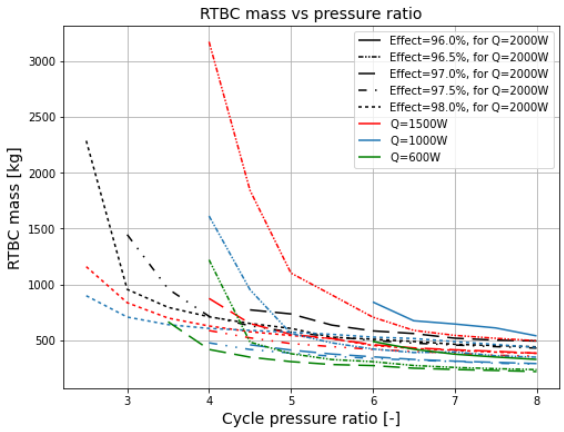


Fig. 20: RTBC mass for the Flying-V case study.

Evidently the recuperator length and mass increases with increasing the recuperator effectiveness, however the tank HEX mass decreases with increasing the recuperator effectiveness. This can be explained by the larger difference between $T_5$ and $T_6$ that is created by a higher effectiveness of the recuperator. The larger temperature difference will therefore require a smaller mass flow rate to achieve a given heat duty. This allows for smaller pipes in the tank HEX with the benefit of decreasing the weight of such component.

The decrease in RTBC mass at higher pressure ratios translates into an increasing specific power, as shown in Fig. 21. Although the RTBC mass increases with the heat load, the specific power also increases with the heat load. Additionally, there exists an optimum recuperator effectiveness that maximizes the RTBC specific power. For the considered cases in this study, the highest specific power values were achieved at an effectiveness of 97% or 97.5%, depending on the heat duty. The highest specific power values, at a pressure ratio of 8 were found to be 2.74 W/kg for 600 W, 3.51 W/kg for 1000 W, 4.20 W/kg for 1500 W, and 4.66 W/kg for 2000 W. It should however be noted that these values for the specific power have been calculated neglecting the mass of the turbomachinery, connecting pipes, and electronics and therefore they represent an overestimation.

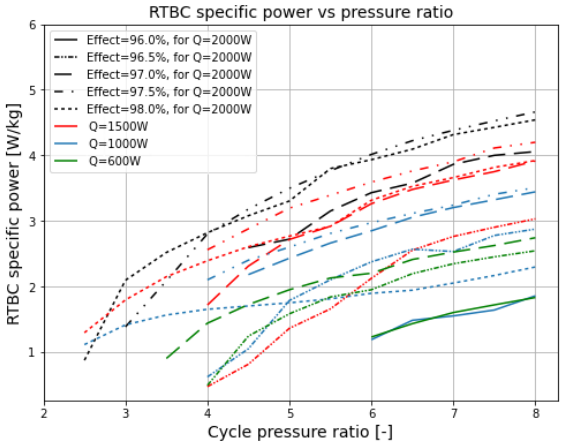


Fig. 21: RTBC specific power for the Flying-V case study.

The RTBC specific power can be plotted as function of the COP to facilitate the analysis of design trade-offs. This is shown in Fig. 22. Here it is apparent that for effectiveness values above 97.5%, the RTBC COP increases, however the specific power decreases.

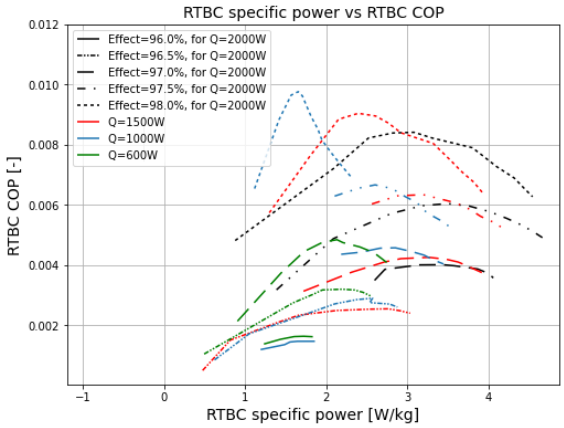


Fig. 22: Correlation between the RTBC specific power and coefficient of performance for the Flying-V case study.

Based on the RTBC performance, it is possible to make an estimate of how much the hydrogen mass is reduced by preventing boil-off. The change in hydrogen mass is equal to the additional amount of hydrogen mass that is required to power the RTBC ($\Delta m_{LH_2,power}$) minus the amount of hydrogen would have been boiled off ($\Delta m_{LH_2,boiloff}$). The former can be estimated, to a first approximation, based on the liquid hydrogen's lower heating value of 140 MJ/kg ($LHV$), flight time ($t$), COP, heat load ($\dot{Q}$), and the efficiency at which the hydrogen chemical energy can be converted to electrical power ($\eta_{conv}$). Assuming that the RTBC's heat load exactly matches the boil-off enthalpy change of the hydrogen, the amount of hydrogen that is not boiled off can be calculated using the flight time, heat load, and the hydrogen's specific enthalpy of evaporation ($\Delta h_{evap}$).

$$\Delta m_{LH_2} = \Delta m_{LH_2,power} - \Delta m_{LH_2,boiloff} \quad [43]$$

$$\Delta m_{LH_2} = \frac{\dot{Q} \cdot t}{COP \cdot LHV \cdot \eta_{conv}} - \frac{\dot{Q} \cdot t}{\Delta h_{evap}} \quad [44]$$

For this case study, a flight time of 8 hours and an energy conversion efficiency of 50% was used. The change in hydrogen mass achievable by adopting an RTBC for zero boil-off is shown in Fig. 23. It is apparent that only the RTBCs with a recuperator effectiveness of 98% yield a decrease in hydrogen mass larger than 10 kg. At 98% recuperator effectiveness, the savings in hydrogen mass are similar for cooling capacities of 1000 W and higher.

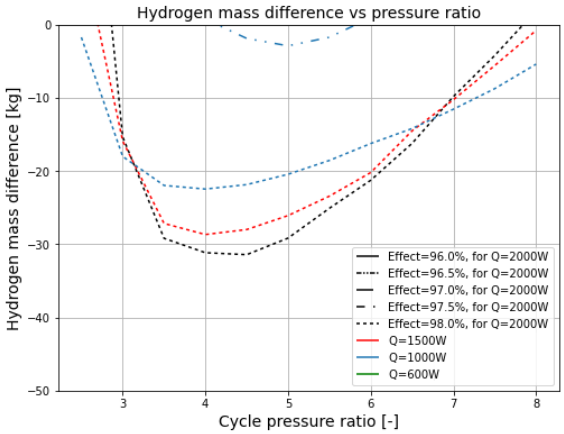


Fig. 23: Change in liquid hydrogen mass achievable through RTBC for the Flying-V case study. Only the cases with a mass reduction are shown.

The reduction in hydrogen mass will however also reduce the tank volume and thereby also the tank mass. The gravimetric storage density (GSD) from van Woensel's study[62] is used to correlate the change in hydrogen mass ($\Delta m_{LH_2}$) to the change in tank mass ($\Delta m_{tank}$), as shown in Equation 45.

$$\Delta m_{tank} = \Delta m_{LH_2} \cdot \left( \frac{1}{GSD} - 1 \right) \quad [45]$$

When combining the change in tank mass, change in hydrogen mass, and the mass of the RTBC itself, it is possible to assess the net total mass change, as shown by Equation 46. The total mass change for the different cases considered in this study is presented in Fig. 24.

From this figure it is clear that none of the considered RTBC cases allow for a decrease in the overall mass of the aircraft, assuming all other components of the aircraft have the same mass. Even for the best cases, the reduction in hydrogen and tank mass is not sufficient to offset the RTBC weight.

$$\Delta m_{tot} = \Delta m_{LH_2} + \Delta m_{tank} + \Delta m_{RTBC} \quad [46]$$

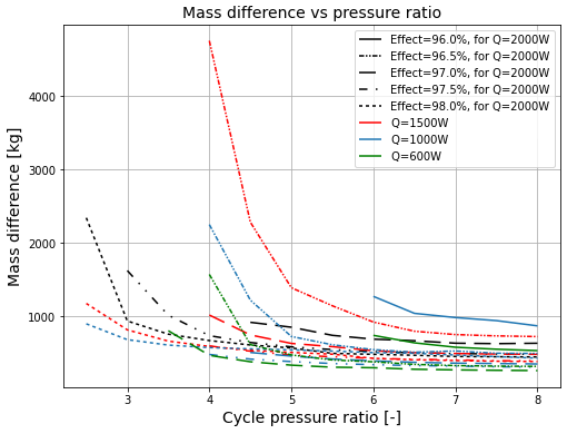


Fig. 24: Total change in mass by adopting an RTBC for the Flying-V case study.

### 3.3 Limitations of the study and recommendations

Based on the results of this study, several recommendations can be made for future improvements on the model's accuracy or for a better assessment of the feasibility of zero boil-off for liquid hydrogen-powered aircraft.

- It is highly recommended to implement a model for the compressor and turbomachinery preliminary design to compute a more representative estimate of the isentropic efficiencies than what done in this study, as the efficiencies were estimated based on literature sources for machines of smaller capacity or using different working fluids.
- The flow correlations for the natural convection inside the liquid hydrogen fuel tank feature a large uncertainty. Due to the low fidelity of empirical models for natural convection, it is recommended to perform a computational fluid dynamics analysis to obtain a more representative heat transfer correlation and evaluate the tank HEX's performance more accurately. Additionally, this analysis could also provide an indication for the required tube spacing in the liquid hydrogen tank to effectively achieve zero boil-off.
- The current study primarily focused on the RTBC itself and less on its implementation in the aircraft. Therefore it is recommended to evaluate the effects of including an RTBC on an aircraft, by for instance the design of the ram air duct used to cool the RTBC working fluid.
- Due to the large temperature difference that the aftercooler experiences, it is recommended to consider implementing a distributed parameter model for this cross-flow PFHEX to take the thermal conduction through the walls into account. Additionally, the effect of drag and/or thrust generated by the aftercooler exhaust on the aircraft's fuel consumption can be insightful regarding the feasibility of liquid hydrogen zero boil-off.
- It is recommended to perform an optimization on the RTBC CWHEX recuperator geometry to decrease its mass and thereby increase the cooler's specific power.
- It is recommended to quantify the heat leak and pressure losses associated with the piping that connects the different RTBC components and thereby propose a preferential placement of these components inside the aircraft.
- A relatively simple structural model was implemented to calculate the wall thicknesses of the CWHEX. It is therefore recommended to implement a more thorough structural model that takes the various combined operating loads into account. Especially the required stiffness of the coiled tubes and spacers necessary to maintain the positioning and shape. Similarly, the design of the tank heat exchanger's structural supports can be optimized to reduce weight, heat leak, and thermal resistance.
- In this study, a coil-wound heat exchanger model was implemented for the RTBC's recuperator. Although this HEX was deemed to be the most promising for this application, it is recommended to implement also other heat exchanger configurations to compare their performance for RTBC technology.

## 4. Conclusion

The use of liquid hydrogen as a fuel source for aircraft poses many challenges. A technology that may enable fuel and mass saving is that of a reverse turbo-Brayton cryocooler (RTBC) to achieve hydrogen zero boil-off in the tank. Therefore an RTBC simulation tool was developed in this study that allows for an estimate of the coefficient of performance and specific power by modeling the performance of the six main RTBC components: compressor, turbine, aftercooler, recuperator, and tank heat exchanger. There was a strong focus on the latter three due to their large contribution to the RTBC total mass. For this reason,

only the preliminary design of the HEXs has been performed in the study, while for turbomachinery only their performance is modeled through simple thermodynamic relations based on the isentropic efficiency definition. The aftercooler preliminary design and optimization has been carried out by using an in-house code. For the recuperator, a coil-wound HEX, a detailed discretized model was created that takes several relevant phenomena into account such as axial conduction, heat leak from the environment, pressure drop, and fluid properties variation along the recuperator. Finally, the tank heat exchanger was also simulated by means of a distributed parameter model.

A case study was analyzed. This is that of on a liquid hydrogen fuel variant of the Flying-V aircraft proposed at TU Delft. The RTBC pressure ratio, heat load, and recuperator effectiveness were varied to assess the influence of these variables on the design of the cryocooler, with the ultimate goal of assessing the technical feasibility of the use of a cryocooler to achieve zero boil-off. Although the results indicate a hydrogen mass reduction for those design solutions characterized by high recuperator effectiveness, none of the cases showed a sufficiently large reduction in hydrogen and tank mass to offset the cryocooler weight. Given that the weight estimates performed in this study are an optimistic approximation, it can be concluded that the use of an RTBC onboard TU Delft's Flying-V is not a viable option. The performance of the individual RTBC components would have to be improved to make RTBC technology feasible for future hydrogen fueled aircraft.

## References

[1] NASA, "Liquid hydrogen as a propulsion fuel, 1945-1959," *National Aeronautics and Space Administrations*, vol. SP-4404, 1978.

[2] V. Sosounov and V. Orlov, "Experimental turbofan using liquid hydrogen and liquid natural gas as fuel.," *AIAA/SAE/ASME/ASEE 26th Propulsion Joint Specialist Conference*, 1990.

[3] D. W. Plachta, "Hybrid thermal control testing of a cryogenic propellant tank," *Cryogenic Engineering and International Cryogenic Materials Conference*, 1999.

[4] L. J. Hastings, C. Bryant, R. Flachbart, K. Holt, E. Johnson, A. Hedayat, B. Hipp, and D. W. Plachta, "Large-scale demonstration of liquid hydrogen storage with zero boiloff for in-space applications," 2010.

[5] D. W. Plachta, "Results of an advanced development zero boil-off cryogenic propellant storage test," 2004.

[6] A. M. Swanger, W. U. Notardonato, W. L. Johnson, and T. M. Tomsik, "Integrated refrigeration and storage for advanced liquid hydrogen operations," *NASA Technical Report Server*, 2016.

[7] Linde, "Standard helium refrigerator lr1420/lr1620," 2019. Last retrieved on 7/11/2023.

[8] W. L. Richards, M. L. Meyer, J. R. Feller, A. C. Rhodes, S. Rosner, D. Stefanovic, and A. Kashani, "Cryogenic technologies for the stratospheric observatory for infrared astronomy (sofia) science instruments," *NASA Technical Report Server*, 2020.

[9] J. J. Breedlove, P. J. Magari, and G. W. Miller, "Cryocooler for air liquefaction onboard large aircraft," *Advances in cryogenic engineering*, vol. Vol.33, pp. pp.838–845, 2008.

[10] R. C. Bowman, "Brilliant eyes ten-kelvin sorption cryocooler experiment (betsce): Final report," pp. pp. 833–839, 1997.

[11] M. O. Kimball, ed., *GSFC Adiabatic Demagnetization Refrigerator*. NASA Goddard Space Flight Center, Greenbelt, 2014.

[12] W. Swift, J. McCormack, M. Zagarola, D. F.X., and S. H., "The nicmos turbo-brayton cryocooler — two years in orbit," *Cryocoolers*, vol. Vol. 13, pp. pp. 633—639, 2004.

[13] L. J. Hastings, D. W. Plachta, S. Salerno, and P. Kittel, "An overview of nasa efforts on zero boiloff storage of cryogenic propellants," *Cryogenics*, vol. 41, pp. pp. 833–839, 2002.

[14] ESA, "Zero-boil off propulsion system feasibility demonstration," 2017.

[15] R. J. Christie, T. M. Tomsik, J. P. Elchert, and M. C. Guzik, "Broad area cooler concepts for cryogenic propellant tanks," *Thermal Fluids Analysis Workshop*, 2011.

[16] S. Qian, J. Yu, and G. Yan, "A review of regenerative heat exchange methods for various cooling technologies," *Renewable and Sustainable Energy Reviews*, vol. Vol.69, pp. pp.535–550, 2017.

[17] K. Lee, D. Koh, J. Ko, H. Yeom, C. Son, and J. Yoon, "Design and performance test of 2 kw class reverse brayton cryogenic system," *Energies*, vol. Vol.13, 2020.

[18] S. Yang, B. Fu, Y. Hou, S. Chen, Z. Liu, and S. Wang, "Transient cooling and operational performance of the cryogenic part in reverse brayton air refrigerator," *Energy*, vol. Vol.167, pp. pp.921–938, 2019.

[19] S. Yang, B. Fu, and Z. Liu, "Simulation and evaluation on the dynamic performance of a cryogenic turbo-based reverse brayton refrigerator," *Energy*, vol. Vol.167, pp. pp.921–938, 2019.

[20] D. Deserranno, Z. M., D. Craig, R. Garehan, T. Giglio, J. Smith, J. Sanders, and M. Day, "Performance testing of a high effectiveness recuperator for high capacity turbo-brayton cryocoolers," *Cryocoolers*, vol. Vol.19, 2016.

[21] M. V. Zagarola, W. L. Swift, H. Sixsmith, J. A. McCormick, and M. G. Izenson, "Development of a turbo-brayton cooler for 6 k space applications," *International Cryocooler Conference*, vol. Vol.12, 2003.

[22] R. W. Hill, M. G. Izenson, W. B. Chen, and M. V. Zagarola, "A recuperative heat exchanger for space-borne turbo-brayton cryocoolers," *Cryocoolers*, vol. Vol.14, 2007.

[23] H. ter Brake and G. Wiegerinck, "Low-power cryocooler survey," *Cryogenics*, vol. Vol.42, no. No.11, pp. pp. 705–718, 2002.

[24] T. Strobridge, "Cryogenic refrigerators: An updated survey," *National Institute of Standards and Technology*, 1974. Last retrieved on 7/11/2023.

[25] K. Cragin, J. McCormick, and M. V. Zagarola, "Development of a cryogenic compressor for airborne cryocoolers," *IOP Publishing*, 2020.

[26] R. Hill, J. Hilderbrand, and M. Zagarola, "An advanced compressor for turbo-brayton cryocoolers," *Cryogenics*, vol. Vol.16, 2011.

[27] M. V. Zagarola, K. Cragin, and J. McCormick, "Operation of gas bearings at cryogenic temperatures," *Cryogenics*, 2019.

[28] M. Zagarola, D. Desserano, X. Li, and S. Mustafi, "Optimization of a brayton cryocooler for zbo liquid hydrogen storage in space," *Cryogenics*, 2014.

[29] L. Chen, X. Zhang, R. Xiao, Z. Zhang, S. Chen, and Y. Hou, "A reverse turbo-brayton cycle cryocooler for zbo storage of liquid hydrogen in space," *Applied Energy Symposium*, 2022.

[30] C. Gondrand, F. Durand, F. Delcayere, S. Crispel, and G. M. Gistau Baguer, "Overview of air liquide refrigeration systems between 1.8 k and 200 k," *Advances in Cryogenic Engineering*, vol. Vol.13, pp. pp.949–956, 2014.

[31] R. K. Shah and D. P. Sekulic, *Fundamentals of heat exchanger design*. John Wiley & Sons Inc, Hoboken (USA), 2003.

[32] J. C. Pacio and C. A. Dorao, "A review on heat exchanger thermal hydraulic models for cryogenic applications," *Cryogenics*, vol. 51, no. 7, pp. 366–379, 2011.

[33] T. Wang, G. Ding, Z. Duan, T. Ren, J. Chen, and H. Pu, "A distributed-parameter model for lng spiral wound heat exchanger based on graph theory," *Applied Thermal Engineering*, vol. Vol.81, 2015.

[34] Y. Ren, W. Cai, J. Chen, L. Lu, J. Wand, and Y. Jiang, "The heat transfer characteristics of shell-side film flow in spiral wound heat exchanger under rolling working conditions," *Applied Thermal Engineering*, vol. 132, 2017.

[35] S. Hosseinian, A. M. Abolmaali, and H. Afshin, "An analytical method for spiral-wound heat exchanger: design and cost estimation considering temperature-dependent fluid properties," *International Journal of Numerical Methods for Heat and Fluid Flow*, 2020.

[36] A. M. Abolmaali and H. Afshin, "A design model for spiral wound heat exchangers which accounts for property variation, longitudinal heat conduction and heat-in-leak," *Applied Thermal Engineering*, vol. Vol.218, 2023.

[37] I. H. Bell, J. Wronski, S. Quoilin, and V. Lemort, "Pure and pseudo-pure fluid thermophysical property evaluation and the open-source thermophysical property library coolprop," *Industrial & Engineering Chemistry Research*, vol. Vol. 53, no. No. 6, pp. pp. 2498–2508, 2014.

[38] H. G. Groehn, "Increase of heat exchanger efficiency for yawed tube banks," *Nineth International Heat Transfer Conference*, vol. Vol. 5, pp. pp. 73–78, 1990.

[39] R. C. Byrne, "Standards of the tubular exchanger manufacturers association, ninth edition," 2019.

[40] A. L. Woodcraft, "Predicting the thermal conductivity of aluminium alloys in the cryogenic to room temperature range," *Cryogenics*, vol. Vol.45, No.6, 2005.

[41] M. S. Bhatti and R. K. Shah, "Laminar convective heat transfer in ducts," *Handbook of Single-Phase Convective Heat Transfer*, vol. Chapter 3, 1987.

[42] M. Van Dyke, "Extended stokes series: Laminar flow through a loosely coiled pipe," *Journal of fluid mechanics*, vol. Vol. 86, no. No.1, pp. pp. 129–145, 1978.

[43] P. Mishra and S. N. Gupta, "Momentum transfer in curved pipes. i. newtonian fluids, ii. non-newtonian fluids," *Industrial and Engineering Chemistry Process Design and Development*, vol. Vol. 18, pp. pp. 130–142, 1979.

[44] H. Ito, "Friction factors for turbulent flow in curved pipes," *Journal of Basic Engineering*, pp. pp. 123–134, 1959.

[45] M. L. Manlapaz and S. W. Churchill, "Fully developed laminar flow from a helical coil," *Chemical Engineering Communications*, vol. Vol. 9, pp. pp. 185–200, 1981.

[46] B. S. Petukhov and V. N. Popov, "Theoretical calculation of heat exchange in turbulent flow in tubes of an incompressible fluid with variable physical properties," *High Temp.*, vol. Vol. 1, no. No.1, pp. pp. 69–83, 1963.

[47] P. S. Srinivasan, S. S. Nandapurkar, and F. A. Holland, "Friction factors for coils," *Transactions of the Institution of Chemical Engineers*, vol. Vol. 48, pp. pp. 156–161, 1970.

[48] C. E. Kalb and J. D. Seadler, "Fully developed viscous-flow heat transfer in curved circular tubes with uniform wall temperature," *American Institute of Chemical Engineers Journals*, vol. Vol. 20, p. pp. 340, 1974.

[49] E. F. Schmidt, "Heat transfer and pressure loss in coiled tubes," *Chem. Eng. Tech.*, vol. Vol. 39, pp. pp. 781–789, 1967.

[50] G. F. C. Rogers and Y. R. Mayhew, "Heat transfer and pressure loss in helically coiled tubes with turbulent flow," *International Journal for Mass and Heat transfer*, vol. Vol. 7, pp. pp. 1207–1216, 1964.

[51] C. M. White, "Streamline flow through curved pipes," *Proceedings of Royal Society of London*, vol. Vol. 123, pp. pp. 645–663, 1929.

[52] A. Žukauskas, "Heat transfer from tubes in crossflow," *Advances in heat transfer*, vol. Vol. 8, pp. pp. 93–160, 1972.

[53] E. E. Abadzic, "Heat transfer on coiled tubular matrix," *ASME winter annual meeting*, 1974.

[54] T. Kim, "Effect of longitudinal pitch on convective heat transfer in crossflow over in-line tube banks," *Annals of Nuclear Engineering*, vol. Vol. 57, pp. pp. 209–215, 2013.

[55] R. F. Le Feuvre, "A method of modeling the heat transfer and flow resistance characteristics of multi-start helically-coiled tube heat exchangers," *Eighth International Heat Transfer Conference*, vol. Vol. 6, pp. pp. 1–41, 1986.

[56] NIST, "Material properties: 304 stainless (uns s30400)," *National Institute for Standards and Technology, Applied Chemicals and Materials Division*. Last accessed on 01/08/2023. `https://trc.nist.gov/cryogenics/materials/304Stainless/304Stainless_rev.htm`.

[57] D. Mann, *LNG materials and fluids: a user's manual of property data in graphic format*. John Wiley & Sons Inc, Hoboken (USA), 1977.

[58] Y. Touloukian and C. Ho, "Thermophysical properties of selected aerospace materials, part ii: Thermophysical properties of seven materials," *International Journal of Heat and Mass Transfer*, pp. pp. 39–46, 1976.

[59] S. W. Churchill and H. H. S. Chu, "Correlating equations for laminar and turbulent free convection from a horizontal cylinder," *International Journal of Heat and Mass Transfer*, vol. Vol. 18, no. No.9, pp. pp. 1049–1053, 1975.

[60] S. O. Atayilmaz and I. Teke, "Experimental and numerical study of the natural convection from a heated horizontal cylinder," *International Communications in Heat and Mass Transfer*, vol. Vol. 36, no. No.7, pp. pp. 731–738, 2009.

[61] A. Baglieri, "Plate fin heat exchanger design optimization and mass-specific performance assessment for aerospace applications," 2023.

[62] C. V. C. van Woensel, "Integration of a liquid hydrogen fuel tank into the concept of the flying-v," *TU Delft Repository*, 2021.

[63] L. Zhou, D. Acharya, D. Jayanta, C. Louis, and A. Nagaraj, "Aerodynamics performance test of a high-speed miniature centrifugal compressor," *ASME Energy Sustainability Conference*, pp. pp. 371–378, 2007.

[64] L. Zhou, D. Acharya, J. Kapat, and L. Chow, "Aerodynamics performance test of a high-speed miniature centrifugal compressor," *Energy Sustainability Conference*, 2007.

## Appendix A - RTBC Analytical model

$$COP = \frac{c_{p_C}}{c_{p_H}} \cdot \frac{\eta_{comp}}{\left[PR^{\frac{\gamma_H - 1}{\gamma_H}} - 1\right]} \cdot \frac{T_6 - (T_3 - \epsilon_{recup} \cdot (T_3 - T_6)) \cdot \left[1 - \eta_{turb} \cdot \left(1 - \frac{1}{PR^{\frac{\gamma_C - 1}{\gamma_C}}}\right)\right]}{T_6 + \epsilon_{recup} \cdot (T_3 - T_6)} \quad [47]$$

Here the term $T_3$ can be substituted by:

$$T_3 = \frac{\epsilon_{reject} \cdot T_{reject} + T_6 \cdot (1 - \epsilon_{recup}) \cdot (1 - \epsilon_{reject}) \cdot \left[1 + \frac{1}{\eta_{comp}} \cdot \left(PR^{\frac{\gamma_H - 1}{\gamma_H}} - 1\right)\right]}{1 - \epsilon_{recup} \cdot (1 - \epsilon_{reject}) \cdot \left[1 + \frac{1}{\eta_{comp}} \cdot \left(PR^{\frac{\gamma_H - 1}{\gamma_H}} - 1\right)\right]} \quad [48]$$

And $T_6$ can be substituted by:

$$\begin{cases} T_6 = \frac{\frac{\epsilon_{load} \cdot T_{load} + A/C}{1 - \epsilon_{rec} \cdot (1 - \epsilon_{load}) \cdot \left[1 - \eta_{turb} \cdot \left(1 - \frac{1}{PR^{\frac{\gamma_C - 1}{\gamma_C}}}\right)\right]} - B/C}{} \\ A = T_{reject} \cdot \epsilon_{rej} \cdot (1 - \epsilon_{load}) \cdot (1 - \epsilon_{recup}) \cdot \left[1 - \eta_{turb} \cdot \left(1 - \frac{1}{PR^{\frac{\gamma_C - 1}{\gamma_C}}}\right)\right] \\ B = (1 - \epsilon_{load}) \cdot (1 - \epsilon_{recup})^2 \cdot (1 - \epsilon_{reject}) \cdot \left[1 - \eta_{turb} \cdot \left(1 - \frac{1}{PR^{\frac{\gamma_C - 1}{\gamma_C}}}\right)\right] \cdot \left[1 + \frac{1}{\eta_{comp}} \cdot \left(PR^{\frac{\gamma_H - 1}{\gamma_H}} - 1\right)\right] \\ C = 1 - \epsilon_{recup} \cdot (1 - \epsilon_{load}) \cdot \left[1 - \eta_{turb} \cdot \left(1 - \frac{1}{PR^{\frac{\gamma_C - 1}{\gamma_C}}}\right)\right] \end{cases} \quad [49]$$

## Appendix B - Tank heat exchanger program logic diagram

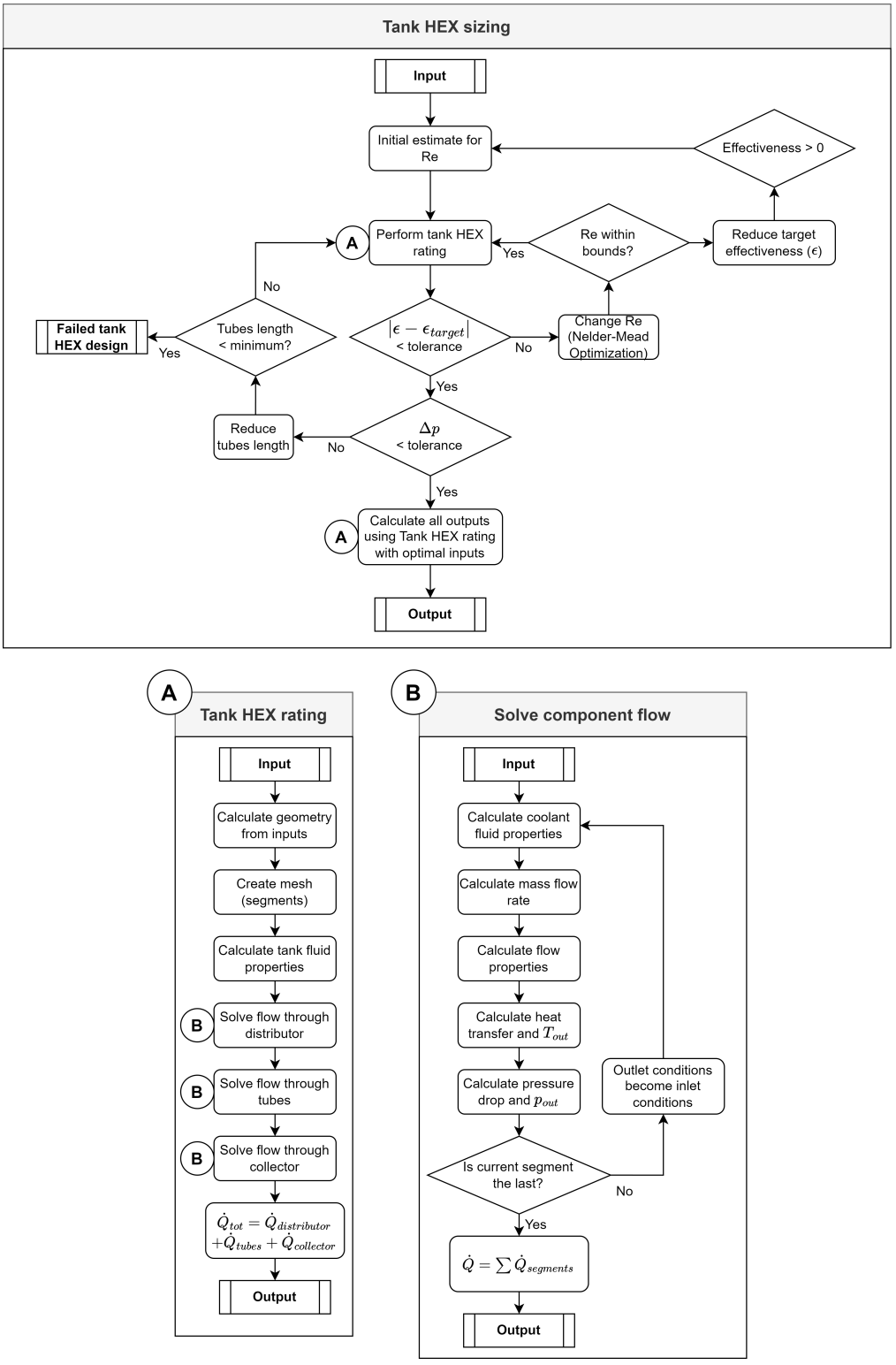


Fig. 25: Tank heat exchanger program logic diagram.

# Appendix C

# Thermodynamic modeling of gaseous flow through a coil-wound heat exchanger

## — Overview of flow correlations —

By Thomas Britting,

Supervised by C. De Servi and F. Beltrame

In partial fulfillment of the MSc thesis

# 1. Introduction

To calculate the performance of a counter-flow, coil-wound heat exchanger, it is necessary to model the thermodynamic behaviour of the two fluids. For this study, both the cold and hot fluid streams are gaseous helium-4 and feature the same mass flow rate as they are part of a closed loop within a cryocooler. Two parameters of the flow are of key interest: firstly the heat transfer coefficient between the fluid and surrounding solid walls, and secondly average pressure drop that the fluid experiences when flowing through the heat exchanger. Because the heat exchanger model is constructed to be a distributed parameter model, the pressure drop and heat transfer coefficient are calculated at each control volume of the heat exchanger. This chapter aims to provide an overview of the correlations that are used to calculate the pressure drop and heat transfer coefficient.

First, in section 2 an explanation is provided of the generalized approach that is taken to correlate the various flow and fluid properties to the heat transfer coefficient and pressure drop of the coil-wound heat exchanger. Secondly, the correlations for flow through a coiled tube, and tubeflow in general, are presented in section 3. Thereafter the correlations of flows through tube banks and specifically the flow through spirally-wound, cross-inclined tube banks, are discussed in section 4. Finally, the modelling approach of the heat transfer and pressure drop behaviour of the fluid that flows near the encapsulating walls of the heat exchanger is explained in section 5. In each section, the correlations for the heat transfer coefficient and pressure drop will be covered separately.

# 2. Overview of correlations

The interaction between the fluids in the heat exchanger and the different metal walls are modelled by using several simplifications and correlations. In terms of heat transfer and pressure drop calculations, the heat exchanger is split in five regions, which each their own correlations. A visual representation of this division can be seen in Figure 1, and a description can be found in subsection 2.1 and subsection 2.2 for the tubeflow and shellflow respectively.

It should be noted that model presented in this study assumes that the helium flowing through the heat exchanger can be approximated by a pure substance (Helium in this case). Additionally, the effect of fouling can be neglected as the fluid circulates in a closed circuit, reducing the potential sources of contamination. Furthermore, the flow is assumed to be fully developed all along the heat exchanger, for both streams. For all the cases that were encountered in this study, the length of the tubes was at least one order magnitude longer than the length required for the flow to fully develop. Regarding the shellflow, Žukauskas [1972] showed that after passing over 20 tubes, there is virtually no more change in the Nusselt number from the fully-developed state.

## 2.1. Tubeflow

The tubeflow is modeled using two different correlations. The inlet regions of the tubes use the correlations of straight circular tubes (1), as there is no coiling happening in the tubeflow region (2). For these correlations, the reader is referred to subsection 3.3 and subsection 3.1. In the central region of the heat exchanger, the tubeflow is modelled as a coiled circular tube, for which the correlations can be found in subsection 3.3 and subsection 3.2.

## 2.2. Shellflow

The shellflow interacts with three different types of walls in the heat exchanger: firstly the coiled tubes (3), secondly the walls of the heat exchanger's outer shell and core (4), and thirdly the straight tubes in the entrance regions of the heat exchanger (5). The heat and momentum transfer between the shellflow and these three walls is modelled using the correlations described in this chapter. The correlations for the flow over the coiled tubes (3) and straight tube banks (5) are presented in section 4 and the correlations for the flow interaction with the walls (4) in section 5.

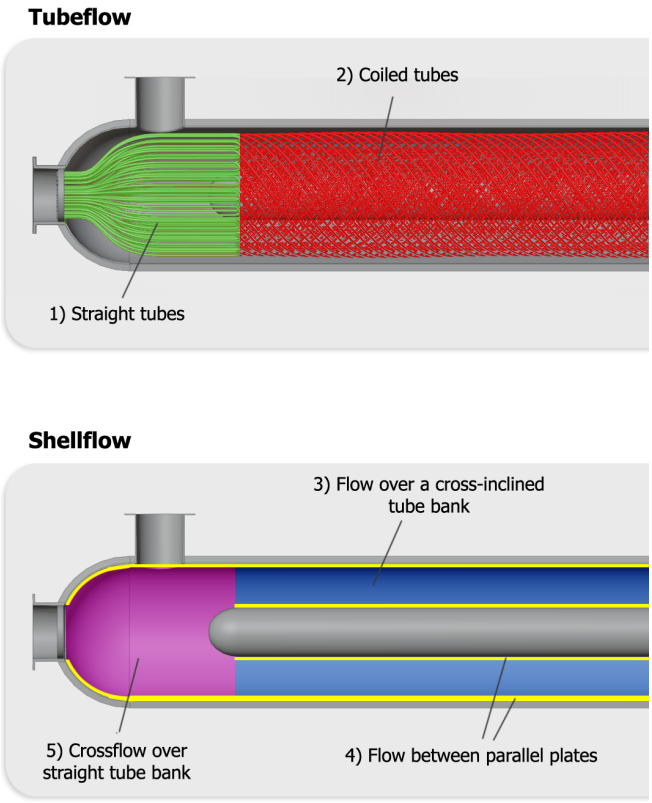


Figure 1: Visual overview of where the different correlations for the heat transfer coefficient and pressure drop correlations are applied to the coiled-wound heat exchanger.

## 2.3. Pressure drop and heat transfer coefficient calculations

Most correlations that exist in literature don't directly make use of a heat transfer coefficient (h), but instead provide the Nusselt number ($Nu$), which can be correlated to the Reynolds number of the flow and often also geometry-dependant parameters. In combination with the local fluid thermal conductivity ($k$) and a reference dimension ($x_{ref}$), it is possible to calculate the heat transfer coefficient using Equation 1. It should be noted that the reference dimension should be consistent with the one that is used to compute the Nusselt number. [Shah and Sekulic, 2003]

$$h = \frac{Nu \cdot k}{x_{ref}} \tag{1}$$

There are several methods on how to calculate how much pressure drop an internal flow will experience. An often used parameter is the friction factor, of which two variants exist: the Fanning friction factor, and the Darcy-Weisbach friction factor. The latter is equal to four times the Fanning

friction factor. To avoid confusion, in this work, only the Fanning friction factor is used and henceforth denoted by $f$. From the Fanning friction factor, the pressure drop ($\Delta P$) can be calculated using Equation 2. In this equation, the hydraulic diameter represents the diameter of a circular tube that is representative to the actual tube crossection. The length, $L$, denotes the distance along which the fluid travels for which the pressure drop is to be calculated. [Shah and Sekulic, 2003]

$$\Delta p = \cdot f \cdot L \cdot \rho \cdot V / (2 \cdot D_h). \tag{2}$$

An alternative method for calculating the pressure drop of a fluid stream is the use of a pressure drop coefficient ($\xi$). This method is more common for flow through complex geometries, such as for example valves, where the use of Equation 2 doesn't provide an accurate or practical solution due to the complexity of the flow path. In general, pressure drop coefficients are calculated from experimental results or computational fluid dynamic simulations. This method is also used in this work to calculate the pressure drop over tube banks, as will be explained in subsection 4.4. The equation that is used to correlate the pressure drop with the pressure drop coefficient is presented in Equation 3. [Shah and Sekulic, 2003]

$$\Delta p = \xi \cdot 0.5 \cdot \rho \cdot V^2 \tag{3}$$

# 3. Tubeflow correlations

In coil-wound heat exchangers, one of the two fluids travels through the many coiled tubes. The behaviour of flows through tubes has been well understood, as there is an extensive number of publications that present various correlations that describe the thermodynamic and hydrodynamic change of properties, such as heat exchange and momentum loss to the surrounding wall. An overview of the most relevant literature on flow through straight tubes is presented in subsection 3.3 and subsection 3.1, for the heat transfer coefficient and friction factor respectively. The different pressure drop behaviour of flow through coiled tubes, in contrast to straight to tubes, is explained in subsection 3.2.

## 3.1. Pressure drop coefficient of flow in tubes

**Laminar flow**

For laminar flow through a straight tube, the fanning friction factor is typically independent from the Prandtl number. An often used correlation for the laminar flow through straight pipes is that of the Hagen-Poiseille flow, Equation 4, as stated by Shah and Sekulic [2003] (Chapter 7). This correlation holds until the critical Reynolds number ($Re_{cr}$) is reached, when the flow starts transitioning from laminar to turbulent (see transitional flow below). For straight tubes, the critical Reynolds number is taken to be 2100.

$$f_{lam} = 16/Re \tag{4}$$

**Turbulent flow**

In turbulent flow through circular tubes, the friction coefficient typically does depend on the roughness of the pipe. The effect of roughness on the pressure drop in the tubeflow is considered out of the scope for this study, and thus perfectly smooth circular tubes are used.

Bhatti and Shah [1987] presented a semi-empirical correlation that can be used for turbulent flow and also for transitional flow, albeit with different coefficients, as shown in Equation 5.

$$f_{turb} = 0.00128 + 0.1143 \cdot Re^{-1/3.2154} \tag{5}$$

**Transitional flow**

The accuracy of semi-empirical correlation for the modeling of transitional flow is relatively low due to the unsteady and chaotic nature of flow transition. Therefore the results of the heat exchanger simulation code presented in this work should be questioned for their correctness when flow transition is encountered throughout the heat exchanger. In practice, the model's equations for flow transition rather serve to act as a continuous function from the laminar to the turbulent regime during the iterations.

Specifically for the fanning friction factor of transitional flow in straight tubes, the transitional correlation (Equation 6) from Bhatti and Shah [1987] is used as it provides a continuous function between the laminar and turbulent function.

$$f_{trans} = 0.0054 + 2.3 \cdot 10^{-8} \cdot Re^{3/2} \tag{6}$$

## 3.2. Pressure drop correlations for coiled tubes

Shah and Zhou [2004] presented an extensive literature survey of the various correlations for the friction coefficient of coiled tubes, alongside with an overview of the flow behaviour that makes it distinct from straight tubes. The flow through coils behaves differently from that through straight tubes, as the curvature gives rise to a secondary flow in the tubes that tends to stabilize the flow and thereby delays flow transition to a higher Reynolds number. Several authors have proposed a correction method to calculate the critical Reynolds number for coiled tubes, using the non-dimensional Dean number ($De$), based on the work of Dean [1927] and Dean [1928]. The Dean number is an a modified expression of the Reynolds number that takes into account the effect of coiling by means of the following expression:

$$De = Re \cdot \left( \frac{D_{tube}}{2 \cdot R_{coil}} \right)^{0.5} \tag{7}$$

Here the ratio of the tube radius ($D_{tube}/2$) and the coiling radius ($R_{coil}$) of the tube are used to compute the Dean number. There have been several correlations suggested to correct the critical Reynolds number for the coiling of the tubes. Srinivasan et al. [1970] suggested an improved relation, Equation 8, of that of Ito [1959] for the critical Reynolds number of flow through coiled tubes.

$$Re_{cr,coiling} = 2100 \cdot \left( 1 + 12 \cdot \left( \frac{D_{tube}}{2 \cdot R_{coil}} \right)^{0.5} \right) \tag{8}$$

The coiling doesn't only increase the critical Reynolds number, but also causes a more gradual transition from laminar to turbulent flow, making it more difficult to clearly identify at what Reynolds numbers laminar flow ends and and where fully turbulent flow begins.

**Laminar flow**

The paper of Shah and Zhou [2004] provides an clear overview of the different equations that have been proposed by various authors to correct for the increased friction factor in case of coiled tubes. A total of 14 different correlations were proposed for laminar flow, each with different applicable ranges in terms of Reynolds number, Dean number, or other criteria. The correlation of Mishra and Gupta [1979] (Equation 9) was chosen for this work for its wide applicable range, being: $1 < De < 3000$. When the Dean number is lower than 1, the friction value is nearly identical to that of straight tubes.

$$\frac{f_{lam,coiled}}{f_{lam}} = \left\{1 - \left[1 - \left(\frac{11.6}{De}\right)^{0.45}\right]^{1/0.45}\right\}^{-1} \tag{9}$$

**Turbulent flow**

Shah and Zhou [2004] also presented three equations from Ito [1959], Srinivasan et al. [1970], and Mishra and Gupta [1979] that correct the turbulent friction factor for turbulent flow. As shown in Figure 2, the three correlations show very good agreement to each other. The correlation of Ito (Equation 10) is selected for this work, because of its wide range of applicability.

$$f_{turb,coiled} = \frac{1}{4}\left(\frac{D_{tube}}{2 \cdot R_{coil}}\right)^{\frac{1}{2}} \left\{0.029 + 0.304\left[Re\left(\frac{D_{tube}}{2 \cdot R_{coil}}\right)^{2}\right]^{-0.25}\right\} \tag{10}$$

**Transitional flow**

Due to the lack of sufficient literature about the effect of tube coiling on the friction factor and heat transfer coefficient in the transitional flow regime, a direct transition from the laminar to turbulent flow correlation is used in this work.

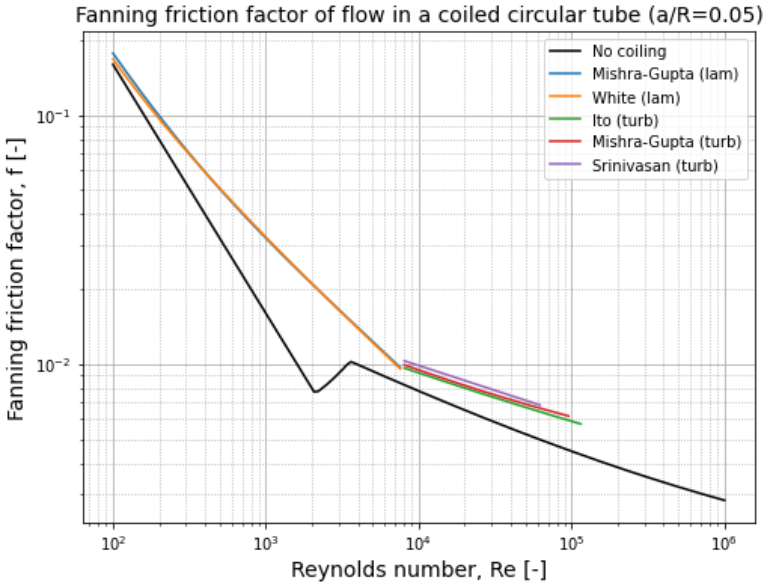


Figure 2: Comparison of three coiled tube flow correlations for the Fanning friction factor (for a ratio of minor over major coil diameter of 0.05 and Prandtl number of 0.7), as compared to the Fanning friction factor of a straight tube.

## 3.3. Nusselt number of flow in coiled tubes

When there exists a temperature difference between the fluid and the tube wall, there is an exchange of heat that takes place between the two. In order to calculate the convective heat transfer coefficient ($U$), a correlation for the flow's Nusselt number ($Nu$) is required. In this section, the Nusselt number of flow through coiled, circular tubes is presented, for the laminar, turbulent, and transitional flow regime. These correlations make use of either the Dean number ($De$) or the ratio of the tube radius ($D_{tube}/2$) and coil radius ($R_{coil}$ to take into account the effect of tube coiling. If the Nusselt number for straight tubes is required, the coil radius can be set equal to $+\infty$, making both the Dean number and $D_{tube}/(2 \cdot R_{coil})$ equal to zero.

**Laminar flow**

There is a wide variety of authors that have published correlations for the Nusselt number of tubeflow in coiled tubes. Generally there is a good agreement between the different correlations, as can be seen from the selection shown in Figure 3, where those of Kalb and Seadler [1974], Manlapaz and Churchill [1981], and Schmidt [1967] are presented. For this work, the correlation of Manlapaz-Churchill was chosen for the laminar Nusselt number of the coiled and straight tubeflow. Manlapaz and Churchill propose several correlations depending on the boundary conditions that apply to the fluid. To calculate the Nusselt number of the tubeflow in this study, the correlation of Manlapaz and Churchill that is chosen is the one where the radial temperature is assumed to be constant and heating uniform in axial direction, as presented in see Equation 11. These conditions are chosen because the radial temperature gradient through the tube's wall is assumed to be relatively small due to the high thermal conductivity and thin wall. The uniform heating in axial direction is the most representative option, particularly because the heat exchanger is of the counter-flow type.

$$Nu_{lam} = \left[ \left( 48/11 + \frac{51/11}{\left(1 + 1342/(Pr \cdot He^2)\right)^2} \right)^3 + 1.816 \cdot \left( \frac{He}{1 + 1.15/Pr} \right)^{3/2} \right]^{1/3} \tag{11}$$

where

$$He = \frac{De}{\left[ 1 + \left( pitch \cdot \frac{\pi}{2} \cdot \frac{D_{tube}}{2} \right)^2 \right]^{0.5}}$$

**Turbulent flow**

Correlations for turbulent tube flow that are often referenced are those of Dittus and Boelter [1930] (as introduced by McAdams [1942]), Sieder and Tate [1936], and Gnielinski [1976] which have been modified and improved upon for specific cases throughout the years. Shah and Sekulic [2003] (Chapter 7) provides a useful list of several correlations that can be used to model turbulent flow through tubes based on the Fanning friction factor, which in this case is calculated using Equation 10, such as for example those of Rogers and Mayhew [1964], and Petukhov and Popov [1963], which are shown in Figure 3. Similarly to the Nusselt number correlations considered for the laminar flow through coiled tubes, the models show a very good agreement and deviate only a few percent at most. Petukhov's elaborate study showed that his results deviate on average with roughly 10% from experimental results. The correlation of Petukhov-Popov is chosen for the model of the heat exchanger in this work, and is shown in Equation 12. This correlation uses the turbulent flow Fanning friction factor ($f_{turb}$) calculated using Ito's method, as described in subsection 3.2. It is applicable in the following range of Reynolds numbers: $4 \cdot 10^3 < Re < 5 \cdot 10^6$ and the following Prandtl number range: $0.5 < Pr < 10^6$.

$$Nu_{turb} = \frac{Re \cdot Pr \cdot f_{turb}/2}{C + 12.7 \cdot (f/2)^{0.5} \cdot \left(Pr^{2/3} - 1\right)} \tag{12}$$

where

$$C = 1.07 + \frac{900}{Re} - \frac{-0.63}{1 + 10 \cdot Pr}$$

Sieder and Tate [1936] proposed a correction that takes into account the change of fluid properties of the flow near the wall, by multiplying the Nusselt number with the ratio of the fluid's average dynamic viscosity and the dynamic viscosity of the fluid at the wall's surface, raised to a power $n$ (see Equation 13). The value of $n$ is either 0.11 in case the fluid is heated and 0.25 when the fluid is cooled. Implementing this correction gives rise to an iterative process as the average dynamic viscosity of the fluid will change after the new bulk fluid temperature is calculated with the updated Nusselt number. In the current study, this correction is not implemented as the radial tempearture gradient within the tubes of the heat exchanger is assumed to be relatively small.

$$Nu_{corrected} = Nu \cdot \left(\frac{\mu_{avg}}{\mu_{wall}}\right)^{n} \tag{13}$$

**Transitional flow**

Due to the challenges of predicting the exact point of flow transition, the modeling of the Nusselt number in transitional flow rather serves as a mean to maintain a continuous function between the laminar and turbulent regime instead of providing an exact solution. Therefore, results where the flow through the heat exchanger experiences flow transition should be evaluated critically. In the current study, the Nusselt number transition from laminar to turbulent will be approximated using a linear gradient between the two, similarly to the method proposed by Taborek [1990]. The point where the laminar flow stops is defined by Equation 8, while the turbulent Nusselt number model is used from Reynolds larger than $5 \cdot 10^6$. The equation for the linear transition for transitional flow is presented in Equation 14.

$$Nu_{trans} = \left(1 - \frac{Re - Re_{cr,coiled}}{5 \cdot 10^6 - Re_{cr,coiled}}\right) \cdot Nu_{lam} + \frac{Re - Re_{cr,coiled}}{5 \cdot 10^6 - Re_{cr,coiled}} \cdot Nu_{turb} \tag{14}$$

# 4. Tube banks flow correlations

The shellflow in the heat exchanger flows over the many coiled tube bundles in the heat exchanger and thereby exchanges both heat and momentum with the tubewalls. To model this exchange, correlations for the heat transfer coefficient and pressure drop are presented in this section. There are however many parameters to consider when modeling the flow over tube banks, such as the tube pitches, coiling angle, tube distribution, and more. These parameters and the conditions that are applicable to the current study are discussed in subsection 4.1. Thereafter, the different correlations for the heat transfer and pressure drop over tube banks are presented in subsection 4.3 and subsection 4.4.

## 4.1. Overview of flow over tube banks

The coil-wound heat exchanger that is described in this study features a set of tube banks with specific geometrical features. Finding semi-empirical correlations that match all of the geometrical features of a coil-wound heat exchanger is challenging, for which it was found necessary to make

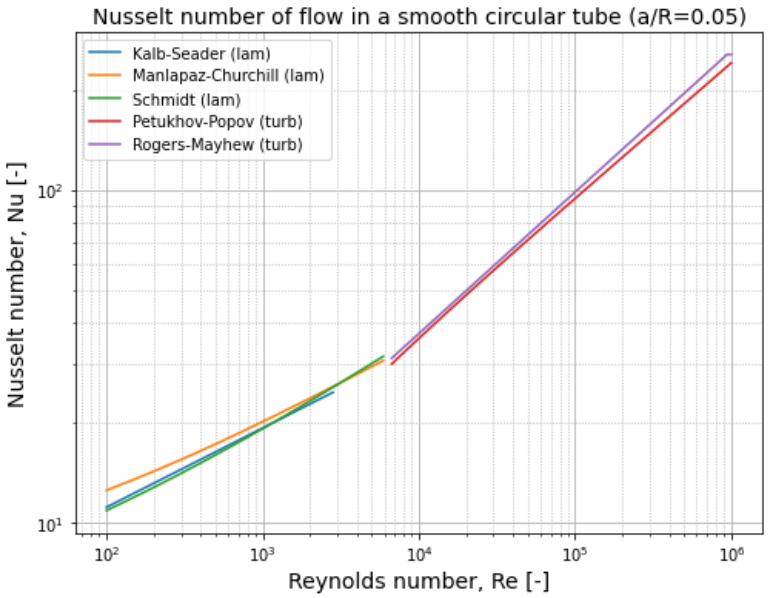


Figure 3: Comparison of laminar and turbulent coiled tube flow correlations for the Nusselt number (for a ratio of minor over major coil diameter of 0.05 and Prandtl number of 0.7).

compromises and assumptions to find the most representative correlations possible. This negatively affects the error range of the heat transfer and pressure drop of the modeled shell flow in the heat exchanger. First, the geometrical parameters that are applicable to the heat exchanger in this study are highlighted below, and visually represented in Figure 4.

**Tube coil angle**

The tubes of this study's heat exchanger are all coiled with the same coil angle, defined as being $0^o$ for parallel tubes and $90^o$ for cross-flow. Due to the limited amount of studies on the effect of the tube coil angle of spirally wound heat exchangers, it is instead insightful to look at the effect of angling straight tubes with respect to the flow direction, also called 'yawed tube banks' or 'inclined tube banks', for which there is more literature available.

**Tube relative inclination**

When considering coiled or yawed tube banks, there are two possible ways these can be oriented relative to each other. As the name suggests, parallel-inclined tubes are all parallel to each other, while for cross-inclined tube banks, each tube layer coils in the opposite direction (or yaws in the opposite direction in the case of straight tube banks). The difference between cross- and parallel inclined tube banks is primarily manifested in the flow path and velocity, which can strongly affect the momentum and heat exchange between the tube walls and the surrounding flow. Typically coil-wound heat exchangers feature a cross-inclined tube inclination to enhance fluid mixing and increase the flow's heat exchange with the tubes. Therefore the tube inclination of the heat exchanger in this study is also taken to be cross-inclined.

**Tube arrangement**

Tube banks are generally arranged either in a staggered or in an in-line configuration. For the in-line configuration, the tubes are placed in a rectangle-shaped pattern where each tube is located

directly downstream of the previous, while in the staggered configuration, the tubes are placed in a rectangular pattern instead. In the case of a coil-wound heat exchanger, the most applicable configuration is that of the in-line configuration.

**Tube spacing**

Two non-dimentional tube spacing variables are often used in literature to describe the tube lay-out: the transverse tube spacing ($S_T$) and longitudinal tube spacing ($S_L$). These denote the distance between the tube centers in transverse (or radial in this case) or longitudinal (or axial in this case) direction, normalized by the tube diameter. As mentioned earlier, for this study, both values are taken to be equal to each other. Typical values in literature range from 1.2 to 2, although the effect of larger or smaller values have also been studied. The majority of the data available in literature is available for tube spacing values of 1.5, while there is very literature available on the effect of the tube spacing on the Nusselt number and pressure drop in cross-inclined, coiled tube bundles. Therefore, for this study, both the transverse and longitudinal tube spacing are both fixed to be 1.5. Deviations from this value could however prove to be interesting for the design of coil-wound heat exchangers, provided that there is sufficient literature available on this effect.

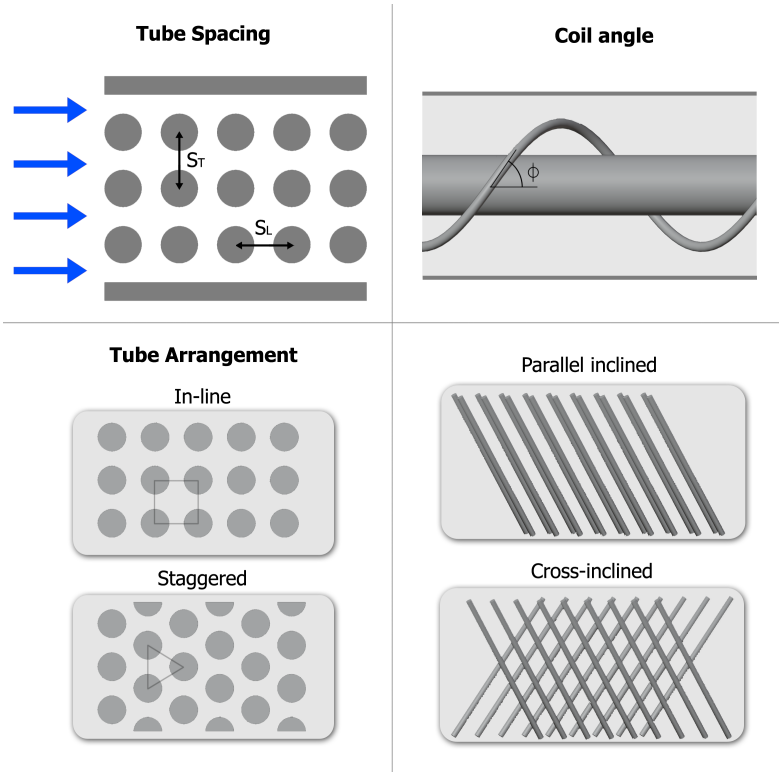


Figure 4: Visual representation of the different geometrical parameters associated with coil-wound heat exchangers.

Correlations for flow over tube banks typically define their Reynolds number by using the outer diameter of the tubes as a reference length. Additionally, the reference velocity is that at the most narrow crossection between the tubes and not the average flow velocity through the tube bank.

## 4.2. Groehn's work

One specific paper has been of great value when collecting representative correlations for the flow over the coiled tube bundles of the heat exchanger: the work done by Groehn [1990]. Groehn performed a series of experimental tests on both cross-inclined and parallel-inclined tube bundles at various yaw angles and tube spacings for a wide range of Reynolds numbers. Additionally, he also performed several comparisons between coiled and straight tubes with similar geometrical parameters to characterise the similarity between the two. It was concluded that for both the flow of gaseous air and helium, the effect of coiling is minimal on the shell-side flow compared to straight tubes. This finding makes it possible to expand the literature scope from coiled, cross-inclined, 1.5 pitched tube banks to straight, cross-inclined, 1.5 pitched tube banks, for which there is more literature available.

In his paper, Groehn doesn't propose any correlations to calculate the Nusselt number or pressure drop coefficient, however he presents his processed experimental data in a multitude of graphs, plotting either $Nu/Pr^{0.36}$ or the pressure drop coefficient $\xi$ in function of the Reynolds number. Therefore in the present study, Groehn's data was digitized and used to draw new correlations from. These empirical correlations are then used in comparison with existing literature to increase the author's confidence towards the validity of the assumptions and simplifications that were made when using correlations from other literature sources. His work, in combination of that of Žukauskas forms the backbone of the heat transfer and pressure drop correlations used within this study.

## 4.3. Nusselt number of flow over tube banks

With his experiments, Groehn's data shows that there is almost no difference between the Nusselt number of flow over tube banks at 30, 45, 60, 75, and 90 degrees at all tested Reynolds number, for both parallel- and cross-inclined tubes. Although this seems to imply that the Nusselt number is independent from the coil angle, it should be pointed out that the Reynolds number used by Groehn is defined by the flow velocity component perpendicular to the tubes and thereby indirectly introduces a dependence on the coil angle, proportional to $sin(\phi)$. Additionally, when overlaying the Nusselt data from Groehn for different tube spacings (see Figure 5), it is apparent that the Nusselt number is also independent from the tube spacing in the range of $1.25 < S_L = S_T < 2.0$. From his data, Equation 15 was deducted by fitting a power-law function using least squares regression. Note that the Reynolds number used in Equation 15 uses the more common definition of the Reynold's number for tube banks, as defined in Equation 16, instead of the one Groehn uses.

$$Nu_{Groehn} = 0.4005 \cdot Pr^{0.36} \cdot \left[Re \cdot sin(\phi)\right]^{0.5793} \tag{15}$$

$$Re_{tubebank} = \frac{\rho \cdot D_{tube} \cdot V_{max}}{\mu} \tag{16}$$

This correlation is compared to that of other authors in literature to assess their applicability and at the same time also validate the correctness of the newly generated Equation 15. Several authors that provide correlations for the heat transfer of flow over yawed tube banks are Žukauskas [1972], Abadzic [1974], Kim [2013], and Le Feuvre [1986]. The work of Žukauskas provides a particularly detailed explanation of the different flow phenomena of flow over tube banks at different tube spacings for in-line, staggered and individual tubes in cross-flow. In this work, Žukauskas [1972] combines the results and correlations from various different publications for in-line tube banks to propose a generalized equation, being Equation 17. This equation applies to a very wide range of Reynolds numbers, being $10 < Re < 2 \cdot 10^6$. Additionally, a correction factor ($C_\phi$) is suggested to take

into account the effect of the tube bank's yaw angle ($\phi$), albeit for parallel inclined tubes and not cross-inclined tubes. The value of $C_\phi$ was digitized from a graph presented in the work of Žukauskas [1972], by fitting a polynomial least squares regression, resulting in Equation 18 with an $r^2$ error of 0.99995 (for $20^o < \phi < 90^o$).

$$Nu_{Žukauskas} = \begin{cases} 0.27 \cdot Re^{0.63} \cdot Pr^{0.36} \cdot C_\phi & \text{for } Re < 2 \cdot 10^5 \\ 0.021 \cdot Re^{0.84} \cdot Pr^{0.36} \cdot C_\phi & \text{for } 2 \cdot 10^5 < Re < 2 \cdot 10^6 \end{cases} \tag{17}$$

$$C_\phi = \text{minimum} \begin{cases} 1 \\ 0.1327 + 1.3028 \cdot \phi - 0.5649 \cdot \phi^2 + 0.0551 \cdot \phi^3 \end{cases} \tag{18}$$

Several authors have performed computational fluid dynamics (CFD) analyses on the flow over such tube banks to study the effect of specific geometrical parameters. For example, Kim [2013] used CFD to come up with a modified version of Žukauskas [1972] correlation to account for the value of the lateral tube spacing ($S_L$). His correlation is also presented in Figure 5, however not used in the present study as it showed a worse agreement with the experimental data of Groehn and other correlations, as compared to the original correlation of Žukauskas. Another computational study that proved relevant is that of Wang et al. [2016], where they compared the effect of the tube yaw angle of their numerical results with that of Žukauskas [1972], showing an error margin ranging from 15% to 30% for the Nusselt number.

It should be noted that in the current study, the equation of Abadzic [1974] (Equation 20) was modified by multiplication with the coiling correction factor from Žukauskas to account for the tube coiling.

$$\frac{Nu_{Kim}}{Nu_{Žukauskas}} = 1 - 2.26 \cdot e^{-1.675 \cdot S_L} \tag{19}$$

$$Nu_{Abadzic} = \begin{cases} 0.294 \cdot Re^{0.6} \cdot Pr^{0.36} \cdot C_\phi & \text{for } 1000 < Re < 2 \cdot 10^4 \\ 0.109 \cdot Re^{0.7} \cdot Pr^{0.36} \cdot C_\phi & \text{for } 2 \cdot 10^4 < Re < 2 \cdot 10^5 \end{cases} \tag{20}$$

Additionally, Le Feuvre [1986] combined the experimental work of several authors for straight cross-inclined tubes and of helically coiled ones, resulting in Equation 21, which already takes into account the coil angle. Le Feuvre's correlation has a narrower range of applicability, being $2 \cdot 10^4 < Re < 2 \cdot 10^5$

$$Nu_{LeFeuvre} = 0.109 \cdot Pr^{0.36} \cdot (cos(\pi - \phi))^{-0.7} \cdot Re^{0.7} \tag{21}$$

A comparison of the different correlations is shown in Figure 5. There is a close match between the different correlations, with the correction from Kim [2013] deviating most from the others. In the end the correlation of Žukauskas [1972], Equation 17 was chosen for the present study.

## 4.4. Pressure drop coefficient of flow over tube banks

Finding correlations for the Nusselt number of flow over spirally-wound, cross-inclined, tube banks at tube spacings of 1.5 proved to be possible with a reasonable error range due to the independence of of the Nusselt number to several variables and the good agreement of of the different correlations. However, the data of Groehn [1990] showed that there is a strong dependence of the pressure

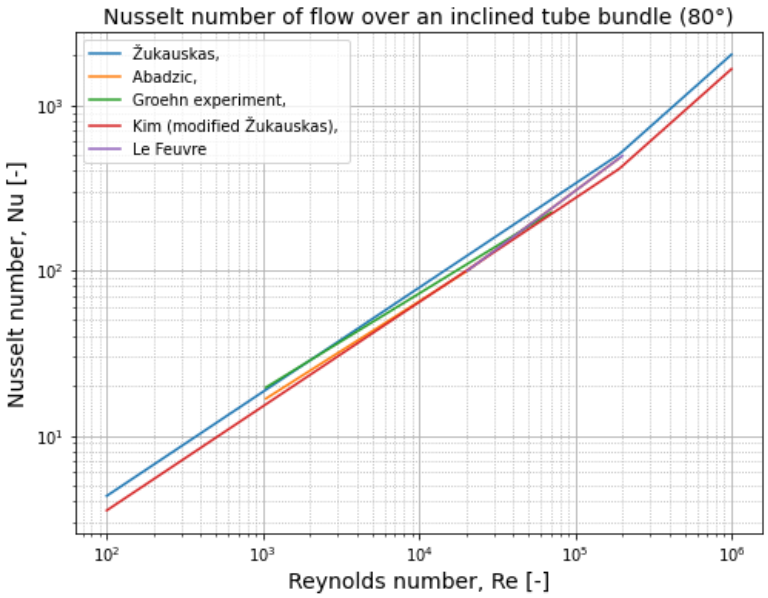


Figure 5: Comparison of flow correlations for the Nusselt number of cross-inclined flow over a coiled tube bank with $S_L = S_T = 1.5$ (for a Prandtl number of 0.7).

drop coefficient ($\xi$) on the tube angle, tube spacing, and also weather the tubes are parallel- or cross-inclined. A correlation (Equation 22) for the pressure drop coefficient of Groehn's data (cross-inclined and $S_L = S_T = 1.5$) was created in the present study to calculate the pressure drop over the coiled tubes, applicable to the range $2000 < Re < 4 \cdot 10^5$ and at coil angles of $45^o$ and larger.

$$\xi_{groehn} = 69034 \cdot (\phi \cdot 180/\pi)^{-2.6777} \cdot Re^{-58.8943 \cdot \phi^{-1.4619}} \tag{22}$$

Žukauskas [1972] presents a correlation to calculate the pressure drop coefficient ($\xi$) for flow over tube banks in a cross-flow orientation ($\phi = 90^o$) at different tube spacings, for both staggered and in-line tube arrangements. Instead of providing an equation, Žukauskas presents several figures where value of $\xi$ can be read from using the ratio $\xi/\chi$ and the intermediate variable $\chi$. These were digitized for the present study in order to compare to the data from Groehn [1990]. The digitized equations for Žukauskas' pressure drop coefficient are presented in Equation 23 and Equation 24, specifically for cross-flow over in-line tube banks at a tube spacing of $S_L = S_T = 1.5$. It should be noted that for Equation 23, the three equations don't form a continuous function, as a gradual transition between the different functions is proposed to prevent abrupt gradient changes of the function. It was found that the error margin between these digitized equations with the graphical correlation of Žukauskas is less than 0.5%.

$$\frac{\xi}{\chi} = \begin{cases} 82.960 \cdot Re^{-1.043} + 0.1574 & \text{for } 30 < Re < 800 \\ 12687.45 \cdot Re^{-2.628} - 12686.81 & \text{for } 4 \cdot 10^3 < Re < 10^5 \\ 0.2314 & \text{for } Re > 3 \cdot 10^6 \end{cases} \tag{23}$$

where

$$\chi = [(S_L - 1) \cdot (S_T - 1)]^{-72945.59 \cdot Re^{-6.271} + 72944.51} \tag{24}$$

Additionally, the work of Le Feuvre [1986] provides an excellent overview of several correlations that can be used to calculate the pressure drop and heat transfer of flow over tube banks in heli-

cally coiled and straight tube banks. From his summary, the correlations where $S_L = S_T = 1.5$ are evaluated and presented in Figure 6, alongside with the suggestion from Le Feuvre self. These correlations makes use of a Fanning flow friction factor ($f$) to calculate the pressure drop over tube banks instead of the pressure drop coefficient as mentioned above.

Figure 6 shows that the aforementioned correlations follow the same trend, however the values of Žukauskas are nearly two times larger. The numerical CFD study from Wang et al. [2016] found that Žukauskas' results for pressure drops across tube bundles with various yaw angles is between 22% and 55% larger than their numerical results. Additionally, Groehn [1990] also mentioned in his paper that the measurements of the pressure drops had to be corrected for the entrance and exit regions of the tube bundle, leading to potentially higher or lower values of the hydraulic resistance coefficient. The correlations from Hua, Dixon, and Le Feuvre do show a reasonably good agreement with the correlations created in this study from the experiments of Groehn with a maximum relative error of 9%, -14%, and -50% respectively. Although still significant, these error margins are of a similar magnitude as what is found in literature, for example such as was concluded by Wang et al. [2016].

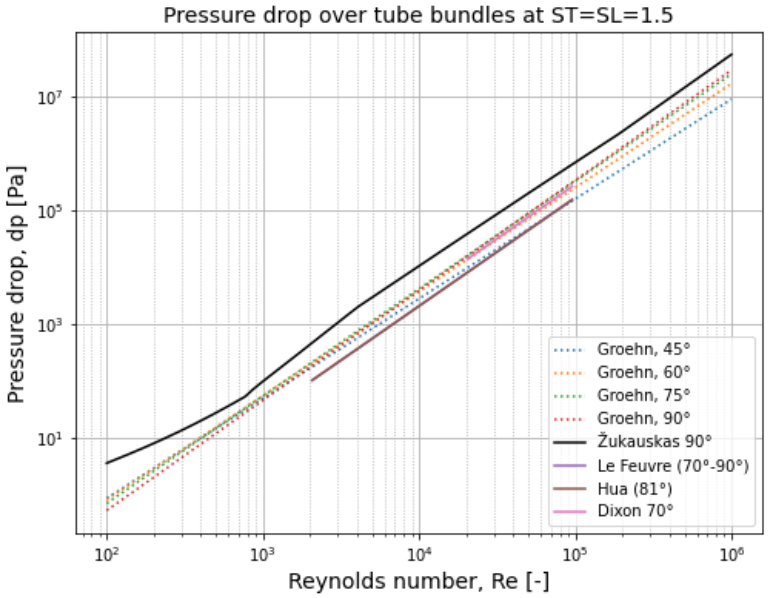


Figure 6: Pressure drop comparison between Žukauskas' correlation and the correlations created from Groehn's data. Note that the reference velocity of the Reynolds number is taken to be that at the narrowest crossection of the tube bundle.

For the present study, the self-deducted correlation (Equation 22) from Groehn's data was used to calculate the pressure drop of the shellflow over the tube bundles, primarily because it allows for the calculation of the pressure drop over inclined tube bundles, while Žukauskas' correlation only applies to crossflow. Pressure drop results on the shell side of the heat exchanger should however be used critically because of the large uncertainties of the correlations, as addressed in this section.

Finally, the pressure drop from the flow over the tube banks can be calculated using Equation 25, where $z$ represents the number of tubes that the flow has to flow over sequentially.

$$\Delta p = z \cdot \xi \cdot 0.5 \cdot \rho \cdot V^2 \tag{25}$$

# 5. Correlations for shellflow near the outer wall

The fluid that flows over the tube bundles also exchanges heat and momentum with the solid walls, other than those of the tubes. Primarily the wall of the outer shell and the wall of the heat exchanger core. The contribution of the fluid interaction with these walls was found to be smaller than that the interaction with the tubewalls.

Due to the limited availability of literature on the fluid behaviour of flow between a spirally wound tube bundle and a cylindrical wall, and due to the lower degree of relevance compared to the outcome of the heat exchanger, a simplified model is used for the heat transfer and pressure drop correlations. The flow near the cylindrical walls of the heat exchanger can be approximated as annular flow. Due to the narrow tube spacing of the heat exchanger, the gap between the tubes and the cylindrical walls is multiple orders magnitude smaller than the radius of heat exchanger. Therefore, the annular flow can be represented with the flow between two infinitely long parallel plates. The heat and momentum exchange near outer shell wall and the core wall is modeled as if the fluid flows between two flat plates or through an annulus respectively. The correlations of this flow are presented in subsection 5.1 and subsection 5.2.

## 5.1. Nusselt number of flow in narrow passages

The heat transfer from the cylindrical shell wall to the fluid in the shell near this wall is modeled as a fluid that flows in between two parallel plates. The distance of the narrow passage between the tube bundle and the shell wall is relatively small compared to the shell wall diameter. Therefore the assumption of the flow between two infinite flat plates can be used.

**Laminar flow**

For the laminar flow regime of the shellflow near the cylindrical walls, the work of Spiga and Morini [1996] was used. They suggest several constant value Nusselt numbers for the laminar flow in a rectangular duct with an infinite aspect ratio, for various thermal boundary conditions. The most representative case for the present study is where only one of the walls introduces heat, while the others are adiabatic. In this case Spiga and Morini [1996] propose a value of 140/26 for the laminar Nusselt number.

**Turbulent flow**

A correlation for the Nusselt number in case of turbulent flow, as function of the Reynolds number is provided by Shibani and Özişik [1976], as shown in Equation 26, which is applicable for the range $Re_{cr} < Re < 10^6$, with an error margin of 6% as stated by Shibani and Özişik.

$$Nu_{turb} = \begin{cases} 12 + 0.03 \cdot Re^{0.88-0.24/(3.6+Pr)} \cdot Pr^{0.33+0.5 \cdot e^{-0.6 \cdot Pr}} & \text{for} \\ 8.3 + 0.02 \cdot Re^{0.82} \cdot Pr^{0.52+0.0096/(0.02+Pr)} \end{cases} \tag{26}$$

**Transitional flow**

The model for transitional flow for the fluid in between the tubes and the cylindrical wall is constructed in a similar manner as that of the tube flow, explained in subsection 2.1. A gradual transition from the laminar to the turbulent Nusselt number is used to provide a continuous function between these regimes. The laminar regime stops at the critical Reynolds number, here being

defined as 2100, while the turbulent regime is taken to start where the correlation of Shibani and Özişik [1976] is valid, being at $Re = 10^4$. As stated before, the solution from the transitional flow regime should not be regarded as an exact solution.

## 5.2. Pressure drop coefficient of flow in narrow passages

The pressure drop caused by friction between the shellflow and the cylindrical walls of the heat exchanger is modeled as if it were an annulus. The flow through an annulus can be modelled by flow through a tube where the hydraulic diameter is replaced by twice the width of the gap of the annulus. Therefore, equations for the Fanning friction factor similar to those described in section 3 are proposed for the flow near the shell walls.

**Laminar flow**

For the laminar flow, Hagen-Poiseulle's correlation (Equation 4) is used until the critical Reynolds number of 2100 is reached.

**Turbulent flow**

In the turbulent flow regime, the well-known correlation of Blasius [1913] is used to calculate the turbulent Fanning friction factor, as shown in Equation 27.

$$f_{turb} = \begin{cases} \frac{0.316}{Re^{0.25}} & \text{for } 3000 < Re < 2 \cdot 10^4 \\ \frac{0.184}{Re^{0.2}} & \text{for } 2 \cdot 10^4 < Re < 2 \cdot 10^6 \end{cases} \tag{27}$$

**Transitional flow**

Similarly to the previously explained models, the transitional regime is modelled by using a linear gradient between the laminar and turbulent equations, and thereby creating a fully continuous function.

# References


E. E. Abadzic. Heat transfer on coiled tubular matrix. ASME winter annual meeting, 1974.

M. S. Bhatti and R. K. Shah. Laminar convective heat transfer in ducts. Handbook of Single-Phase Convective Heat Transfer, Chapter 3, 1987.

P. R. H. Blasius. Das aehnlichkeitsgesetz bei reibungsvorgangen in flussigkeiten. Forschungsheft, 131:pp. 1–41, 1913.

W. R. Dean. Note on the motion of fluid in a curved pipe. Philosophical Magazine, Vol. 20:pp. 208–223, 1927.

W. R. Dean. The streamline motion of fluid in a curved pipe. Philosophical Magazine, Vol. 30:pp. 673–693, 1928.

F. W. Dittus and L. M. K. Boelter. Heat transfer in automobile radiators of the tubular type. University of California Publications in Engineering, Vol. 2:pp. 443–461, 1930.

V. Gnielinski. New equations for heat and mass transfer in turbulent pipe and channel flow. Int. Chem. Eng., pages pp. 359–168, 1976.

H. G. Groehn. Increase of heat exchanger efficiency for yawed tube banks. Nineth International Heat Transfer Conference, Vol. 5:pp. 73–78, 1990.

H. Ito. Friction factors for turbulent flow in curved pipes. Journal of Basic Engineering, pages pp. 123–134, 1959.

C. E. Kalb and J. D. Seadler. Fully developed viscous-flow heat transfer in curved circular tubes with uniform wall temperature. American Institute of Chemical Engineers Journals, Vol. 20:pp. 340, 1974.

T. Kim. Effect of longitudinal pitch on convective heat transfer in crossflow over in-line tube banks. Annals of Nuclear Engineering, Vol. 57:pp. 209–215, 2013.

R. F. Le Feuvre. A method of modeling the heat transfer and flow resistance characteristics of multi-start helically-coiled tube heat exchangers. Eighth International Heat Transfer Conference, Vol. 6: pp. 1–41, 1986.

M. L. Manlapaz and S. W. Churchill. Fully developed laminar flow from a helical coil. Chemical Engineering Communications, Vol. 9:pp. 185–200, 1981.

W. H. McAdams. Heat transmission, 2nd edition. McGraw-Hill, New York, 1942.

P. Mishra and S. N. Gupta. Momentum transfer in curved pipes. i. newtonian fluids, ii. non-newtonian fluids. Industrial and Engineering Chemistry Process Design and Development, Vol. 18:pp. 130–142, 1979.

B. S. Petukhov and V. N. Popov. Theoretical calculation of heat exchange in turbulent flow in tubes of an incompressible fluid with variable physical properties. High Temp., Vol. 1(No.1):pp. 69–83, 1963.

G. F. C. Rogers and Y. R. Mayhew. Heat transfer and pressure loss in helically coiled tubes with turbulent flow. International Journal for Mass and Heat transfer, Vol. 7:pp. 1207–1216, 1964.

E. F. Schmidt. Heat transfer and pressure loss in coiled tubes. Chem. Eng. Tech., Vol. 39:pp. 781–789, 1967.

R. K. Shah and D. P. Sekulic. Fundamentals of heat exchanger design. John Wiley & Sons Inc, Hoboken (USA), 2003. ISBN 0-471-32171-0.

S. N. Shah and Y. Zhou. Fluid flow in coiled tubing: a literature review and experimental investigation. Journal of Canadian Petroleum Technology, Vol. 43(No.6):pp. 52–61, 2004. doi: 10.2118/04-06-03.

A. A. Shibani and M. N. Özişik. A solution to heat transfer in turbulent flow between parallel plates. International Journal of Heat and Mass transfer, Vol. 20:pp. 565–573, 1976.

E. N. Sieder and G. E. Tate. Heat transfer and pressure drop of liquids in tubes. Ind. Eng. Chem., Vol. 28(No.12):pp. 1429–1435, 1936.

M. Spiga and G. L. Morini. Laminar heat transfer between parallel plates as the limiting solution for the rectangular duct. International Communications on Heat and Mass transfer, Vol. 23(4):pp. 555–562, 1996.

P. S. Srinivasan, S. S. Nandapurkar, and F. A. Holland. Friction factors for coils. Transactions of the Institution of Chemical Engineers, Vol. 48:pp. 156–161, 1970.

J. Taborek. Design method for tube-side laminar and transition flow regime with effects of natural convection. 9th International Heat Transfer Conference, Jerusalem (Israel), 1990.

Y. Wang, Xin Gu, Z. Jin, and K. Wang. Characteristics of heat transfer for tube banks in crossflow and its relation with that in shell-and-tube heat exchangers. International Journal of Heat and Mass transfer, Vol. 93:pp. 584–594, 2016.

A. Žukauskas. Heat transfer from tubes in crossflow. Advances in heat transfer, Vol. 8:pp. 93–160, 1972. doi: 10.1016/s0065-2717(08)70038-8.

# Appendix D

# Tubular heat exchanger model for distributed cooling of a liquid hydrogen tank

## – Model description and validation –

By Thomas Britting,

Supervised by C. De Servi and F. Beltrame

In partial fulfillment of the MSc thesis

# 1. Introduction

One of the three heat exchangers in a reverse turbo-Brayton cryocooler (RTBC) is the one that extracts the heat load from the to-be-cooled object, which in this case is the liquid hydrogen inside the fuel tank.

There exist several type of heat exchangers that are used to cool or heat up liquids inside closed volumes, often used in boilers. Most of these are comprised of tubes, often with features that improve heat transfer such as fins and corrugations. An often used geometry for submerged tubular heat exchangers is that of a single coiled tube, which provides a large surface area for limited dimensions.

One of the prime challenges of cooling a large volume of cryogenic fluids, is the low thermal conductivity of the fluid, which decreases the thermal diffusion and causes temperature stratification within the tank. This becomes particularly challenging for larger tanks. In such cases it becomes advantageous to have a heat exchanger that is well distributed throughout the tank. An example of a heat exchanger that was designed to evenly distribute the heat transfer throughout a large liquid hydrogen tank is that of NASA's Ground Operations Demonstration Unit (GODU). In a paper by Fesmire et al. [2014], the design and analysis of a tubular heat exchanger is described for the refrigeration of a 125000 liter liquid hydrogen tank. This heat exchanger design is used as a baseline for the present study because of its similarity to the studied conditions, namely the refrigeration of a large liquid hydrogen tank. A more detailed description of the test set-up and design of this heat exchanger is provided in subsection 4.1.

This appendix aims to provide a more detailed overview of the model that was developed during this study to calculate performance of a specific heat exchanger (rating) or to estimate the mass and size of a given heat exchanger for a given thermal load (sizing). A general description of this heat exchanger's geometry can be found in section 2, alongside the model's general structure, inputs, outputs and assumptions. section 3 goes in more detail, outlining the governing equations of the model, as well as the fluid correlations that were used. Thereafter, section 4 explains the efforts undertaken to validate the model against NASA's GODU heat exchanger mentioned in the previous paragraph. Finally, the conclusion of the development of this tubular heat exchanger model for liquid hydrogen tank refrigeration can be found in section 5.

# 2. Tank heat exchanger model overview

**Geometry description**

The heat exchanger design of this chapter is based on that of NASA's GODU liquid hydrogen tank, as described by Fesmire et al. [2014]. They identified a hoop and barrel configuration heat exchanger (also called a whale-skeleton heat exchanger) to offer the most ideal combination of pressure drop, cooling distribution, and heat transfer. It is comprised of two horizontal tubes (also called manifolds), of which the bottom one distributes the cooling fluid among a series of smaller tube pairs. These smaller tubes follow the outer contour of the tank and allow the cooling fluid to flow from the lower manifold to the upper manifold and thereby provide a distributed cooling load along the full length and width of the tank. The cooling fluid enters the heat exchanger in the lower horizontal tube and leaves the heat exchanger from the upper horizontal tube. This configuration is best suited for applications where the heat exchanger fulfils a cooling function, as the warmer fluid in the tank tends to rise in the buoyancy-driven convective currents. A visual representation of how the cooling fluid flows through the tank heat exchanger, can be seen in Figure 3, alongside with a

three-dimensional view of the heat exchanger in Figure 1. A visual overview of a single tube pair can be seen in Figure 2, along with the equations that are used to calculate the total tube length $L_{tube}$.

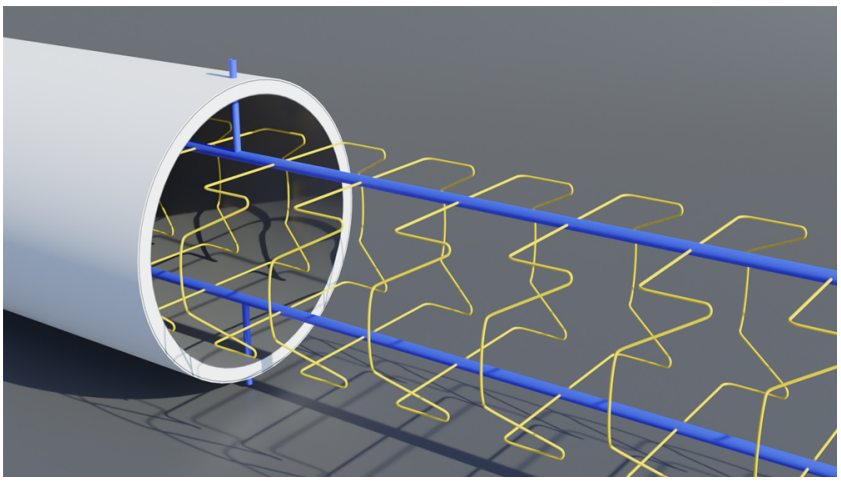

Figure 1: Render of the tank heat exchanger inside a cylindrical tank, similar to that described by Fesmire et al. [2014]. The two horizontal distributors (distributor and collector) are shown in blue, while the smaller distributed tubes are shown in yellow.

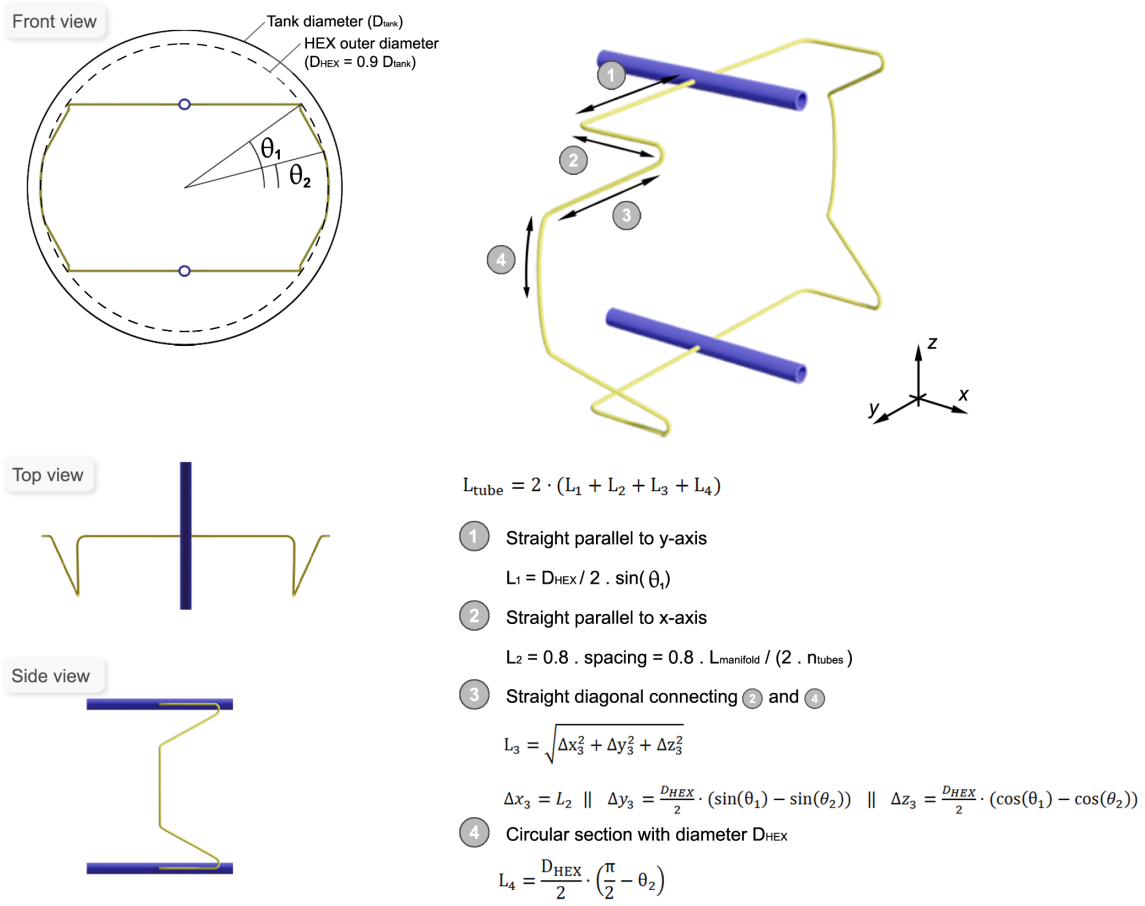


Figure 2: Overview of a single tube pair's geometry, including the equations used to calculate the tube lenth $L_{tube}$.

Typically in such a heat exchanger, the mass flow rate through each tube pair will be different as the pressure of the flow through the manifolds decreases towards the ends. This flow maldistribution was countered in NASA's GODU heat exchanger design by the installation of tailored orifices that equalize the pressure drop and mass flow among the various tube pairs to within 1%. [Fesmire et al., 2014] instead of 14% in case of no orifices.

The heat exchanger geometry of this model is symmetrical along all three primary axes, where the inlet and outlet tubes are located at the mid-point of the two manifolds. This simplifies the model as the solution to only one quadrant of the heat exchanger can be modeled.

**Model structure**

Due to the proximity to the critical point and the variable fluid properties of helium at temperatures below 20 Kelvin, a distributed parameter approach has been chosen for the HEX model, similar to that of the RTBC recuperator in this study. Therefore, the different components of the heat exchanger are segmented and for each of these segments the fluid properties are evaluated in order to locally solve a set of conservation equations.

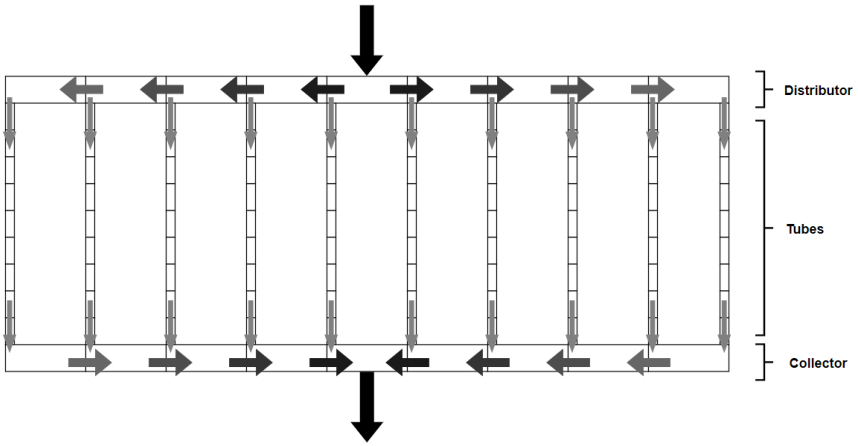


Figure 3: Overview of the flow paths inside the tank heat exchanger, where darker arrows represent a higher mass flow rate that lighter arrows.

**Assumptions**

- The fluid inside the tank is assumed to have uniform fluid properties and temperature.
- The simulation is assumed to be at a steady state with no changes over time.
- The coolant (Helium) fluid properties are assumed to be constant within each control volume. This was proven to be valid following the grid sensitivity results that is presented in subsection 4.3.
- The number of tubes is restricted to an even number to maintain lateral symmetry over the tank's primary axis.
- Each of the tubes is assumed to experience the same mass flow rate due to the use of correcting orifices. For NASA's GODU heat exchanger, this proved to equalize the flow rate to within 1%.

- The pressure drop effects of flow mixing and tube kinks are neglected and instead pressure drop is only calculated to originate from frictional forces with the tube walls.
- The model assumes perfect local mixing of the fluid within the heat exchanger, thereby neglecting any radial temperature gradients within the heat exchanger tubes. Additionally, the mixing of two merging fluid streams is assumed to be instantaneous and loss-less.
- The flow is assumed to be fully developed, where any entrance effects are neglected. The initial assumption was based on the criteria that the tube length should be at least 10 times the tube inner diameter, however a more detailed check of this assumption's validity was performed later and proved still to be valid.
- Fluid properties are modelled to be variable with both temperature and pressure through use of the CoolProp program [Bell et al., 2014], which makes use of the Helmholtz energy equations to solve for the fluid properties.
- The fluid properties of hydrogen are assumed to be those of the instantaneous equilibrium between the ortho- and para-hydrogen isomers at a given temperature and pressure.
- Natural convection of the fluid inside the tank is assumed to be driven purely by a constant gravitational acceleration of $9.80665 m/s^2$, neglecting any other accelerating forces acting on the tank or fluid.
- Thermal radiation is neglected in the model as the radiative heat flux of objects near 20 Kelvin and below is many orders of magnitude smaller compared to the convective heat transfer. For reference, even at 100% emissivity, an object at 20 Kelvin has a black body emissive heat flux less than $0.01 W/m^2$, which is four orders magnitude smaller than the heat flux values experienced by NASA's GODU heat exchanger. [Fesmire et al., 2014]
- Effects of axial conduction through the tube walls are assumed to be negligible as the temperature gradient throughout the heat exchanger is only in the order of several Kelvin (generally less than 10 K) for a length of multiple meters, with a steel thermal conductivity below $2 W/(m \cdot K)$. For example in case of the NASA GODU heat exchanger, the thermal conductivity through the tube walls was found to be in the order of several milliwatts, being 5 orders magnitude smaller than the convective heat transfer.
- Gravitational effects on the cooling fluid are neglected, including natural convection of the cooling fluid or gravity-induced vertical pressure gradients. A typical measure to determine if a heat transfer is primarily forced or natural convection is Richardson's number ($Ri$), being defined as $Ri = Gr/Re^2$. The study by Sparrow et al. [1959] concluded that below a Richardson number of 0.3, the assumption of neglecting natural convection has an error of less than 5%. The Richardson numbers encountered in this study have been significantly lower, such as for example the maximum value of $Ri = 0.0074$ encountered during validation (see section 4).

**Model inputs and outputs**

The tank heat exchanger program can be used in two different ways: as a rating problem where the number of tube pairs is provided as an input, for which the heat transfer is an output. And secondly as a sizing problem, where the number of tube pairs is varied to achieve a heat transfer as close as possible to a target value.

The primary outputs of the model are the pressure drop, HEX mass, actual heat transfer between the tank fluid and the coolant, and coolant outlet temperature. A complete overview of the inlets and outputs of the program can be found on page 21 of this appendix.

# 3. Tank heat exchanger model description

The heat exchanger is divided in three separate components: the upper horizontal manifold (also called the collector), the lower horizontal manifold (also called the distributor), and lastly the many pairs of smaller tubes. As mentioned in the assumptions, only one quarter of the heat exchanger is modelled as the geometry and coolant flow is symmetrical. Each of these three components is subdivided into multiple control volumes (segments) for which the governing equations are solved. An overview of the tank heat exchanger program can be seen in the flow diagram in Figure 4, which will be discussed in more detail below.

The number of tubes, heat load, inlet conditions, and effectiveness of the tank HEX are used as an input to size the diameter of the tubs and thereby estimate the tank HEX's mass. The effectiveness is defined by the heat transfer from the hydrogen to the helium cooling fluid divided by the maximum possible heat transfer between the two. The latter can be expressed as the enthalpy difference of the cooling fluid assuming it reaches the same temperature as the liquid hydrogen without pressure loss, as shown in Equation 1.

$$\dot{Q}_{max} = H_{out,max} - H_{in} = \dot{m} \cdot (h_{out,max} - h_{in}) \tag{1}$$

Thereby the required mass flow rate of the cooling fluid is calculated using the effectiveness in combination with the imposed heat load ($\dot{Q}$) and effectiveness $\epsilon$, as shown in Equation 2.

$$\dot{m} = \frac{\epsilon \cdot \dot{Q}}{\dot{Q}_{max}} \tag{2}$$

The rating problem will calculate the heat transfer for the given geometry and input conditions. Thereafter, the effectiveness for the current Reynolds number is compared with the target effectiveness in order to change Re using a Nelder-Mead optimization. The change in Reynolds number translates to a change in the tube diameter, as the mass flow through the HEX is predetermined. With this newly updated geometry, the rating problem is executed again. This process continues repeatedly until the geometry is found that provides the closest match to the target effectiveness.

The current model is however restricted to a specific range of Reynolds numbers for which the internal and external convective heat transfer correlations are valid. When these bounds are exceeded by the Reynolds number for the internal convection or Rayleigh number for the external convection, the target effectiveness of the tank HEX is reduced. This process is repeated until a design is found that satisfies the operational range of the heat transfer correlations.

Furthermore, the tank HEX model imposes a maximum pressure drop constraint. If the pressure drop of the flow through the tank HEX exceeds an imposed tolerance, each of the tube's length is reduced. More specifically, the length of segment 2 shown in Figure 2. If the length of segment 2 is reduced to zero, the tank HEX sizing tool will terminate with an error statement.

**Tank heat exchanger rating**

The tank heat exchanger rating program is shown separately in Figure 4. It first calculates the required geometry in the heat exchanger, such as the length of each tube, flow areas and tube inner and outer diameters. From this geometry, then a one-dimensional mesh is generated that contains data of the different segments. Then the fluid properties of the liquid inside the tank are calculated: fluid density ($\rho_{tank}$), dynamic viscosity ($\mu_{tank}$), Prandtl number ($Pr_{tank}$), and isobaric thermal expansion coefficient ($\beta_{tank}$).

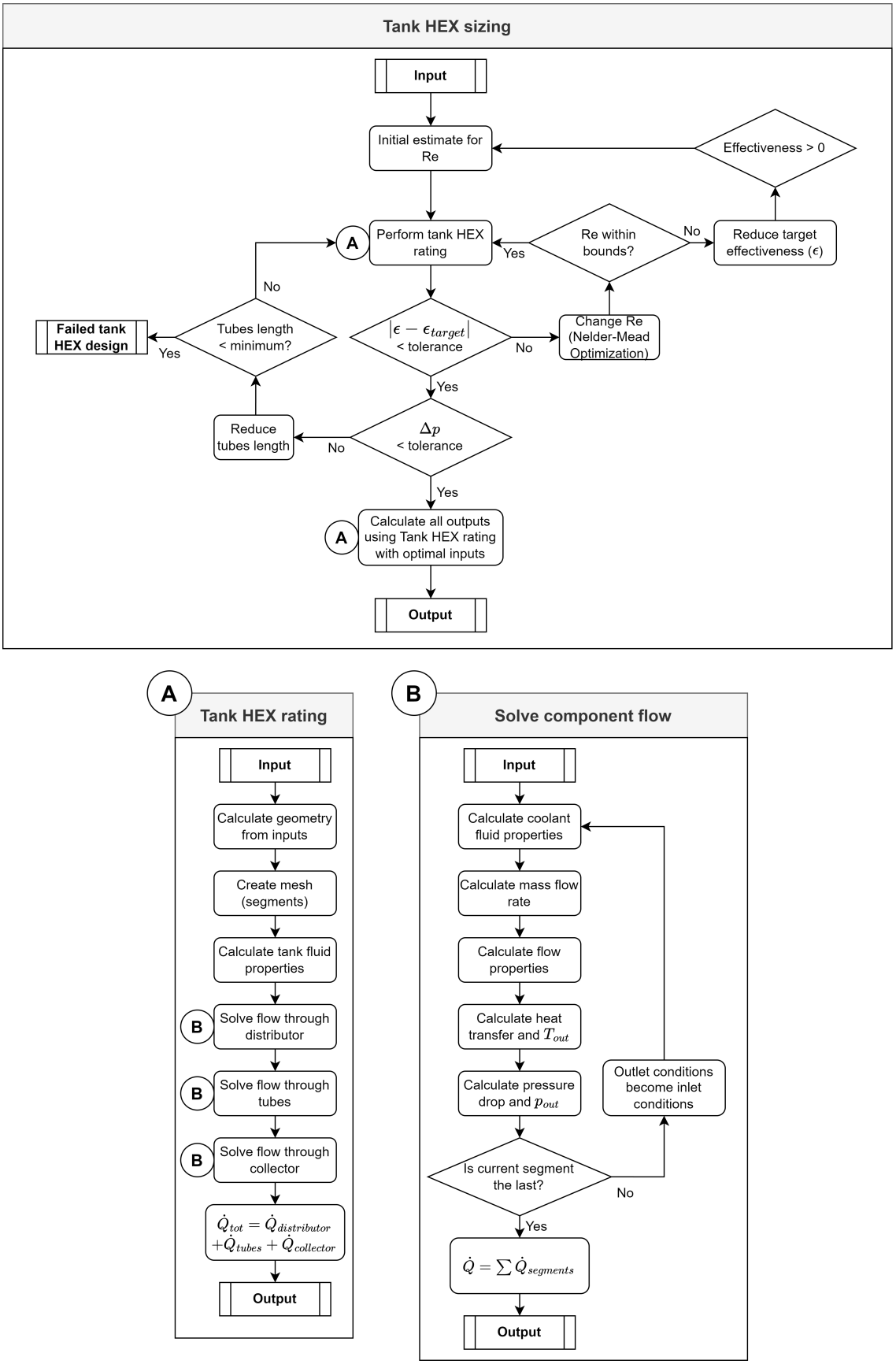


Figure 4: Flow diagram for the tank heat exchanger program.

Thereafter, the rating program will sequentially calculate the heat transfer of the distributor, tubes, and collector by progressively solving a system of equations for each segment. The equations that are used to solve for the fluid behaviour through each of the components of the heat exchanger (flow diagram B in Figure 4) are explained in subsection 3.1. Afterwards, the heat transfer of the whole heat exchanger is calculated by simply adding that of the distributor, tubes, and collector, as shown in Equation 3.

$$\dot{Q}_{tot} = \dot{Q}_{distributor} + \dot{Q}_{tubes} + \dot{Q}_{collector} \tag{3}$$

## 3.1. System of equations

**Mass conservation**

As stated in the assumptions, the mass flow rate through all the smaller tubes ($\dot{m}_{tube}$) is assumed to be the same, and equal to the heat exchanger's total mass flow rate divided by the number of tubes.

The mass flow rate through the first cell of the distributor is set equal to that of half the heat exchanger, as the cooling fluid is split equally between each halves of the heat exchanger. At each segment boundary, the mass flow rate is reduced by twice $\dot{m}_{tube}$, to account for the fluid entering a tube pair at each cell's boundary. Figure 3 shows the mass flow distribution through the whole heat exchanger, while Figure 5 shows how the mass flow rate changes throughout the distributor specifically. The mass flow rate distribution through the collector is equal to that of the distributor.

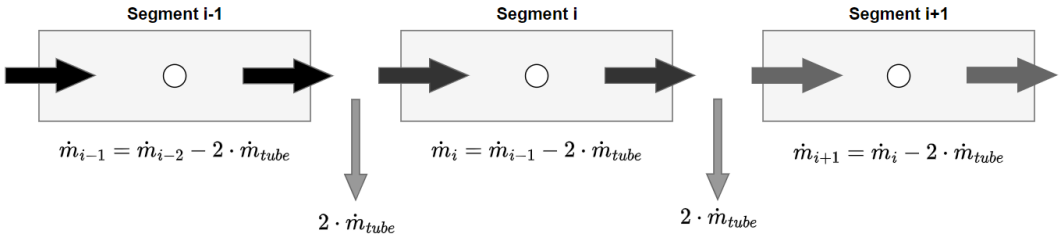


Figure 5: Illustration of how the mass flow rate changes through the segments of the tank heat exchanger's distributor, showing that after each segment, the mass flow decreases by twice that of the mass flow through a tube.

**Fluid and flow properties**

For each segment in the heat exchanger, the fluid properties ($c_p$, $h$, $k$, $Pr$, $\mu$, $\rho$) are calculated from the temperature and pressure at the segment's inlet, using CoolProp. Within each segment, these properties remain constant. With the mass flow rate, fluid density, and local geometry known, the fluid's velocity is computed using Equation 4, from which the flow properties can be calculated.

$$V = \frac{\dot{m}}{A_{crossec} \cdot \rho} \tag{4}$$

This allows for the calculation of the Reynold's number with Equation 5.

$$Re = \frac{D_{inner} \cdot \rho \cdot V}{\mu} \tag{5}$$

**Energy conservation and heat transfer**

Each segment of the heat exchanger is subjected to heat transfer with the fluid in the tank. This energy source is used to calculate the temperature at the outlet of each segment, which becomes the inlet temperature for the downstream segment. From the energy balance, the outlet temperature of each segment is calculated using Equation 6.

$$T_{out} = T_{in} + \frac{\dot{Q}}{c_p \cdot \dot{m}} \tag{6}$$

Because the orifices at each tube pair serve to equalize the pressure drop among all tubes, the pressure drop of the outermost tube pair is used as a representative for that of all tubes.

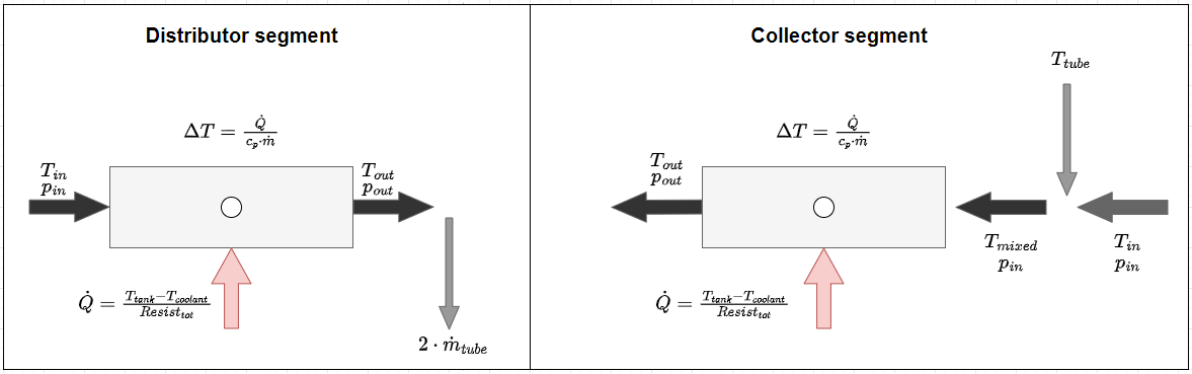


Figure 6: Overview of how temperature changes throughout a distributor and collector segment. In the distributor, the outlet temperature changes due to the heat transfer, while for the collector, mixing with the smaller tube's fluid happens prior to heat transfer.

The heat transfer that each segment receives from the tank fluid is calculated using the method of thermal resistivity, as shown in Equation 7. The temperature of the coolant is set to the local segment's inlet temperature.

$$Q = \frac{T_{tank} - T_{coolant}}{Resist_{tot}} \tag{7}$$

The total thermal resistance at a heat exchanger segment is equal to the sum of the thermal resistance from the internal forced convection, conduction through the walls, and from the external natural convection, as shown by Equation 8. Each of these three contributions is explained in more detail in the sections below. A graphical representation of this thermal resistance scheme is shown in Figure 7.

$$Resist_{tot} = Resist_{conv,inner} + Resist_{cond} + Resist_{conv,outer} \tag{8}$$

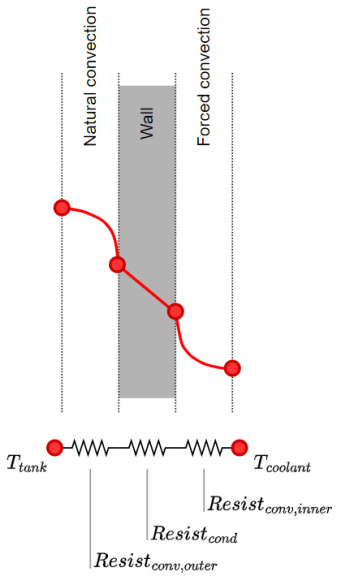


Figure 7: Thermal resistance scheme of the tank HEX.

**Momentum conservation and pressure drop**

The pressure drop through each heat exchanger segment is calculated using the inlet conditions of the segment and the friction factor flow correlations mentioned in subsection 3.2. The outlet pressure of each segment is calculated by simply subtracting the pressure drop from the inlet pressure. Thereafter, the outlet pressure of each section become the inlet pressure for the downstream segment.

$$p_{out} = p_{in} - \Delta p \tag{9}$$

## 3.2. Tubes internal convection

The heat transfer coefficient on the inner side of the tubes and manifolds needs to be computed in order to calculate the forced convective thermal resistivity $Resist_{conv,inner}$, which is defined using Equation 10. Here $U$ is the internal convective heat transfer coefficient in the tube section and $A$ is the internal surface area of the tube section.

$$Resist_{conv,inner} = \frac{1}{U_{conv,inner} \cdot A} \tag{10}$$

The heat transfer coefficient is calculated using the same approach as explained in the appendix "Thermodynamic modeling of gaseous flow through a coil-wound heat exchanger". The laminar flow correlation of Manlapaz-Churchill is used, while Petukhov-Popov's correlations is used for turbulent flow, with a linear transition between the two in case of transitional flow. Similarly, the pressure drop through the different components of the tank's tubular heat exchanger is also computed using the correlations described in the appendix "Thermodynamic modeling of gaseous flow through a coil-wound heat exchanger", by means of the Fanning friction factor, $f$ (see Equation 11). Mishra-Gupta's correlation for laminar flow and Ito's correlation for turbulent flow are used, assuming a straight and smooth tube. As there is nearly any tube coiling in this heat exchanger, no tube coiling correction factors are used for the flow correlations described in this paragraph.

$$\Delta p = 4 \cdot f \cdot L_{segment} \cdot 0.5 \cdot \rho \cdot V^2 / D_{hydr} \tag{11}$$

## 3.3. Radial conduction

The second contribution to the thermal resistance comes from the radial conduction through the metal walls ($Resist_{cond}$), which is calculated according to the conductive resistance equation through a hollow cylinder, as shown in Equation 12.

$$Resist_{cond,radial} = \frac{ln(D_{outer}/D_{inner})}{2 \cdot \pi \cdot k_{wall} \cdot L_{section}} \tag{12}$$

In this equation, the local thermal conductivity of the steel wall ($k_{wall}$) is calculated from an empirical correlation that relates the thermal conductivity of stainless steel 304 to the temperature. The correlation is shown in Equation 13, and is suggested by the National Institute of Standards and Technology [NIST], compiled from Mann [1977] and Touloukian and Ho [1976]. This correlation is applicable in the range of 4 to 300 Kelvin and can be seen in Figure 8. [NIST]

$$\begin{aligned} log(k_{steel}) = &-1.4087 + 1.3982 \cdot log(T) + 0.2543 \cdot (log(T))^2 - 0.6260 \cdot (log(T))^3 + 0.2334 \cdot (log(T))^4 \\ &+ 0.4256 \cdot (log(T))^5 - 0.4658 \cdot (log(T))^6 + 0.1650 \cdot (log(T))^7 - 0.0199 \cdot (log(T))^8) \end{aligned} \tag{13}$$

The wall temperature is not yet known at the moment the thermal conductivity of the wall is used to calculate the radial conductive resistance. Therefore, an initial estimate of the wall temperature is used to calculate the thermal conductivity with Equation 13. The estimate of the wall temperature is calculated using Equation 14.

$$T_{wall} = \frac{U_{conv,inner} \cdot A_{inner} \cdot T_{fluid,inner} + U_{conv,outer} \cdot A_{outer} \cdot T_{fluid,outer}}{U_{conv,inner} \cdot A_{inner} + U_{conv,outer} \cdot A_{outer}} \tag{14}$$

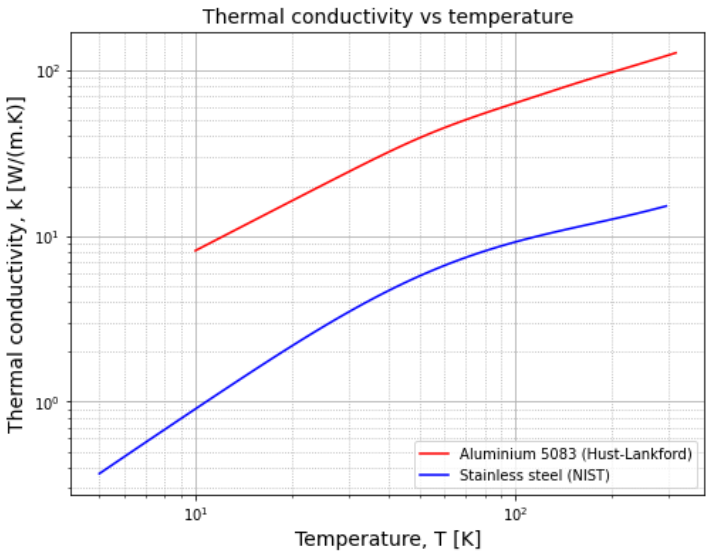


Figure 8: Thermal conductivity of Stainless steel 304 in function of temperature using Equation 13 from NIST and Aluminium-5083 from Hust-Lankford's model.[Woodcraft, 2005]

### 3.4. Tubes external convection

On the outside of the heat exchanger, there is no forced convection, however the heat transfer is a buoyancy driven natural convection. In this case the heat transfer coefficient is still defined in the same as in case of forced convection ($U = Nu \cdot k_{fluid}/D_{ref}$), however the Nusselt number is correlated differently. It is related to a the non-dimensional Rayleigh number and the fluid's Prandtl number. There exists a wide variety of correlations to calculate the Nusselt number for natural convection from tubes at different orientations. The correlation from Churchill and Chu [1975] for natural convection over heated horizontal tubes is used, as shown in Equation 15. Several authors have compared results of multiple correlations for horizontal tubes with experimental and CFD results, yielding error margins typically in the order of 20% to 50%. [Atayilmaz and Teke, 2009] It is important to keep this relatively large error range in mind when interpreting the results from the simulation.

$$Nu_{tank} = \left(0.6 + 0.387 \cdot \left(\frac{Ra}{\left[1 + (0.559/Pr_{tank})^{9/16}\right]^{16/9}}\right)^{1/6}\right)^2 \tag{15}$$

As shown in Equation 16, the Rayleigh number in this equation can be calculated from the Grashof and Prandtl numbers, defined by Equation 17 and Equation 18 respectively.

$$Ra = Pr_{tank} \cdot Gr \tag{16}$$

$$Gr = g \cdot \beta_{tank} \cdot D_{outer}^3 \cdot (T_{fluid} - T_{wall}) \cdot \left(\frac{\rho_{tank}}{\mu_{tank}}\right)^2 \tag{17}$$

$$Pr_{tank} = c_{p_{tank}} \cdot \mu_{tank}/k_{tank} \tag{18}$$

Equation 17 depends on the Earth's gravity ($g$), coefficient of volume expansion of the fluid ($\beta$), the temperature difference between the fluid and wall, the fluid density ($\rho$), and fluid dynamic viscosity ($\mu$).

With the previously mentioned equations, the outer heat transfer coefficient of the heat exchanger segments is calculated and used to calculate the tank-side convection's contribution to the thermal resistance, using Equation 19. Here $A$ is the external surface area of the tube segment.

$$Resist_{conv,outer} = \frac{1}{U_{conv,outer} \cdot A} \tag{19}$$

## 4. Tank heat exchanger model validation

The tank heat exchanger code is validated against the data from NASA's Ground Operations Demonstration Unit's (GODU) heat exchanger as described in the paper "Integrated Heat Exchanger Design for a Cryogenic Storage Tank".[Fesmire et al., 2014] The lay-out of this heat exchanger inside its tank can be seen in Figure 9. The reason for choosing this validation data is primarily based on the excellent documentation that is available on NASA's GODU tank and also on the similarity of the conditions to the current study.

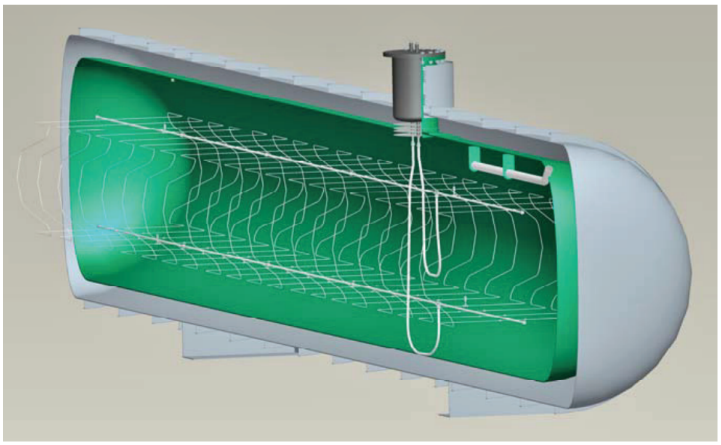

Figure 9: NASA GODU tank and heat exchanger lay-out, from Fesmire et al. [2014].

subsection 4.1 gives an overview of the program inputs that have been used for validation. Additionally, this section also provides the performance parameters of the heat exchanger that will be compared to the program's results (as presented in subsection 4.3. In subsection 4.2, the general approach towards validation of the program is treated. Finally, a conclusion on the validation efforts can be found in subsection 4.4.

## 4.1. Validation data

This subsection provides the reader with the inputs that have been used to validate the program, alongside with an explanation how some of these inputs were obtained and which assumptions were made during the validation process.

**Performance**

The heat transfer between the cooling fluid and tank fluid will be used as the main metric for validation, alongside with the coolant pressure drop over the heat exchanger. For the nominal case where the liquid hydrogen inside the tank has a temperature of 20 Kelvin, the effective cooling power of the heat exchanger is said to be 800 Watt, while the cooling power is said to be 420 Watt in case the liquid hydrogen has a temperature of 17 Kelvin. Additionally, for both cases it is mentioned that the final temperature difference between the cooling fluid and the hydrogen is less than 0.5 Kelvin.

In case of the 20 Kelvin hydrogen, the cooling fluid's pressure drop over the heat exchanger is said to be 3 kPa. In case of 17 Kelvin hydrogen, no specific pressure drop value is mentioned, however it is said to have a similar pressure drop. [Fesmire et al., 2014]

**Geometry**

The following geometry is clearly stated in the paper of Fesmire et al. [2014]:

- Number of tubes: 40
- Tube outside diameter: 0.0046 m
- Manifold outer diameter: 0.025 m (for both distributor and collector)
- Manifold length: 18.5 m (for both distributor and collector)

The inner diameter of the liquid hydrogen tank is not stated in the aforementioned paper, however a value of 2.9 meters is mentioned by several other papers on NASA's GODU tank, for example by Swanger et al. [2016].

The inner diameter of the tubes and manifolds is required in the tank heat exchanger model, however Fesmire et al. [2014] only provide the outer diameters. It is however stated that schedule 10 piping are used, from which the pipe thickness can be deducted using data provided by stainless steel tube providers. A wall thickness of 2.11 mm and 1.65 mm was found to correspond with the outer diameters for the manifolds and tubes respectively. Hence the tube inner diameter is calculated using Equation 20.

$$D_{inner} = D_{outer} - 2 \cdot t_{wall} \tag{20}$$

**Fluid conditions**

NASA's GODU tank heat exchanger used pure helium as a cooling fluid, with a mass flow rate of 0.022 kg/s. The tank itself is filled with liquid hydrogen at a temperature of 20 Kelvin. The nominal pressure of the liquid hydrogen inside the tank is not directly provided, however it can be deducted from Figure 6 in their paper. At a tank pressure of 95 kPa, the heat transfer matches the previously mentioned heat transfer of 800 W. [Fesmire et al., 2014] Because the heat exchanger's performance parameters are also provided at a liquid hydrogen temperature of 17 Kelvin, yielding 420 W of cooling power, this case will be used as a second data point for validation.

The temperature and pressure at which the helium coolant enters the heat exchanger are not stated by Fesmire et al. [2014]. A reasonable estimate can be made based on a graph providing the cryocooler's cooling power as a function of the tank temperature. The cooler seems to provide zero cooling power at a temperature of about 13.3 Kelvin. Based on this, the assumption is made that the cryocooler delivers helium at 13.3 Kelvin. Fesmire et al. [2014] also state that the cooler delivers a capacity of 850 W, while connecting line losses decrease this value by 50 W. Therefore the inlet temperature of the tank heat exchanger is 13.3 Kelvin plus an amount that is equivalent to a 0.022 kg/s helium flow, subjected to 50 W, as shown by Equation 21. This results in a heat exchanger inlet temperature of 13.65 Kelvin.

$$T_{hex,in} = 13.3 + \frac{Q_{loss}}{c_p \cdot \dot{m}} \tag{21}$$

The inlet pressure of the helium coolant is however not mentioned. Due to the proximity to the critical point of helium, the pressure has a relatively significant influence on the helium density and thereby affects the flow velocity through the heat exchanger. The approach to estimate the heat exchanger pressure in the tank heat exchanger validation process is explained in more detail in subsection 4.2.

## 4.2. Validation approach

Prior to comparing the simulated results with those of Fesmire et al. [2014], a grid independence study is performed to assess the model's error sensitivity to the number of segments in the tubes.

As explained in subsection 4.1, all model inputs are known, except for the heat exchanger inlet pressure. Therefore, two different approaches will be used to estimate the helium pressure. The results for both approaches will then be compared to each other and the results from Fesmire et al. [2014] to assess their agreement.

**Approach A**

For approach A, the inlet pressure of the heat exchanger is determined such that the total heat transfer of the heat exchanger exactly matches that of the experiment (800 W at 20 K hydrogen). Subsequently the pressure drop across the heat exchanger is compared to that mentioned by Fesmire et al. [2014]. Additionally, at this inlet pressure, the heat transfer and pressure drop results for the case at 17 K hydrogen are compared to those of NASA's GODU.

**Approach B**

For approach B, the inlet pressure of the heat exchanger is determined such that the pressure drop matches the 3 kPa value that is mentioned by Fesmire et al. [2014], after which the heat transfer resemblance can be evaluated. Similarly to approach A, the heat transfer and pressure drop are also evaluated in case of 17 K hydrogen, using the newly found heat exchanger inlet pressure.

## 4.3. Validation results

**Geometry**

The geometry of the heat exchanger model presented in this work is a simplification of NASA's GODU heat exchanger. Therefore several geometrical parameters are compared to assess their similarity and identify potential sources of errors that could contribute to a reduced accuracy of the model.

Fesmire et al. [2014] mentions that the combined length of the tubes is 144 meters (6.038 m each). The model described in this chapter simplifies the tube geometry by neglecting rounded corners and also makes some assumptions regarding the tube geometry (explained in section 2). This was found to result in a difference in tube length of -0.062 meter, or -1.02% compared to the 6.038 meters of the GODU. The shorter tubes of the model are expected to decrease the total surface area and thereby decrease the heat transfer.

Another difference between this study's model and the GODU heat exchanger is that the former has the cooling fluid entrance and exit exactly at the mid-point of the manifolds, while for the latter the entrance and exit are located 6 tube pairs from the center. The more ideal entrance/exit location of this study's model is expected to result in a slightly higher heat transfer.

**Mesh sensitivity**

Prior to comparing the results from the simulation with those of the validation data, a sensitivity analysis was performed to assess the minimum required number of segments for the heat exchanger tubes to guarantee an accurate solution. The tank heat exchanger rating program was used to calculate the pressure drop and heat transfer results for the number of tube segments ranging from 3 to 600. The change in the cooling power between 600 segments and 601 segments is only $2.73 \cdot 10^{-5}$. This value was deemed low enough for the cooling power to be considered a converged solution. From the difference between the heat transfer at various number of segments and the converged value at 600 segments, a minimum number of segments can be determined. Considering that several assumptions (see section 2) introduce errors in the order of a percentage, an error threshold of 0.1% was considered sufficient. Figure 12 shows that the this 0.1% threshold is reached in case 117 or more segments are used. Therefore the validation and cases described later in this study have 117 segments. The error of the pressure drop was found to be lower ($< 5 \cdot 10^{-3}$) in case of 117 segments, as can be seen in Figure 13

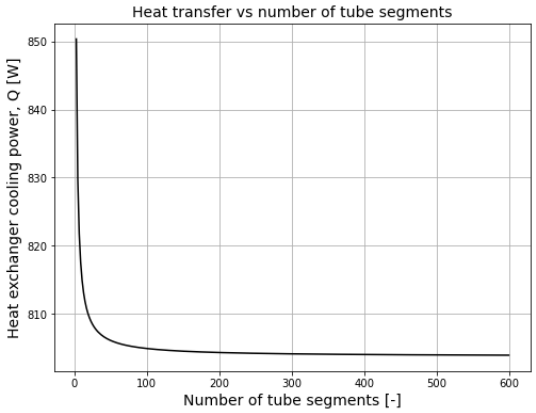


Figure 10: Tank heat exchanger cooling power as function of the number of segments in each of the tubes, showing convergence.

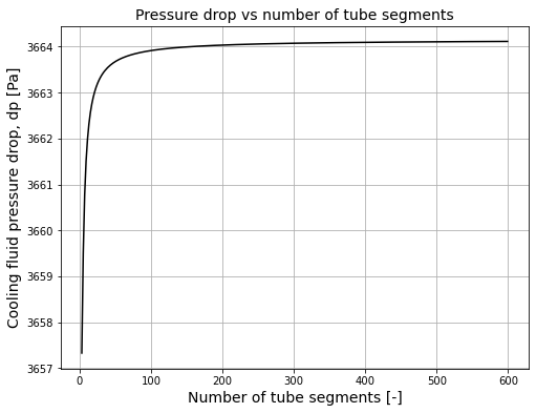


Figure 11: Tank heat exchanger pressure drop as function of the number of segments in each of the tubes, showing convergence.

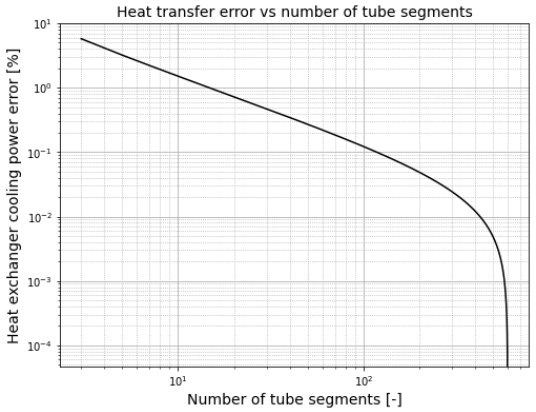


Figure 12: Tank heat exchanger cooling power error as function of the number of segments in each of the tubes. Note that the reference converged value is set to be that at 600 segments.

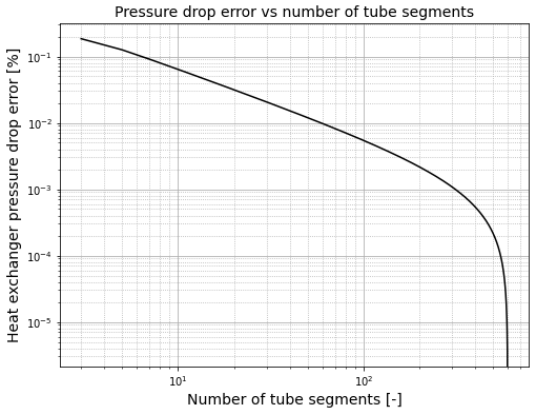


Figure 13: Tank heat exchanger pressure drop error as function of the number of segments in each of the tubes. Note that the reference converged value is set to be that at 600 segments.

**Approach A**

At a liquid hydrogen temperature of 20 K, the heat transfer of the validation data (800 W) was achieved by the tank heat exchanger program at an inlet pressure of 11.184 bar. This resulted in a pressure drop of 3.869 kPa, as compared to the 3 kPa stated by Fesmire et al. [2014].

When using this 11.184 bar inlet pressure, the heat transfer and pressure drop in case of a hydrogen temperature of 17 Kelvin were found to be 408.56 W and 3.141 kPa. As shown in Table 1, the heat transfer corresponds well (-2.72%) with the 420 W from NASA. No exact value for the pressure drop error can be given in case of the 17 K hydrogen case, because the pressure drop is only said to be very similar to 3 kPa, to which the model differs by 4.7%.

**Approach B**

Using approach B as explained in subsection 4.2, the pressure drop of 3 kPa was achieved by the tank heat exchanger model when the heat exchanger inlet pressure has a value of 14.63 bar. The resulting heat transfer equals 821.76 W, which deviates 2.72% from the 800 W from Fesmire et al. [2014].

Using an inlet pressure of 14.63 bar, the heat transfer and pressure drop in case of a hydrogen temperature of 17 Kelvin were found to be 421.49 W and 2.436 kPa respectively. The corresponding errors are therefore 0.35% and 18.8% for the heat transfer and pressure drop respectively, although it should be noted that the exact pressure drop for the case of 17 K hydrogen was not mentioned by Fesmire et al. [2014].

| | | **Heat transfer power, $\dot{Q}$ [W]** | | | **Pressure drop, $\Delta$ p [kPa]** | | |
|---|---|---|---|---|---|---|---|
| | **Inlet pressure $p_{in}$ [kPa]** | **Current model** | **NASA GODU** | **Difference** | **Current model** | **NASA GODU** | **Difference** |
| **Approach A: matching heat transfer at 20 K hydrogen** | | | | | | | |
| $H_2$ at 20 K | 1118.4 | 800 | 800 | NA | 3.869 | 3.0 | +28.97 % |
| $H_2$ at 17 K | 1118.4 | 408.56 | 420 | -2.72 % | 3.141 | ~3.0 * | +4.7 % * |
| | | | | | | | |
| **Approach B: matching pressure drop at 20 K hydrogen** | | | | | | | |
| $H_2$ at 20 K | 1463.0 | 821.76 | 800 | +2.72 % | 3.0 | 3.0 | NA |
| $H_2$ at 17 K | 1463.0 | 421.49 | 420 | +0.35 % | 2.436 | ~3.0 * | -18.8% * |

Table 1: Comparison between the heat transfer and pressure drop results. *The pressure drop in case of a hydrogen temperature of 17 Kelvin is mentioned to be similar to 3 kPa, however no exact value is provided.

Additional to the pressure drop and heat transfer, Fesmire et al. [2014] mention that the temperature difference between the liquid hydrogen and the cooling fluid at the exit of the heat exchanger is below 0.5 K for all the aforementioned cases. The results from the simulations shown in Table 1 featured a temperature difference between tank fluid and heat exchanger outlet temperature between 0.326 and 0.355 Kelvin, which is in line with the data from NASA's GODU.

A visual representation of the 3D temperature distribution of the helium inside the heat exchanger can be seen in Figure 14 alongside with a plot of the temperature change along the fluid path in Figure 15. Both clearly show the non-negligible heat transfer contribution of the distributor towards the total heat transfer. Note that the collector manifold experiences a slight negative temperature gradient, as it progressively receives colder inflow of coolant from the tubes.

**Mass**

To the best of the author's knowledg, the mass of NASA's GODU heat exchanger is not mentioned in literature, making it not possible to validate the mass estimate results of the model.

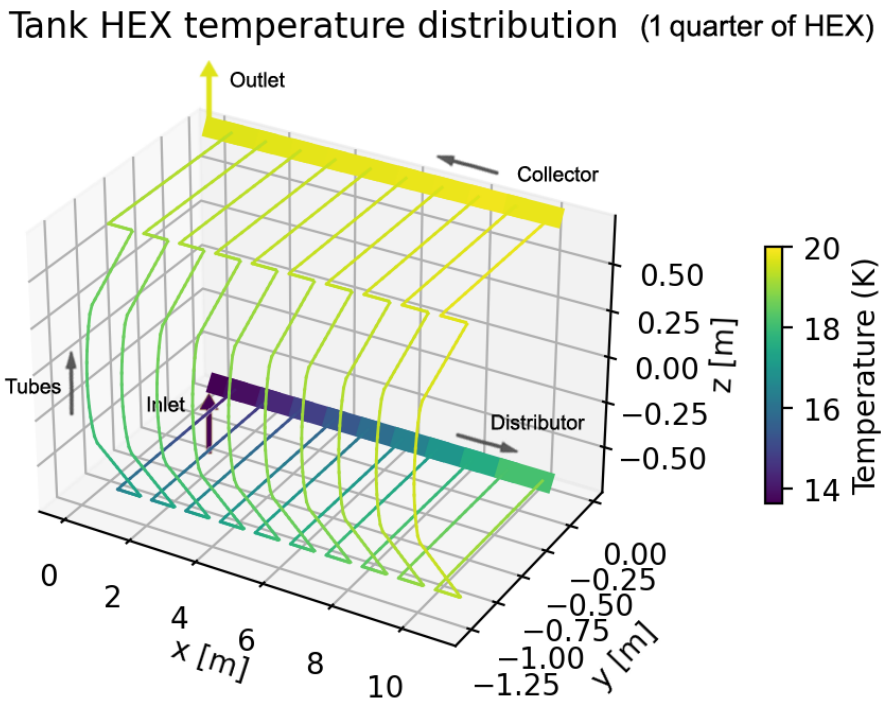


Figure 14: 3D Temperature distribution results of the tank heat exchanger validation results, replicating NASA's GODU heat exchanger (for Hydrogen at 20 K). Note that only one quarter of the heat exchanger is shown, as the results can be mirrored over the XZ and YZ planes.

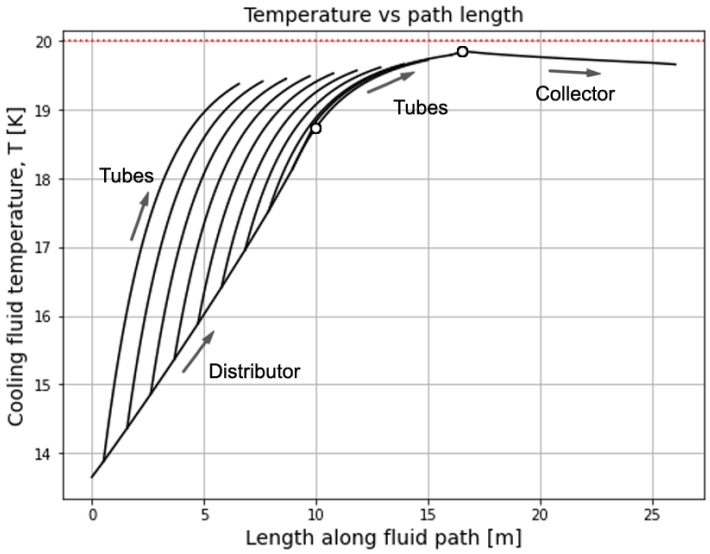


Figure 15: Temperature distribution along the flow path of the coolant through the heat exchanger, from the simulated data of NASA's GODU heat exchanger (for Hydrogen at 20 K). Note that each of the tubes connects to a section of the collector.

### 4.4. Validation conclusion

Validation of the tank heat exchanger model was successfully performed with data from by NASA's GODU heat exchanger. Heat transfer results showed a close match, in the order of several percent. Pressure drop results deviated more, up to around 30%, which is to be expected from the simplifications and assumptions made for this model on top of the typical error margins of the friction factor's empirical correlations. Mesh convergence was established to be satisfied at a minimum number of 117 segments for the tubes, providing an error below 0.1%.

## 5. Tank heat exchanger conclusion and recommendations

A tank heat exchanger model was developed to calculate the performance of a heat exchanger for a given geometry, and to calculate the mass of a heat exchanger for a given cooling power. The heat exchanger design was strongly based on that of NASA's Ground Operations Unit (GODU) heat exchanger for a 125000 liter liquid hydrogen tank [Fesmire et al., 2014], with which the model was successfully validated, as shown in section 4.

The capabilities of the current model are built to accommodate the cases of the current study, being the steady state cooling of a large liquid hydrogen tank. However, there are ample opportunities to further increase the range of cases to which this program could be used for. Several examples of suggested features to implement are: inclusion of heat transfer with a gaseous and liquid tank fluid to allow for a partially filled tank, heat transfer correlations for natural convection in zero-g environments for space-based cooling of liquid hydrogen tanks, or the option of having heat transfer enhancement features in or on the tubes. Additionally, the structural aspect of the heat exchanger and the structural interface with the tank are relatively simple for the current model and offer another opportunity for future work to provide a more encompassing mass estimate of the whole cooling system.

# References


S. O. Atayilmaz and I. Teke. Experimental and numerical study of the natural convection from a heated horizontal cylinder. International Communications in Heat and Mass Transfer, Vol. 36 (No.7):pp. 731–738, 2009. doi: 10.1016/j.icheatmasstransfer.2009.03.017.

Ian H. Bell, Jorrit Wronski, Sylvain Quoilin, and Vincent Lemort. Pure and pseudo-pure fluid thermophysical property evaluation and the open-source thermophysical property library coolprop. Industrial & Engineering Chemistry Research, Vol. 53(No. 6):pp. 2498–2508, 2014. doi: 10.1021/ie4033999. URL `http://pubs.acs.org/doi/abs/10.1021/ie4033999`.

S. W. Churchill and H. H. S. Chu. Correlating equations for laminar and turbulent free convection from a horizontal cylinder. International Journal of Heat and Mass Transfer, Vol. 18(No.9):pp. 1049–1053, 1975.

J.E. Fesmire, T.M Tomsik, T. Bonner, J.M. Oliveira, H.J. Conyers, W.L. Johnson, and W.U. Notardonato. Integrated heat exchanger design for a cryogenic storage tank. AIP conference proceedings, Vol. 18:pp. 1365–1372, 2014. doi: 10.1063/1.4860865.

D. Mann. LNG materials and fluids: a user's manual of property data in graphic format. John Wiley & Sons Inc, Hoboken (USA), 1977. ISBN 0-471-32171-0.

NIST. Material properties: 304 stainless (uns s30400). National Institute for Standards and Technology, Applied Chemicals and Materials Division. Last accessed on 01/08/2023. `https://trc.nist.gov/cryogenics/materials/304Stainless/304Stainless_rev.htm`.

E.M. Sparrow, R. Eichhorn, and J.L. Gregg. Combined forced and free convection in a boundary layer flow. Physics of Fluids, Vol. 2(No. 3):pp. 319–328, 1959. doi: 10.1063/1.1705928.

A. M. Swanger, W. U. Notardonato, W. L. Johnson, and T. M. Tomsik. Integrated refrigeration and storage for advanced liquid hydrogen operations. International Cryocooler Conference 19, San Diego (USA), 2016.

Y.S. Touloukian and C.Y. Ho. Thermophysical properties of selected aerospace materials, part ii: Thermophysical properties of seven materials. International Journal of Heat and Mass Transfer, pages pp. 39–46, 1976.

A. L. Woodcraft. Predicting the thermal conductivity of aluminium alloys in the cryogenic to room temperature range. Cryogenics, Vol.45, No.6, 2005. doi: 10.1016/j.cryogenics.2005.02.003.

## Tank heat exchanger program inputs and outputs

| Inputs for sizing program | | | |
|---|---|---|---|
| **Variable description** | **Variable** | **Unit** | **Data type** |
| Target heat exchange (negative for cooling) | $\dot{Q}$ | $W$ | float |
| Coolant inlet temperature | $T_{in}$ | $K$ | float |
| Coolant inlet pressure | $p_{in}$ | $Pa$ | float |
| Tank fluid temperature | $T_{tank}$ | $K$ | float |
| Tank fluid pressure | $p_{tank}$ | $Pa$ | float |
| Target effectiveness | $\epsilon$ | $-$ | float |
| Coolant fluid name | $fluid_{hex}$ | $-$ | string |
| Tank fluid name | $fluid_{tank}$ | $-$ | string |
| Tank inner radius | $R_{tank}$ | $m$ | float |
| Length of the tank's cylindrical section | $L_{tank,cyliner}$ | $m$ | float |
| Heat exchanger tube wall thickness | $t_{tube}$ | $m$ | float |
| Distributor and collector wall thickness | $t_{distributor}$ | $m$ | float |
| Density of the heat exchanger material | $\rho_{metal}$ | $kg/m^3$ | float |
| Boolean used to plot several variables | plotting | NA | boolean |
| Variable that controls how much information is printed<br><0: Suspend all text<br>= 0: Only warnings<br>>0: Final solution and warnings | verbosity | - | float |

Table 2: Program inputs for the sizing program of the tank heat exchanger.

# Literature study

## Reverse turbo-Brayton cryocoolers for zero boil-off in airborne liquid hydrogen tanks

by

Thomas Britting

to obtain the degree of Master of Science
at the Delft University of Technology,

Student number: 4554116
Project duration: November 1, 2021 – May 31, 2024
Supervised by: Prof. dr. ir. C. De Servi, TU Delft
F. Beltrame, TU Delft

TU Delft

# Contents

# List of Figures

# List of Tables

# List of Abbreviations

| Abbreviation | Meaning |
|---|---|
| ADC | Adiabatic Demagnetisation Cooler |
| CFD | Computational Fluid Dynamics |
| COP | Coefficient Of Performance |
| CWHEX | Coil-Wound Heat Exchanger |
| FIR | Fixed ISIM Radiators |
| GM | Gifford-McMahon |
| HEX | Heat Exchanger |
| ISIM | Integrated Science Instrument Module |
| JT | Joule-Thomson |
| LNG | Liquefied Natural Gas |
| LMTD | Log Mean Temperature Difference |
| MTD | Mean Temperature Difference |
| MRI | Magnetic Resonance Imaging |
| NICMOS | Near Infrared Camera and Multi-Object Spectrometer |
| NIST | National Institute of Standards and Technology |
| NTU | Number of Thermal Units |
| PFHEX | Plate-Fin Heat Exchanger |
| PT | Pulse-Tube |
| RTB | Reverse Turbo-Brayton |
| RTBC | Reverse Turbo-Brayton Cooler |
| SOFIA | Stratospheric Observatory For Infrared Astronomy |

# List of Symbols

## Roman symbols

| Symbol | Meaning | Unit |
|---|---|---|
| $A$ | Area | $m^2$ |
| $C$ | Heat capacity rate | $J \cdot s^{-1} \cdot K^{-1}$ |
| $C^*$ | Ratio of heat capacity rates | $-$ |
| $c_p$ | Specific heat at constant pressure | $J \cdot kg^{-1} \cdot K^{-1}$ |
| $c_v$ | Specific heat at constant volume | $J \cdot kg^{-1} \cdot K^{-1}$ |
| $d$ | Distance between two points | $m$ |
| $E$ | Emissive power | $W \cdot m^{-2}$ |
| $F_{A \to B}$ | View factor from object A to B | $-$ |
| $G$ | Irradiance | $W \cdot m^{-2}$ |
| $Gr_x$ | Grashof number with reference dimension x | $-$ |
| $H$ | Enthalpy | $J$ |
| $h$ | Specific enthalpy | $J \cdot kg^{-1}$ |
| $h_{conv}$ | Convective heat transfer coefficient | $J \cdot kg^{-1}$ |
| $h_{overall}$ | Overall heat transfer coefficient | $J \cdot kg^{-1}$ |
| $J$ | Radiance | $W \cdot m^{-2}$ |
| $k$ | Heat conductivity | $W \cdot m^{-1} \cdot K^{-1}$ |
| $NTU$ | Number of Transfer Units | |
| $Nu_x$ | Nusselt number with reference dimension x | $-$ |
| $p$ | Pressure | $Pa$ |
| $P$ | Temperature effectiveness | $-$ |
| $Pe$ | Péclet number | $-$ |
| $Pr$ | Prandtl number | $-$ |
| $\dot{Q}$ | Thermal power | $W$ |
| $\dot{q}$ | Heat flux | $W \cdot m^{-2}$ |
| $\dot{q}_{int}$ | Internal heat generation rate per unit volume | $W \cdot m^{-3}$ |
| $R$ | Specific heat constant | $J \cdot kg^{-1} \cdot K^{-1}$ |
| $R$ | Thermal resistivity | $K \cdot s/J^{-1}$ |
| $Ra_x$ | Rayleigh number with reference dimension x | $-$ |
| $R_C$ | Heat capacity rate ratio | $-$ |
| $Re_x$ | Reynolds number with reference dimension x | $-$ |
| $Ri$ | Richardson number | $-$ |
| $s$ | Entropy | $J \cdot K^{-1}$ |
| $T$ | Temperature | $K$ |
| $V$ | Velocity | $m/s$ |
| $\dot{W}$ | Mechanical power | $W$ |
| $x$ | Spatial location | $m$ |
| $Z$ | Compressibility factor | $-$ |

## Greek symbols

| Symbol | Meaning | Unit |
|---|---|---|
| $\alpha_{surf}$ | Surface absorptivity | $-$ |
| $\beta$ | Coefficient of thermal expansion | $K^{-1}$ |
| $\beta$ | Non-dimensional environmental heat leak | $-$ |
| $\gamma$ | Specific heat ratio | $-$ |
| $\Delta$ | Finite difference | $-$ |
| $\epsilon_{surf}$ | Surface emissivity | $-$ |
| $\epsilon$ | Heat exchanger effectiveness | $-$ |
| $\epsilon_n$ | New heat exchanger effectiveness | $-$ |
| $\eta$ | Efficiency (or isentropic efficiency in case of turbomachinery) | $-$ |
| $\lambda$ | Wavelength | $m$ |
| $\mu$ | Dynamic viscosity | $kg \cdot m^{-1} \cdot s^{-1}$ |
| $\nu$ | Kinematic viscosity | $m^2 \cdot s$ |
| $\rho$ | Density | $kg \cdot m^{-3}$ |
| $\psi$ | Angle with respect to the normal of a surface | $rad$ |
| $\Psi$ | Non-dimensional effective mean temperature difference | $-$ |
| $\omega$ | Acentric factor of a molecule | $-$ |

## Subscripts

| Symbol | Meaning |
|---|---|
| $X_C$ | Cold |
| $X_{carn}$ | Carnot |
| $X_{cond}$ | Conductive |
| $X_{comp}$ | Compressor |
| $X_{conv}$ | Convective |
| $X_{crit}$ | Critical point of fluid |
| $X_{env}$ | Environment |
| $X_{ext}$ | External |
| $X_H$ | Hot |
| $X_{HEX}$ | Heat exchanger |
| $X_{int}$ | Internal |
| $X_{max}$ | Maximum |
| $X_{mean}$ | Average |
| $X_{min}$ | Minimum |
| $X_n$ | In the direction normal to a surface |
| $X_p$ | Property for an isobaric process |
| $X_{rec}$ | Recuperator |
| $X_{rad}$ | Radiative |
| $X_{red}$ | Reduced fluid property |
| $X_{ref}$ | Reference |
| $X_{reject}$ | Rejection |
| $X_{sat}$ | At saturated conditions |
| $X_{surf}$ | At the surface |
| $X_{trip}$ | Triple point of fluid |
| $X_{turb}$ | Turbine |
| $X_v$ | Property for an isochoric process |
| $X_\psi$ | In a direction with angle $\psi$ with respect to the normal of a surface |

# 1 Introduction

The increasing growth in greenhouse gas emissions in recent history has started a global movement towards the development of more sustainable technologies. In the search for alternative non-carbon-based fuel sources, hydrogen has been highlighted as a promising candidate. The low density of hydrogen strongly hampers the feasibility of room temperature hydrogen as an airborne fuel source, making the use of liquefied hydrogen much more attainable. The implementation of liquid hydrogen as an airborne fuel source however comes with many challenges that require the maturization of multiple technologies.

The use of liquid hydrogen as a fuel source for aircraft has already been demonstrated in the last century (NASA, 1978, Sosounov and Orlov, 1990) and zero boil-off for liquid hydrogen fuel tanks have already been proven for ground systems (Plachta, 1999, Hastings et al., 2010, Plachta, 2004). However, achieving zero boil-off onboard liquid hydrogen aircraft is still an unproven concept. Zero boil-off can offer the potential of fuel savings onboard future liquid hydrogen powered aircraft if the cryocooler mass and power consumption are sufficiently low. However, there exists a knowledge gap on the thermodynamic performance and specific power of cryocoolers for airborne applications. Reverse turbo-Brayton cryocoolers have been identified as a favorable candidate for broad area cooling of cryogenic fuel tanks. Therefore this study aims to perform a sensitivity study on a reverse turbo-Brayton cryocooler to achieve zero boil-off in a liquid hydrogen powered aircraft fuel tank by the development of a numerical simulation tool for an RTBC, focuses on the heat exchangers.

This document is a summary of the literature study that was performed to familiarize with the concepts and previous work that are necessary to perform the aforementioned study. First, an overview of the properties and behavior of fluids at cryogenic temperatures is presented in chapter 2, with a particular focus on hydrogen and helium. Thereafter, chapter 3 summarizes cryocooler technologies and applications alongside a survey that was performed on the performance of existing cryocoolers. Reverse turbo-Brayton cryocoolers are covered in more detail in chapter 4, including the derivation of an analytical model for an RTBCs coefficient of performance. Due to the strong contribution of heat exchangers to the RTBC mass, this study particularly emphasizes on the modeling methodologies and existing technologies of heat exchangers in chapter 5. Finally, the research question and scope of this thesis study is defined in chapter 6

# 2

# Characteristics of cryogenic fluids

The upper temperature limit of what is defined to be cryogenic was defined to lay at 120 K by the 13th IIR International Congress of Refrigeration in 1971. Other definitions of what is considered to be cryogenic have been used as well, such as the 93 K threshold, set by the National Institute of Standard and Technology. Other definitions of this cryogenic temperature limit are mentioned in literature, generally between 90 K and 130 K.

With a boiling point lower than 93 K at standard atmospheric pressure, the following elements can be considered to be cryogenic fluids, according to the two aforementioned definitions: helium, hydrogen, neon, nitrogen, fluorine, argon, and oxygen. Gasses with molecules consisting out of multiple elements (e.g. $CH_4$) or compound gasses (e.g. air) can also be considered cryogenic fluids, however are not listed here for brevity. Additionally, a distinction between the two most common isotopes of helium can be made: helium-4 ($^4He$) and helium-3 ($^3He$). These exhibit different thermo-physical properties, which is exploited in the dilution refrigeration cooling cycle described in subsection 3.1.10. The boiling temperatures at standard atmospheric pressure of the cryogenic fluids mentioned above are presented in Table 2.1. Additionally, the effect of pressure on the boiling, or saturation, point of different typically used cooling fluids can be seen in Figure 2.1

| **Fluid** | **Boiling T [K] (at 1 atm pressure)** |
|---|---|
| $^3He$ | 3.19 |
| $^4He$ | 4.21 |
| $H_2$ | 20.27 |
| $Ne$ | 27.09 |
| $N_2$ | 77.09 |
| $F_2$ | 85.24 |
| $Ar$ | 87.24 |
| $O_2$ | 90.18 |

Table 2.1: Boiling temperatures of cryogenic fluids, consistent of identical elements.Bar-Cohen, 2016

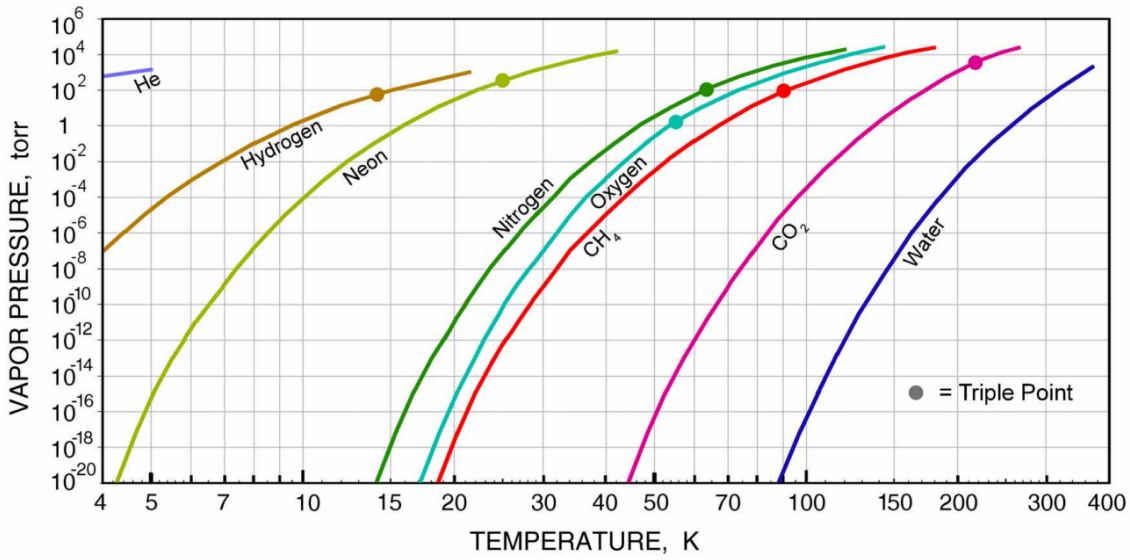


Figure 2.1: Saturation temperature of different fluids as function of pressure. (Bar-Cohen, 2016)

At cryogenic temperatures, the vibrational energy of the molecules becomes less dominant compared to the intermolecular forces. This causes the fluid properties to deviate from those that are approximated by the ideal gas law. This deviation increases as temperature decreases, because the vibrational energy of a molecule is directly proportional to the temperature. Additionally, fluid properties deviate more from the ideal gas law at higher pressures. The deviation of the ideal fluid properties, compared to those of the real gas can be expressed using a compressibility factor, Z. This parameter is defined as the ratio of the volume a real gas compared to an ideal gas. This can be expressed in terms of the densities, shown in Equation 2.1. The compressibility factor can be used as a correction term to calculate real gas properties from the ideal gas law.

$$Z = \frac{V_{real}}{V_{ideal}} = \frac{\rho_{ideal}}{\rho_{real}} \tag{2.1}$$

The equation of state for ideal gasses (Equation 2.2) can be used to express the compressibility factor in terms of pressure and temperature, shown in Equation 2.3.

$$p = R \cdot \rho \cdot T \tag{2.2}$$

$$Z = \frac{p}{\rho_{real} \cdot T \cdot R_{ideal}} \tag{2.3}$$

The compressibility factor is a function of both pressure and temperature of the fluid. However there is a temperature at which the attractive and repulsive forces of the gas cancel out, making the compressibility factor equal to a value close to unity, independent of the pressure: the Boyle temperature. Close to this temperature, the ideal gas law very well approximates a fluid's properties. Above the Boyle temperature, the compressibility factor has a positive value and grows larger with increasing pressure. There is however much variation in the reported experimental values for the Boyle temperature, as indicated by Estrada-Torres, 2007.

Another fluid property that is directly linked to real gas effects, is the the Joule-Thomson coefficient (JT coefficient). The JT expansion process does not take place for ideal gases and can either cool down or warm up a fluid, depending on the pressure and temperature conditions of the expansion process. The inversion temperature of a fluid is defined as the temperature below which a JT expansion process, often called throttle, results in a temperature decrease. This inversion temperature is pressure dependent. Nearly all gases have inversion temperatures above room temperatures at atmospheric pressure, except for helium, hydrogen and neon. These gases have to be cooled down below their

inversion temperatures first, before JT cooling can be used to cool the fluid down further.

There are other fluid properties that change notably at cryogenic temperatures, such as the heat conductivity of a fluid, that can decrease with more than an order of magnitude compared to ambient conditions. For most fluids, the thermal conductivity decreases linearly with a decreasing temperature. (Poling et al., 2001) This makes it more challenging for cryogenic heat exchangers to change the bulk temperature of a fluid. Similarly to the heat conductivity, the viscosity of a fluid can change as much as an order of magnitude when comparing the ambient to low cryogenic temperatures.

Fluid properties also change drastically when approaching the critical point or vapor dome. At temperatures and pressures above the critical point, there is no distinct difference between the gaseous and liquid phase, hence the fluid is called supercritical. Poling et al., 2001

Some fluid properties can be calculated with simplified equations, instead of interpolating a large database of properties. Although this results in deviations from the actual fluid properties, there is usually a significant improvement in computational cost, as only one or a few simple equations have to be solved, instead of processing a large database. This can be favorable depending on the required accuracy of the application.
One example of such simplification is the **Shomate equation**, where the enthalpy, entropy and specific heat at constant pressure are approximated using polynomials, as shown in Equation 2.4, Equation 2.5, and Equation 2.6 respectively. Shomate equations make use of 8 coefficients, denoted by the letters A, B, C, D, E, F, G, and H. These coefficients only have a validity within a specified temperature range. Linstrom and Mallard, 2023

$$H^o - H^o_{298.15} = A\cdot\left(\frac{T}{1000}\right)+B/2\cdot\left(\frac{T}{1000}\right)^2+C/3\cdot\left(\frac{T}{1000}\right)^3+D/4\cdot\left(\frac{T}{1000}\right)^4-E\left(\frac{T}{1000}\right)^{-1}+F-H \quad (2.4)$$

$$s^o = A\cdot ln\left(\frac{T}{1000}\right)+B\cdot\left(\frac{T}{1000}\right)+C\cdot\left(\frac{T}{1000}\right)^2+D\cdot\left(\frac{T}{1000}\right)^3-E/2\cdot\left(\frac{T}{1000}\right)^{-2}+G \quad (2.5)$$

$$C_p^o = A+B\cdot\left(\frac{T}{1000}\right)+C\cdot\left(\frac{T}{1000}\right)^2+D\cdot\left(\frac{T}{1000}\right)^3+E\cdot\left(\frac{T}{1000}\right)^{-2} \quad (2.6)$$

Another example is the **Antoine equation** that is used to estimate the saturation conditions analytically (see Equation 2.7). Similarly to the Shomate equation, a set of constant is used to calculate the saturation point at a given pressure (A, B, and C), alongside with the saturation temperature, $T_{sat}$. The equation is only valid within a certain temperature range, dependant on the fluid. Poling et al., 2001

$$log(p_{sat}) = A - B/(C+T_{sat}) \quad (2.7)$$

The **Lee-Kesler equation** (Equation 2.11) is another method to calculate the saturation conditions from a fluid of which the critical point is known. It makes use of the reduced pressure ($p_{red}$) and reduced temperature ($T_{red}$), which the pressure or temperature divided by those at the critical point respectively. Additionally, the Lee-Kesler equation uses the acentric factor ($\omega$), defined in Equation 2.10, as an input. The acentric factor is an expression for how non-spherical the molecule of a fluid is. (B. I. Lee and Kesler, 1975)

$$p_{red} = p/p_{crit} \quad (2.8)$$

$$T_{red} = T/T_{crit} \quad (2.9)$$

$$\omega = -log(p_{red,sat}) - 1, at T_{red} = 0.7 \quad (2.10)$$

$$ln(P_{red}) = f^{(0)} + \omega \cdot f^{(1)} \tag{2.11}$$

$$f^{(0)} = 5.92714 - 6.09648/T_{red} - 1.28862 \cdot ln(T_{red}) + 0.169347 \cdot T_{red}^{6}$$

$$f^{(1)} = 15.2518 - 15.6875/T_{red} - 13.4721 \cdot ln(T_{red}) + 0.43577 \cdot T_{red}^{6}$$

An often used equation of state that calculates the compressibility factor of a fluid is the virial equation (Equation 2.12). It makes use of empirically determined coefficients (A, B, C, D, ...), which are a function of temperature only.

$$Z = 1 + B \cdot \rho + C \cdot \rho^2 + D \cdot \rho^3 + ... \tag{2.12}$$

Apart from the aforementioned equations, there have been many semi-empirical relations developed throughout history to estimate the saturation conditions of fluids, such as the Arden-Buck, Tetens, or Goff-Gratch equations for example. These equations are not covered in this study, because these are used for the saturation properties of water.

## 2.1. Fluid properties of relevant cryogenic fluids

This thesis study focuses on the cooling of hydrogen to liquid conditions. Figure 2.1 shows that only helium has a boiling point lower than that of hydrogen. Therefore helium is the most logical choice for a cooling fluid for liquid hydrogen applications. The fluid properties of helium and hydrogen are presented and discussed in subsection 2.1.1 and subsection 2.1.2. These fluid properties all originate from the available online webbook of the National Institute of Standards and Technology (NIST).

### 2.1.1. Hydrogen fluid properties

In this document, hydrogen is referred to as the diatomic molecule $H_2$, while $H$ is referred to as atomic hydrogen. The fluid properties were retrieved from the NIST chemistry webbook (Linstrom and Mallard, 2023).

At ambient conditions, hydrogen is gaseous and has a density of 0.0852 kg/m³ (Linstrom and Mallard, 2023), which is significantly lower than the density of typical hydrocarbon fuels, having a density in the order of 800 kg/m³. This low density is one of the major challenges associated with hydrogen. Several solutions to store hydrogen at higher densities have been studied over the years, both for spacecraft and aircraft applications, such as for example high-pressure hydrogen, cryogenic (liquid) hydrogen, slush hydrogen, or a high-pressure liquid hydrogen. Slush hydrogen is a mixture of liquid and solid hydrogen, typically at lower temperatures than most liquid hydrogen applications, that offers an increased density compared to liquid hydrogen. (Friedlander et al., 1991) Figure 2.2 shows three regions of interest where hydrogen is stored with increased density (slush hydrogen not included). This study focuses on region 1, where hydrogen is stored in a liquid phase at sub-critical pressures, allowing for densities in the order of 70 kg/m³ (Linstrom and Mallard, 2023), less than 10% of typical hydrocarbon fuels.

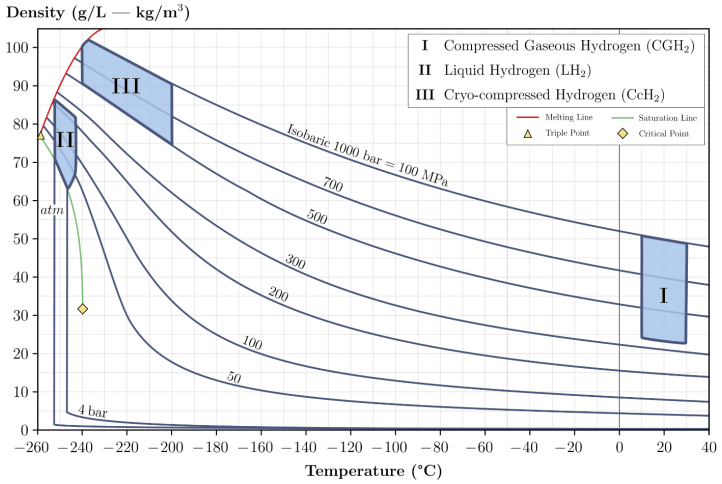


Figure 2.2: Hydrogen density as function of pressure and temperature. Three areas of interest for increased hydrogen density are highlighted. (Vidas et al., 2022)

Hydrogen has a critical point temperature of 33.18 K and pressure of 13 bar. At temperatures and pressures above these values, there is no distinct phase difference and the fluid is considered supercritical. At a temperature of 13.95 K and a pressure of 0.0721 bar, hydrogen exists in three states simultaneously, which is called the triple point. This point also indicates the lowest pressure and temperature at which hydrogen can exist in a liquid state. The phase diagram of hydrogen can be seen in Figure 2.3.

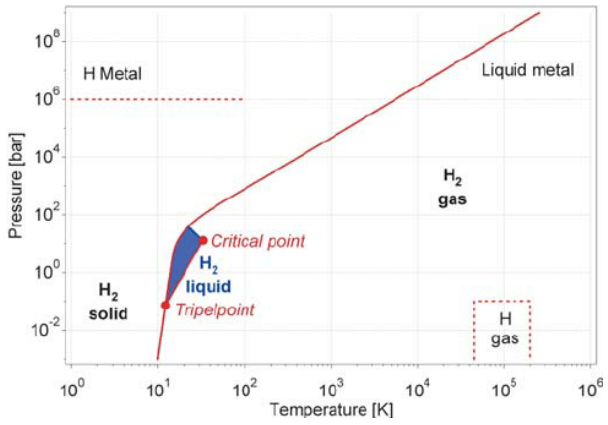


Figure 2.3: Phase diagram of hydrogen (Vidas et al., 2022)

Data from the NIST fluid property database can be can be used to compare the fluid properties at different pressures and temperatures. All fluid properties mentioned in this section originate from the NIST database, except when mentioned otherwise. (Linstrom and Mallard, 2023)

The compressibility factor, Z is used to assess when the ideal gas law can be used to calculate fluid properties of hydrogen. Table 2.2 shows the temperatures at which the compressibility factor has a certain value, e.g. 90%, for different pressures. Weather or not the ideal gas law can be used, is dependant on the application. For example, if an application only tolerates a deviation less than 1% from the ideal gas law, it is fair to use the ideal gas law down to temperatures of 47.7 K, at 1 bar pressure. If lower temperatures have to be included in that model, then the non-ideal gas effects should be taken into account, for example by using the compressibility factor or fluid property tables. At ambient temperatures, the compressibility factor increases with increasing pressure, although only with very small amounts. A plot of the compressibility factor factor as function of temperature and pressure can be found in Figure 2.4. The Boyle temperature, at which the compressibility factor is nearly identical for

different pressures, has been measured to be between 100 K and 110 K for hydrogen. Estrada-Torres, 2007

| | **0.5 bar** | **1 bar** | **3 bar** | **5 bar** | **10 bar** | **20 bar** |
|---|---|---|---|---|---|---|
| **101.0%** | None | None | None | None | None | 138.7 K |
| **99.9%** | 99.6 K | 101.9 K | 104.7 K | 104.9 K | 104.7 K | 103.0 K |
| **99.0%** | 37.4 K | 47.7 K | 67.3 K | 74.9 K | 84.8 K | 91.2 K |
| **90.0%** | 18.2 K* | 20.3 K* | 31.43 K | 37.1 K | 47.0 K | 57.3 K |
| **50.0%** | 18.2 K* | 20.3 K* | 24.7 K* | 27.2 K* | 31.1 K* | 37.8 K |

Table 2.2: Temperatures at which the compressibility factor of hydrogen equals 101% 99.9%, 99%, 90% and 50%, for different pressure values (in the 2.8 K to 1000 K range). *Saturated conditions

At temperatures below roughly 100 K, the effect of pressure on the fluid properties of hydrogen is noticeable. This is a consequence of the proximity to the critical point of the fluid and cryogenic temperatures. Figure 2.7, Figure 2.8, and Figure 2.9 show the change of specific heat at constant pressure ($C_p$), specific gas constant ($R$), and specific heat ratio ($\gamma$) as function of pressure and temperature. All three of these parameters show nearly asymptotic behaviour when approaching the critical point of hydrogen, being located at $T_{crit}$ = 33.14 K and $p_{crit}$ = 12.96 bar. (Linstrom and Mallard, 2023) At pressures below the critical point, these fluid properties will experience a discontinuity at the saturation temperature, caused by the transition from vapour to liquid. Another observation that can be made, is that the specific heat at constant pressure doesn't approach a horizontal asymptotic at high temperatures, but instead maintains a non-linear behaviour. There is however a region between about 400 K and 700 K, where $C_p$ only changes less than 1%.

Figure 2.5 shows the change of the Joule-Thomson coefficient with pressure and temperature. The Joule-Thomson coefficient of hydrogen is negative at ambient conditions, resulting in a temperature rise when the pressure decreases. It is one of three elements of the periodic table that doesn't have a positive JT coefficient at ambient conditions. The upper inversion temperature, above which no inversion can take place is 224 K. The peak of the inversion curve lies at a pressure of 117 bar. Above this pressure, the JT coefficient is always negative, hence a throttling expansion will only increase the temperature.

In Figure 2.6, the thermal conductivity of hydrogen is plotted as function of temperature and pressure. At a pressure of 1 bar, the heat conductivity of hydrogen has a value of 0.181 W/mK at room temperature and drops with about a magnitude when decreasing to 20 K. When phase transition occurs, the thermal conductivity of the fluid rises rapidly to values close to 0.1 W/mK, in the liquid state. Supercritical hydrogen will not drop to as low thermal conductivity values as subcritical hydrogen. For example, at a pressure of 30 bar, the thermal conductivity has a minimum value of 0.0566 W/mK. (Linstrom and Mallard, 2023)

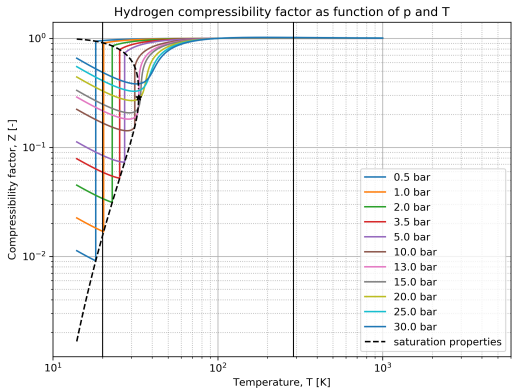


Figure 2.4: Hydrogen compressibility factor, Z, as function of temperature, for different pressures.

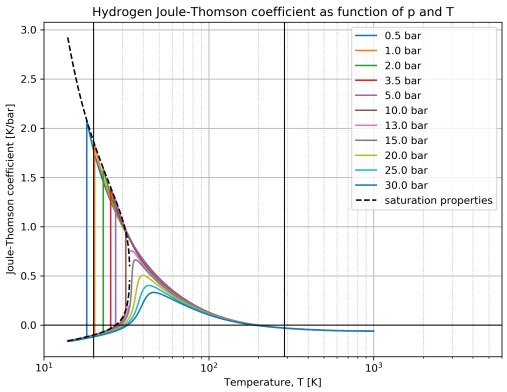


Figure 2.5: Hydrogen Joule-Thomson coefficient as function of temperature, for different pressures.

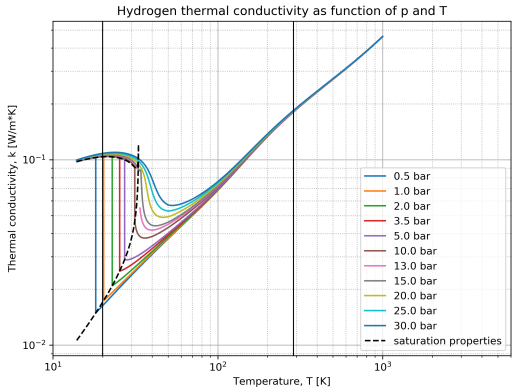


Figure 2.6: Hydrogen heat conductivity as function of temperature, for different pressures.

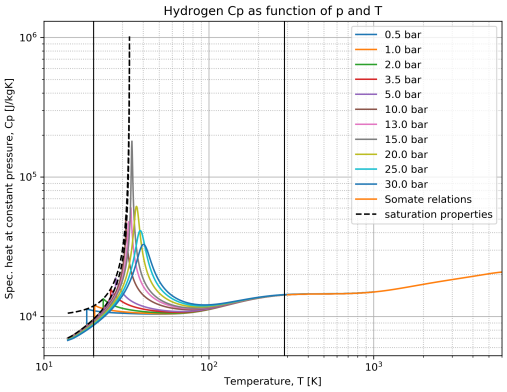


Figure 2.7: Hydrogen specific heat at constant pressure as function of temperature, for different pressures.

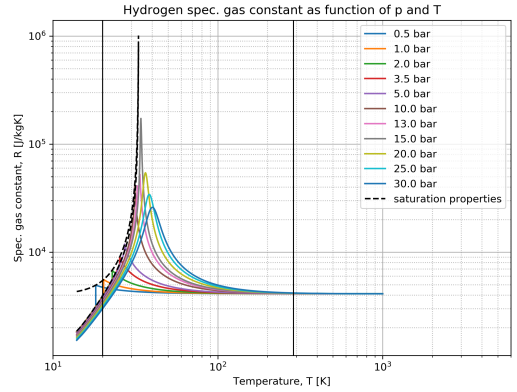


Figure 2.8: Hydrogen specific heat constant as function of temperature, for different pressures.

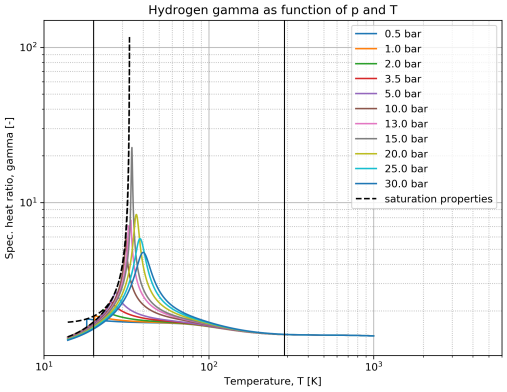


Figure 2.9: Hydrogen specific heat ratio as function of temperature, for different pressures.

### 2.1.2. Helium-4 fluid properties

Helium is a mono-atomic molecule that can exist as one of two stable isotopes: helium-3 ($^3He$) or helium-4 ($^4He$), of which the latter is most abundant on Earth and most commonly used for cryocooler applications. For this reason, this chapter primarily focuses on the use of helium-4.

Helium-4 is a gas with a density of 0.169 kg/m³ at ambient conditions and has a saturation point of 4.22 K at atmospheric pressure. This low boiling point makes helium a practical working fluid for cryocoolers at low cryogenic temperatures, especially below the boiling point of hydrogen. Additionally, helium is a noble gas, meaning that it doesn't have the tendency to chemically react with other substances.

Helium-4 has a critical point with a temperature of 5.20 K and pressure of 2.28 bar. Unlike most elements, helium-4 has no triple point. At temperatures below 2.17 K, it transitions to a partial superfluid instead of a solid. At this superfluid state, the fluid has zero viscosity and an extremely large thermal conductivity. At pressures above 25 bar, helium-4 can however form a solid. The transition from liquid to superfluid state is called the lambda point. The phase diagram of helium-4 and helium-3 are shown in Figure 2.10 and Figure 2.11.

| | **0.5 bar** | **1 bar** | **3 bar** | **5 bar** | **10 bar** | **20 bar** |
|---|---|---|---|---|---|---|
| **101.0%** | None | None | None | 56.5 K | 148.1 K | 288.3 K |
| **99.9%** | 19.5 K | 21.2 K | 22.1 K | 22.1 K | 21.3 K | 17.9 K |
| **99%** | 11.4 K | 13.9 K | 18.0 K | 19.0 K | 19.6 K | 16.9 K |
| **90%** | 4.64 K | 6.22 K | 9.84 K | 11.1 K | 12.9 K | 11.2 K |

Table 2.3: Temperatures at which the compressibility factor of helium equals 101%, 99.9%, 99%, and 90%, for different pressure values (in the 2.8 K to 1000 K range). *Saturated conditions

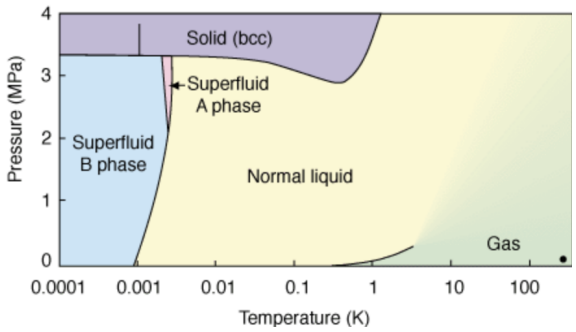


Figure 2.10: Phase diagram of helium-3 (LTL, 2003)

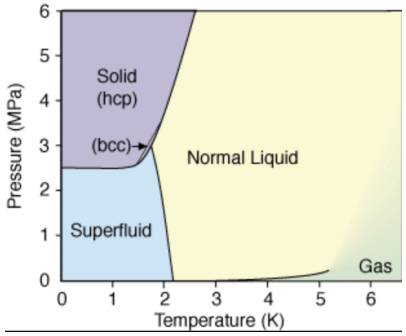


Figure 2.11: Phase diagram of helium-4 (LTL, 2003)

The heat capacity at constant pressure $C_p$, specific heat constant ($R$) and specific heat ratio ($\gamma$) of helium-4 all have an asymptotic behaviour at temperatures above 40 K, where temperature and pressure have little effect on their values. They converge to a constant value of 5193 J/kgK, 2077 J/kgK, and 1.666 respectively.

The Joule-Thomson coefficient of Helium-4 is positive at ambient conditions, meaning that a decrease in pressure will increase the temperature, during an isenthalpic throttling process. The maximum inversion temperature of helium is 45.4 K, meaning that the JT coefficient will always be negative above this temperature. The maximum pressure at which inversion can take place, is 37.0 bar, with a corresponding temperature of 20.7 K. Figure 2.13 shows the JT data from the NIST database as function of temperature and pressure.

Thermal conductivity of helium-4 at ambient conditions is 0.15 W/mK. Similar to most fluids, it decreases with decreasing temperature, as can be seen in Figure 2.14. Near the critical point, the thermal conductivity has an inflexion point, but decreases again at lower temperatures, either as a liquid or as a compressible liquid (subcritical).

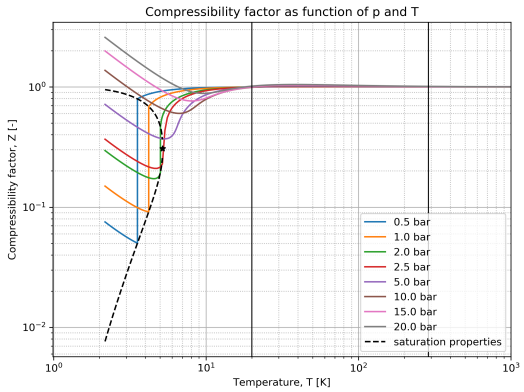


Figure 2.12: Helium compressibility factor, Z, as function of temperature, for different pressures.

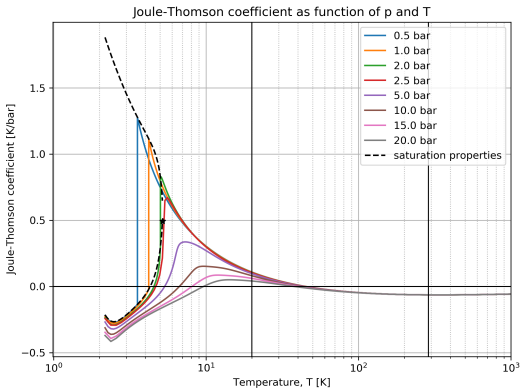


Figure 2.13: Helium Joule-Thomson coefficient as function of temperature, for different pressures.

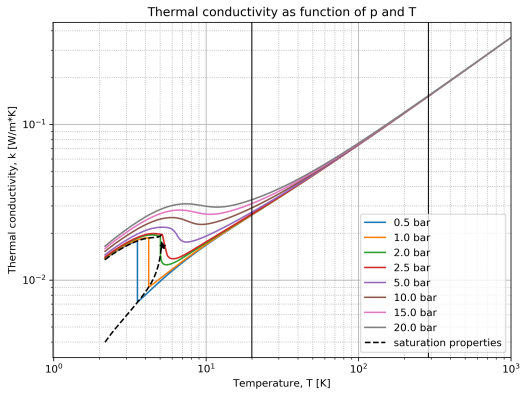


Figure 2.14: Helium heat conductivity as function of temperature, for different pressures.

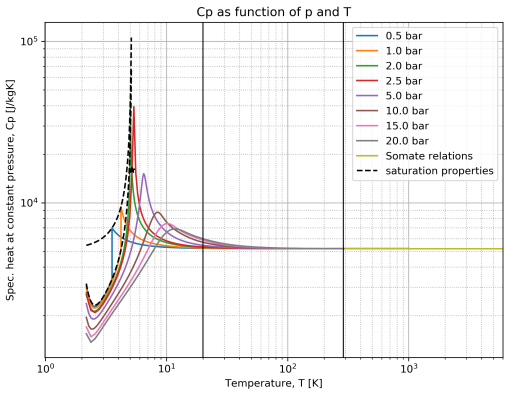


Figure 2.15: Helium specific heat at constant pressure as function of temperature, for different pressures.

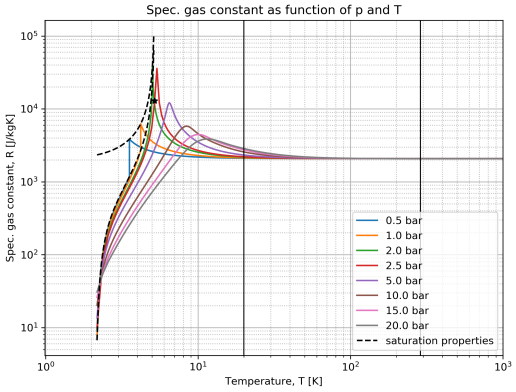


Figure 2.16: Helium specific heat constant as function of temperature, for different pressures.

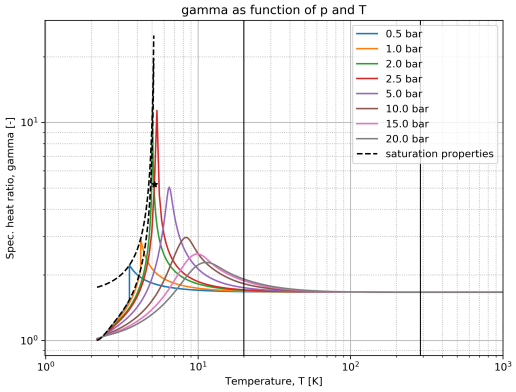


Figure 2.17: Helium specific heat ratio as function of temperature, for different pressures.

# 3

# Cryocoolers

## 3.1. Types of cryogenic coolers

There is a range of different types of cryocoolers that are used to achieve cryogenic temperatures, each with their own thermodynamic cycle. section 3.1 covers the working principles, characteristics and relevant application range these can operate in. Several coolers use the cyclic linear motion of a fluid inside a tube to displace heat from one end to another: the Stirling, pulse-tube, and Gifford-McMahon coolers, covered in subsection 3.1.1, subsection 3.1.2, and subsection 3.1.3 respectively. Several continuous cycles are covered in this section: the Joule-Thomson cooler in subsection 3.1.4, the sorption cooler in subsection 3.1.5, and the reverse turbo-Brayton cooler in subsection 3.1.6. Several solid state and sub-Kelvin coolers are briefly mentioned in this chapter: Peltier cooling, dilution cooling, adiabatic demagnetisation, and optical cooling. Although their relevance towards the study of liquid hydrogen cooling is minimal, they are described briefly for completeness.

### 3.1.1. Stirling cooler

Stirling coolers operate by periodically compressing and expanding a fixed amount of fluid by using a piston. Additionally, there is a displacer or regenerator present that dictates where the fluid is at any point during the cycle. This displacer makes sure that the fluid is at the load interface of the cooler when the fluid is cold and that it is at the heat rejection interface when the fluid is hot. An ideal Stirling cooler cycle consists out of four phases: an isothermal compression, isochoric heat rejection, isothermal expansion, and finally an isochoric heat absorption.

Because the piston and displacer are often controlled by a rotating flywheel or a linear spring system, the real thermodynamic processes are not perfectly isothermal or isochoric. On a T-s diagram, an ideal Stirling cycle has four distinct lines, indicating the isothermal and isochoric processes, while a real cycle has a more continuous and round shape.

Typically, single stage Stirling coolers are used up to temperatures of 60 K to 80 K and two stage coolers to temperatures of 15 K to 30 K. Stirling coolers either make use of linear motors or rotary drives to drive the compression piston. Configurations of two drive motors are not uncommon, especially for space applications, to limit the vibrations or momentum transfer to the vehicle. (Radebaugh, 2009)

### 3.1.2. Pulse-tube cooler

Pulse-tube coolers operate with a similar thermodynamic cycle compared to Stirling coolers. However instead of using a displacer, a pulse-tube cooler makes use of a precisely tuned pneumatic circuit that relies on the fluid equivalent of an electrical resistance-inductance-capacitance together with a regenerator to control the fluid and temperature distribution. This is achieved by inclusion of an inertance tube, regenerator, and reservoir volume. This eliminates the moving parts at the cold end of the cooler and reduces the vibrations of the cooler, compared to a Stirling-type cooler. Pulse-tube coolers typically have lower thermodynamic efficiencies than Stirling coolers. Similarly to the Stirling cooler (and other reciprocating cooling cycles in general), achieving low temperatures is difficult due to the reduced

thermal capacity of regenerator materials at low temperatures. This reduced thermal capacity matches poorly in combination with the high operating frequencies of these coolers, typically between 30 Hz and 70 Hz. (Radebaugh, 2009)


Figure 3.1: Stirling cryocooler by CryoTel, 2023

Figure 3.2: Pulse-tube cryocooler by Mullie et al., 2016

### 3.1.3. Gifford-McMahon (GM) cooler

Gifford-McMahon coolers operate similarly to Stirling coolers, where a displacer or regenerator determines whether the fluid interacts with the hot end or cold end at each point in the cycle. The compressor architecture is however different from that of a Stirling or pulse-tube cooler. Instead of using a piston, a rotary valve alternately supplies the pulsating tube with a high or low pressure fluid. After the high pressure flow is allowed to expand, it cools the load interface. Thereafter it is discharged and transformed to a hot, high pressure fluid by means of a continuous flow compressor. After compression and heat rejection of the fluid, the flow is again allowed to expand via the rotatry valve. The use of a rotary valve allows the GM cooler to operate at lower operating frequencies in the order of 1 Hz to 2.4 Hz. This counteracts the issues arising from the low thermal capacity of the regenerator materials at low cryogenic temperatures and thus allows GM coolers to operate more effectively at lower temperatures compared to Stirling coolers. (Radebaugh, 2009)

Figure 3.3: Gifford-McMahon cryocooler by Cryomech, 2023

### 3.1.4. Joule-Thomson (JT) cooler

As the name implies, Joule-Thomson coolers make use of the Joule-Thomson throttling effect to cool fluids to cryogenic temperatures. The ideal thermodynamic cycle consists of an isentropic compression by a compressor, followed by an isobaric heat rejection, after which an isenthalpic JT throttling process takes place, and finally an isobaric heat absorption at the load interface of the cooler. In contrast to the pulse-tube, Stirling, and Gifford McMahon coolers, the JT cooler uses a continuous cycle, which allows for the use of fluid pipes for remote cooling.

Figure 3.4: Joule-Thomson cryocooler by LeTehnica, 2023

The isenthalpic throttling process is achieved by forcing the working fluid through a porous plug or valve by creating a significant pressure difference. The pressure difference and the temperature of the fluid determine the decrease in temperature during the JT throttling process, as explained in chapter 2. One of the major advantages of JT coolers is that they don't have any moving parts at the cold end and that they cool in a continuous cycle. The thermodynamic efficiency of these coolers is typically lower than that of previously mentioned cooler types, because the isenthalpic process is irreversible. Because the JT coolers only operate at low-enough temperature for the JT effect to take place, they need a recuperator or a first stage cryocooler to reduce the working fluid's temperature. Either of these ensure that the fluid at the throttle is sufficiently cold for the JT effect to result in a decrease in temperature. For this reason, JT coolers are often used in combination with a Stirling cooler that pre-cools the fluid more efficiently. (Radebaugh, 2009)

### 3.1.5. Sorption cooler

Sorption coolers operate similarly to Joule-Thomson coolers, with the main difference that they make use of sorption beds and check valves to increase the pressure and temperature of a cold, low pressure gas. These sorption beds are typically made out of a porous structure and work either by chemical or by physical sorption, controlled by the supply of heat towards the bed. The main advantage for these coolers is that there are no moving components, and hence minimal or no vibrations. In terms of efficiency, it suffers from the same issue as the JT cooler, whereby the isenthalpic throttling process to cool the fluid is a non-reversible process, reducing the overall efficiency of the cooler. (Jones et al., 1990)

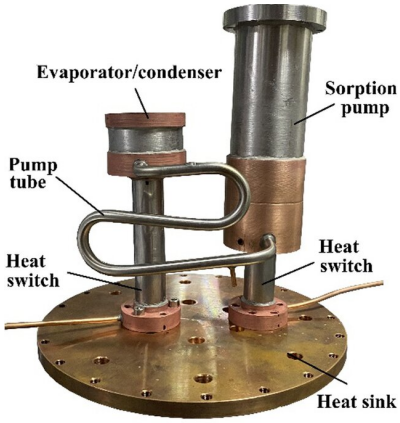


Figure 3.5: Sorption cryocooler by LeTehnica, 2022

### 3.1.6. Reverse Turbo-Brayton Cooler (RTBC)

Similarly to the common Turbo-Brayton cycle, the RTBC makes use of the compression and expansion process using turbomachinery to change the fluid's pressure and temperature. After a compressor raises the pressure and temperature of the fluid during an isentropic process, the fluid is cooled down by isobaric heat rejection to the environment. Thereafter, the fluid temperature is further reduced by an isentropic expansion through a turbine, followed by the isobaric heat absorption at the load interface. Finally the fluid flows back to the compressor. A major advantage of the RTBC is that it is a continuous cycle that can have the cold load interface at a further distance from the hot end by using pipes. This makes it a compelling choice to be used for the cooling of large fuel tanks or remote devices. Because the RTBC uses a continuous cycle, a counter-flow recuperator is typically used instead of a regenerator to reduce the required pressure ratio to achieve a minimum temperature. (Radebaugh, 2009)

Due to the use of non-contact bearings, RTBCs typically exhibit very little vibrations. The performance of RTBCs has proven to be relatively high, especially for devices operating at higher power levels, as explained in section 3.3. RTBCs are not so common as reciprocating cryocoolers, however there is currently an increase in the development effort towards these type of coolers. One of the larger challenges of developing small-scale RTBCs is the difficulty of manufacturing the turbomachinery components.

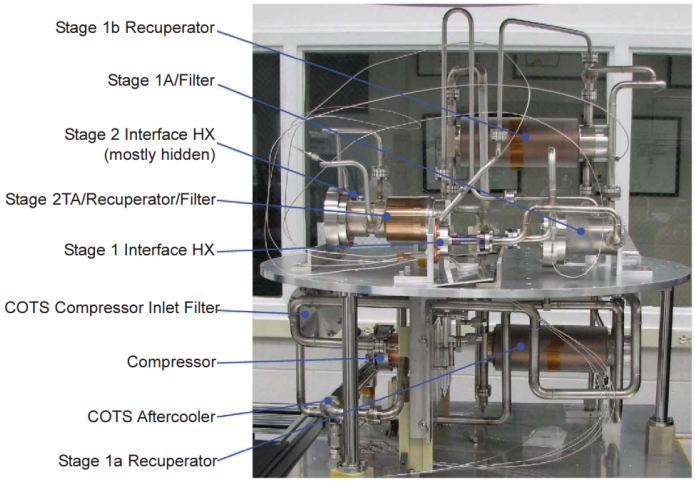


Figure 3.6: 2-stage reverse turbo-Brayton cryocooler by M. Zagarola et al., 2009

### 3.1.7. Peltier cooler

Peltier coolers are solid-state devices that, similarly to thermocouples, rely on the reverse Seebeck effect (also called Peltier effect) to generate a temperature difference. Two metals with different electrical and thermal conductive properties will experience a temperature gradient when a current is applied, similarly to the reverse effect in thermocouples where a temperature difference can be measured using the induced voltage difference over the two metals. This thermo-electric behaviour allows for Peltier coolers to be used for applications typically higher than cryogenic temperatures. Peltier coolers have low coefficients of performance, however are often used because of their lack of moving parts or vibrations, making them reliable. (Stockholm, 1997)

Figure 3.7: Three-layer stack of Peltier coolers by Stockholm, 1997.

### 3.1.8. Optical cooler

Optical or laser cooling is, similarly to Peltier coolers, a solid state cooler with little to no moving parts. A gas or a solid substance, typically doped in ytterbium, is subjected to a laser beam, which exerts a force on the molecules in the form of radiation pressure. The laser is tuned such that the target molecules only experience this force when moving towards the laser. This is achieved by exploiting the Doppler frequency shift, caused by the vibrations or translational motion of the individual molecules. In such a manner, the atoms will experience different wavelengths of light depending on the direction of their motion and only absorb the photons when moving towards the laser, hence reducing their thermal energy. The photons are later emitted by the atoms by means of fluorescence, however in a random direction, resulting in a net force. Careful selection of the laser light frequency, in combination with the subject element, is essential for the cooling process to take place. This type of cooling is typically limited to the warmer end of the cryogenic temperatures or above. (Melgaard et al., 2016)

### 3.1.9. Adiabatic demagnetisation cooler (ADC)

Figure 3.8: Adiabatic demagnetisation cooler with dilution cooler by Duband et al., 2012

ADCs make use of paramagnetic substances, called a salt pill, that exhibit molecules with large internal magnetic fields. By imposing an external magnetic field to the salt pill, the internal magnetic fields all align. Reducing the strength of this external magnetic field, allows the thermal energy of the substance to be converted towards the internal magnetic field of the molecules, and by such lowering the overall temperature. This process only lasts until the external magnetic field cannot be lowered further, after which the salt pill's temperature is raised by imposing a larger external magnetic field than before. Thereafter, the heat is rejected towards a heat sink that already operates at cryogenic temperatures, for example a liquid helium bath. (Kimball, 2014)

This periodic cooling cycle is used to cool components to temperatures below 1 K, where most mechanical cycles fail to operate. This type of cooler is however not considered relevant for the future scope of this study.

### 3.1.10. Dilution cooler

Dilution coolers rely on the endothermic process of diluting a mixture of the two most common helium isotopes: helium-3 and helium-4. A liquid helium bath below 1 K contains a nearly pure helium-3 zone and a diluted zone, consisting primarily of helium-4. Helium-3 molecules migrate from the $^3He$ rich to the diluted zone. This dilution is an endothermic process and is the driving mechanism that provides the useful cooling power of the cooler. The Helium-3 molecules are continuously extracted from the diluted zone in a still, after which the cycle is repeated. $^3He$-$^4He$ dilution coolers can operate in the milliKelvin temperature range, however need an additional cooler to maintain the liquid helium bath. (Martin et al., 2010)

Figure 3.9: Helium dilution cooler (Martin et al., 2010)

## 3.2. Applications of cryocoolers

Cryocoolers have been used for various applications, in a wide range of fields. This section aims to provide a global overview of the typical aerospace applications of cryogenic coolers. subsection 3.2.2 and subsection 3.2.1 treat the aircraft and space applications of cryocoolers respectively, while subsection 3.2.3 briefly mentions which non-aerospace applications exist. Because the scope of this study is zero boil-off for liquid hydrogen tanks, the content of this section has an emphasis on non-reciprocating cooling cycles such as the reverse turbo-Brayton cycle.

In summary, cryogenics for space applications has had a relatively long heritage, where passive systems and solid coolant cryostats cover the majority of designs. Active coolers have been operated for space missions with a longer lifetime, mainly the Stirling and Joule-Thomson types. The use of RTBCs has been limited to 1 case, however there it is currently being considered for ZBO of cryogenic propellants in space. The use of cryogenics for aircraft applications has been much more limited, where to the author's knowledge no active cryocooler has been used to achieve zero boil-off for airborne cryogenic fuel tanks.

### 3.2.1. Space applications

Cryocoolers have been used for for many decades on space missions, primarily to cool optical instruments for observational satellites. (Collaudin and Rando, 2000) An overview of the typically used cryocoolers on space applications as function the operational cold-end temperature is shown in Figure 3.10. It is clear that the cooling power of the applications tend to be lower at lower temperatures, which can be identified as a consequence of the limited power available on a spacecraft in combination with the lower coefficient of performance (see section 3.3) at lower temperatures.

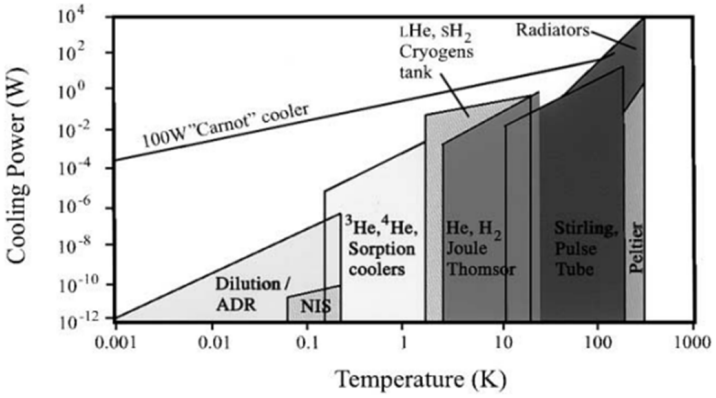


Figure 3.10: Typical operational regime, in terms of temperature and cooling power, of different types of cryocoolers for space applications. (Collaudin and Rando, 2000)

Most cryogenic cooling for space applications happens through a combination of passive thermal control of the spacecraft, in combination with a local active cooling system that reduces the temperature of a specific component to the target temperature. The choice for frequent use of passive cooling systems onboard spacecraft can be attributed to the lack of induced vibrations and the lack of any form of heat transfer with the environment except radiation. Next to passive systems, open cycle coolant loops have been employed on spacecraft, where a pre-cooled substance (often a solid) acts as a coolant until fully consumed. The limited amount of coolant is stored in a well-insulated container to extend its lifetime as long as possible. Some examples mentioned by Collaudin and Rando, 2000 are the use of solid $N_2$, solid $Ne$, solid $H_2$, supercritical $^4He$, and superfluid $^4He$ (ordered decreasingly with temperature).

Apart from passive systems or cryostats, the Stirling-type cooler has been the most frequently used active cooler for space applications. However, the use of pulse-tube coolers for space applications has recently been considered for its potential to reduce on-board vibrations. (Collaudin and Rando, 2000) Only few continuous cycle cryocoolers have been operated in space, of which the most popular has been the Joule-Thomson cooler type. The NICMOS cooler onboard the Hubble space telescope was the first use of an RTBC in space and has been operating successfully since its installment in 1997. In recent decades, the use of RTBCs as a mean to achieve zero boil-off on long-duration space missions with cryogenic propellants has been studied and considered by multiple organizations and research institutes such as NASA (Hastings et al., 2002, Deserranno et al., 2014) and ESA (ESA, 2017). Other non-reciprocating cryocoolers in space have been flown as experiments onboard NASA's Space Shuttle, such as the BETSCE experiment by NASA that featured a vibration-free hydrogen sorption cooler in 1996. (Bowman, 1997)

Because the heat rejection for space applications primarily occurs through radiation, it is important to understand the functioning of radiators in space. These are designed to radiate the excess heat of the cryocooler (or other components) away from the spacecraft. The use of large radiators however poses constraints on the attitude control system of the spacecraft, as the radiator should not be illuminated by the sun, or Earth in some cases, to avoid receiving heat instead of rejecting. When radiating towards deep space, a reference temperature of 2.73 K is generally used. (Collaudin and Rando, 2000)

Typically space radiators radiate heat at a temperature close to 300 K, similar to the spacecraft bus's temperature. There has however been an effort towards the development of cryoradiators that reject heat at lower temperatures. Because the radiative heat flux is a function of temperature to the power of four, the effective area needed to transfer the same amount of heat in a cryoradiator can much larger than in case of a regular radiator, as shown in Figure 3.11. Cryoradiators that operate below 100 K have been made, however the parasitic heat loads associated with thermal conduction from the spacecraft bus become a dominant source of performance loss. For this reason it has been found to be impractical to use cryoradiators at temperatures below 60 K. (Collaudin and Rando, 2000) Regardless, a few cryoradiators have been deployed that operate below 60 K, for example those onboard the James Webb Space Telescope, called the Fixed IMIR Radiators (FIR), which operated between 35 K and 40 K, as described by Franck et al., 2016. Even with minimal parasitic heat load, these radiators can only remove about $1.1 \cdot 10^{-4}$ Watts per square meter.

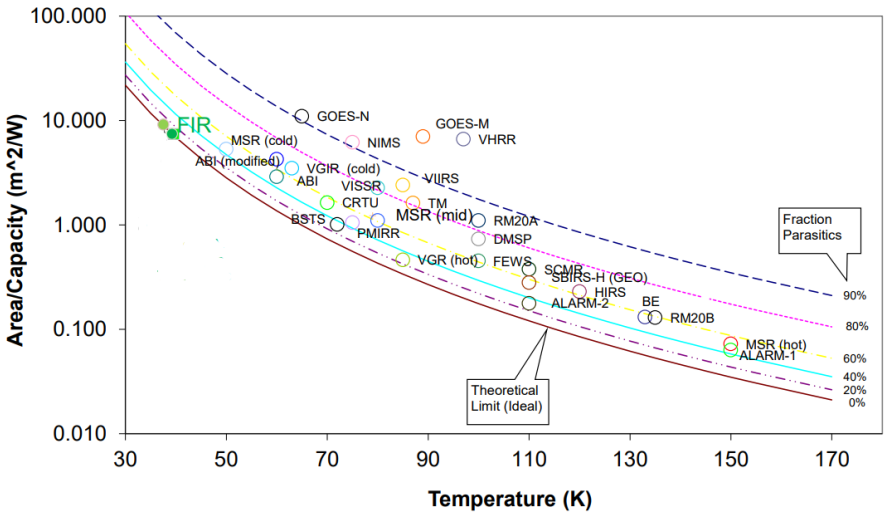


Figure 3.11: Theoretical and actual heat flux of several cryoradiators for space applications as function of the heat rejection temperature. (Franck et al., 2016)

### 3.2.2. Aircraft applications

The use of cryocoolers is more evident for space applications than that for aircraft, where typical mission durations are orders magnitude shorter and environmental losses significantly larger. Therefore, the use of cryocoolers onboard aircraft has been minimal and primarily limited to highly specific applications, often being related to military or scientific operations. For example, Creare developed an air separation device using a reverse turbo-Brayton cycle to generate pure oxygen for medical purposes and nitrogen for tank pressurization onboard a large transport aircraft. (J. J. Breedlove et al., 2008) Another example of the use of a cryocooler system onboard aircraft is the Stratospheric Observatory For Infrared Astronomy (SOFIA), where a commercial pulse-tube cooler was used to cool the optical instruments of the airborne telescope. (Rosner et al., 2016; Richards et al., 2020) These are however very exceptional cases, as typical commercial aircraft don't feature fluids at cryogenic temperatures.

Some experimental aircraft have already made use cryogenic propellants such as liquid hydrogen instead of conventional hydrocarbon fuels, such as a modified B-57 aircraft in the late '50s that intermittently used liquid hydrogen fuel as part of research project Bee. (NASA, 1978) Later in the late 1980s, the experimental Tu-155 aircraft was flown using both kerosene and liquid hydrogen. (Sosounov and Orlov, 1990) In recent years, there is an increased amount of studies towards the use of cryocoolers onboard aircraft to provide zero boil-off for cryogenic fuels such as liquid hydrogen or to achieve superconductivity in electric motors, both driven by the goal of sustainable and carbon-free aircraft transport in the future. For example, Berg et al., 2015 performed a conceptual study on the use of RTBCs for cooling superconducting motors and concluded that there is a need for more studies on cryogenic systems onboard aircraft in order to perform reliable trade-offs.

Therefore, the focus of this study is to contribute to the research on the technical feasibility of using a cryocooler to achieve zero boil-off for liquid hydrogen powered aircraft as there currently exists a very limited amount of research on this topic.

### 3.2.3. Non-aerospace applications

Although this study focuses on the use of cryocoolers for aerospace applications, it is important to aware of the use and characteristics of cryocoolers in other fields as a reference to what technologies have been developed and to what degree the current state of the art has matured. In the following paragraphs, several common ground-based applications of cryocoolers are highlighted. However due to the wide extend of cryogenic applications, this is only a very brief summary. For an in-depth overview of all cryogenic applications, the reader is referred to the book "Cryogenic Technology and Applications" from Jha, 2011.

Cryogenics have been used in a wide range of fields, from large-scale industrial liquefaction plants to small-scale portable coolers for infrared vision, or micro-Kelvin applications featuring fundamental research. Additionally, cryocoolers are involved in medical applications such as the use of superconductors in MRI machines for example. Furthermore, with the prospect of an energy transition, the increasing demand for liquefied natural gas (LNG) in recent decades has sparked a noticeable increase in the research towards more efficient liquefaction and storage methods. (Michot Foss, 2007) Figure 3.12 shows most cryogenic applications and their cooling power as function of the temperature. (Radebaugh, 2009) Cryocoolers for ground applications are typically not optimized for their mass but rather energy efficiency. Therefore, the use of very large heat exchangers or multi-stage coolers is not uncommon for industrial ground applications.

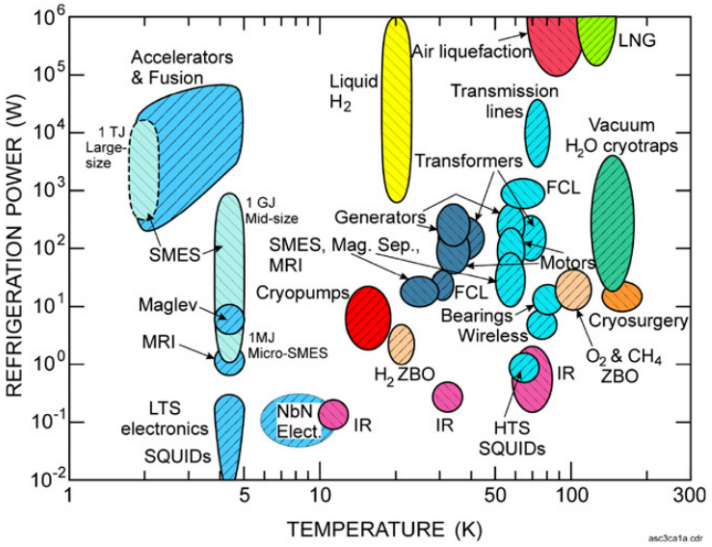


Figure 3.12: Cryocooler applications and their typical power consumption vs load temperature. (Radebaugh, 2009)

## 3.3. Performance of cryocoolers

When designing, optimising, or comparing cryocooler, there are several design parameters that used. Two parameters often referred to in literature are the coefficient of performance (COP) and percentage of Carnot efficiency. Another performance parameter is the specific power, which is an often used measure to relate the cooling power to the mass of the cooler. A description of these performance parameters is provided in subsection 3.3.1. Additionally, in subsection 3.3.2 a comparison of the typical performance parameters of commercially available cryocoolers is provided and discussed. For a more detailed description and breakdown of the performance parameters of reverse turbo-Brayton coolers, the reader is referred to section 4.4.

### 3.3.1. Performance parameters of cryocoolers

A common performance parameter for cryogenic coolers is the coefficient of performance (COP), which is a metric for the amount of useful heat that is extracted by the cooler divided by the input power provided to the cooler, as can be seen in Equation 3.1.

$$COP = \frac{\dot{Q}_{load}}{\dot{W}_{input}} \tag{3.1}$$

The maximum possible coefficient of performance that can be achieved by a cooler is the Carnot coefficient of performance ($COP_{Carnot}$). It is purely a function of the heat rejection temperature and cold end temperature of the cycle. For ground applications, a cryocooler's reject temperature is equal to or close to the ambient temperature.

$$COP_{Carnot} = \frac{T_{cold}}{T_{reject} - T_{cold}} \tag{3.2}$$

An often mentioned performance parameter is the Carnot efficiency ($\eta_{Carnot}$), which denotes how close the coefficient of performance of a cooler is compared to that of an ideal Carnot cycle.

$$\eta_{Carnot} = \frac{COP}{COP_{Carnot}} \tag{3.3}$$

The previously mentioned performance parameters primarily highlight the thermodynamic efficiency of the cryocooler. However another often-considered metric is the weight of the device which can be assessed using the specific power ($P_{sp}$).

$$P_{sp} = \frac{\dot{Q}_{load}}{m} \tag{3.4}$$

### 3.3.2. Comparison of cryocooler performance

The coefficient of performance of a cryocooler can be expressed as a function of the operating conditions of the cooler. Variables that are frequently mentioned in literature include: heat load, load temperature, cooling power, rejection temperature, and input power.

A study by Radebaugh, 2009 identified the state of the art cryocooler Carnot efficiency at 80 K to be around 20% for space applications and 10-15% for commercial cryocoolers. At temperatures of 3 K, where helium is liquid at ambient pressure, typical efficiency levels are around 1%.

Over the years, a few cryocooler surveys have been performed by multiple authors with the goal of creating useful correlations to estimation the specific power, efficiency, and/or cost of a cryocooler. For example, the often-cited survey by Strobridge, 1974 or the low-power cryocooler survey by ter Brake and Wiegerinck, 2002. The latter presented its results, overlayed on the data from Strobridge, which is shown in Figure 3.13.

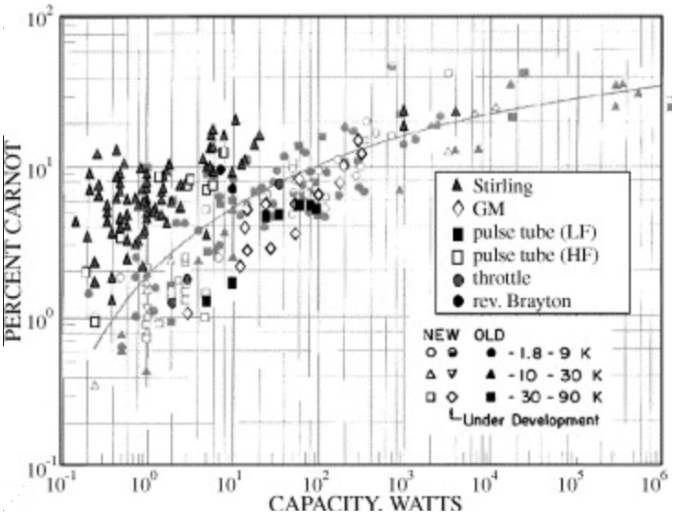


Figure 3.13: Cryocooler percentage of Carnot efficiency data vs input power, combined data from Strobridge, 1974 and ter Brake and Wiegerinck, 2002.

For the present study, a literature survey was performed to compile a database on commercially available cryocoolers. Firstly, the operating conditions of the different types of cryocoolers are identified by plotting the heat load as a function of the load temperature and input power, shown in Figure 3.14 and Figure 3.15 respectively. A distinction between five different types cryocoolers is made: Stirling,

pulse-tube, Gifford-McMahon, Joule-Thomson, and reverse turbo-Brayton coolers. This list contains a total of 210 cryocoolers, primarily consisting of commercially available and space flown cryocoolers. A majority of the coolers presented in this section are those developed by the following companies, although not only limited to these: Sunpower, Thales Cryogenics, AIM, Ricor, Cryomech, Sumitomo Heavy Industries, Raytheon, Ball Aerospace, Creare, and Lockheed Martin. This list is not a complete overview of every single cryogenic coolers ever developed, however it is deemed sufficient to create a general understanding of the applicable operational range of the different types of cryocoolers.

Most commercial cryocoolers don't have a single point of operation, but instead provide performance curves with the cooling power as function of the cooling temperatures and/or input power settings. When available, a data set of four values was taken from each cryocooler. These are represented in the graphs below by means of a line connecting the different data points. Often the so called zero-load temperature is also included, being the minimum temperature achievable by the cooler, at which no more useful cooling power can be provided. For several plots, these data points fall outside of the plot boundaries, due to the use of logarithmic axis scales.

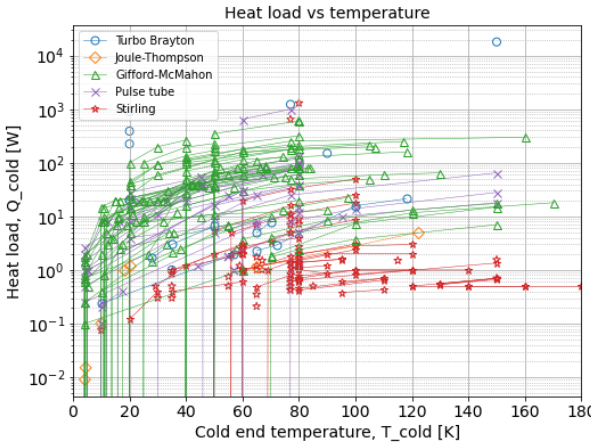


Figure 3.14: Cooling power as function of load temperature.

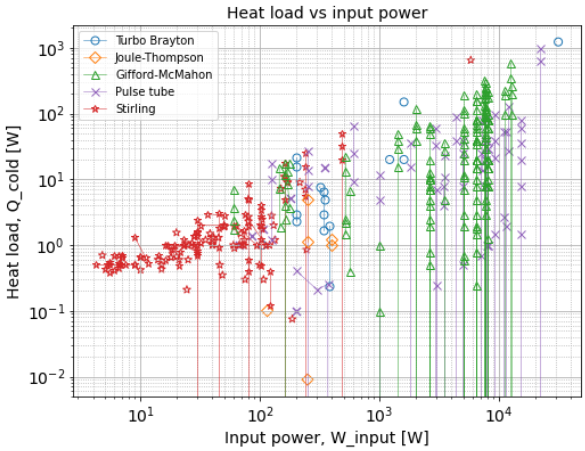


Figure 3.15: Cooling power as function of input power.

In Figure 3.14, it is shown that coolers operating at lower temperatures typically have lower cooling loads as well. This can be explained by the lower coefficient of performance at lower temperatures, as will be explained in more detail later in this section. The majority of the cryocoolers in this study have cooling powers between 0.2 W and 300 W. At temperatures of 20 K, close to the boiling point of hydrogen, currently existing commercial cryocoolers operate between 0.1 W and 40 W, with a few outliers of a higher cooling power. There is a noticeable amount of cryocoolers operating at temperatures between 77 K and 80 K, close to the boiling point of Nitrogen at atmospheric conditions. This can be attributed to the fact that the production of liquid Nitrogen or liquid air has a wide range of applications.

Figure 3.15 shows how the cryocooler heat load varies with the input power. It is clear that Stirling coolers are typically operated at input power of 200 W or less. JT coolers and RTBCs have been used for intermediate input power ranges between 100 W and 2000 W. Additionally, it was found that existing pulse-tube and GM coolers have been operating at a wide range of input power levels, typically above 100 W and below 20 kW.

Performance parameters, such as the COP, specific power and percentage of Carnot efficiency, can be expressed as function of the typical operating variables of a cryocooler: the heat load, load temperature, and input power. The performance variation associated with the rejection temperature is not covered, because nearly all compressors in the database have a rejection temperature between 273 K and 300 K.

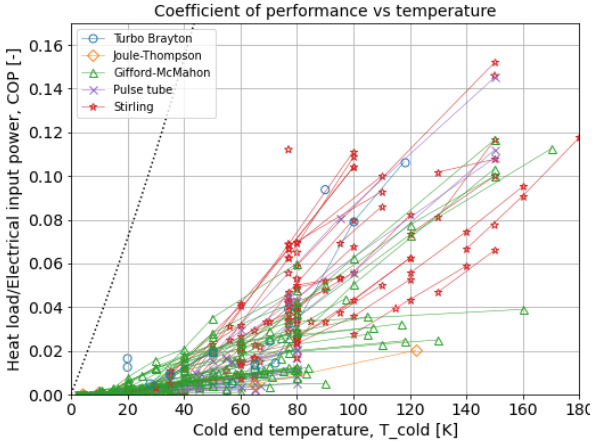


Figure 3.16: Coefficient of performance as function of load temperature.

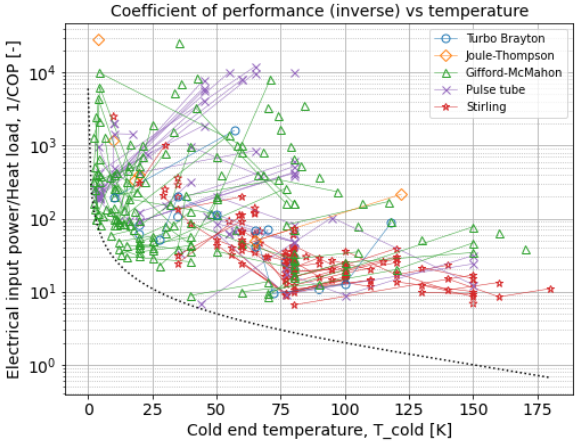


Figure 3.17: Inverse of the coefficient of performance as function of load temperature.

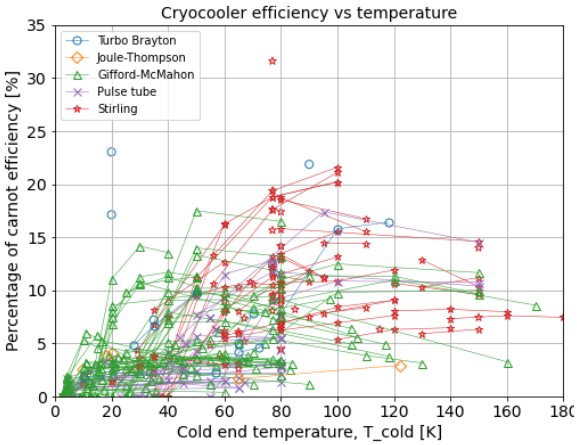


Figure 3.18: Coefficient of performance as function of load temperature.

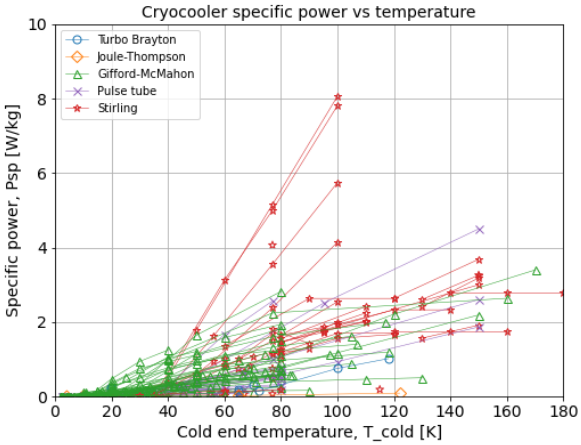


Figure 3.19: Specific power as function of load temperature.

The general trend that can be observed is that all performance parameters decrease as the load temperature decreases. Several cryocoolers have a local maximum percentage of Carnot efficiency because these are often optimised for operation at their design point, instead of a wider range of temperatures. The results agree well with those observed by Radebaugh, 2009, such as for example that the state of the art coefficient of performance of cryocoolers at 80 K is about 20%.

Stirling coolers tend to score best when it comes to COP, specific power, and percentage of Carnot efficiency. However only for temperatures above 40 K. Below this temperature, Gifford-McMahon coolers outperform Stirling coolers in terms of the three performance parameters mentioned earlier. This confirms what is mentioned in literature: that GM coolers can operate more efficiently at lower temperatures due to the lower operating frequency compared to Stirling coolers (see subsection 3.1.3).

Pulse tube coolers generally have lower performance parameters compared to Stirling coolers, and follow the same trend with significant performance loss at 40 K and below. The amount of reverse turbo-Brayotn or JT coolers is too low to identify clear performance trends, however RTBCs have proven to be capable of performing better than Stirling or GM coolers.

As shown in Figure 3.14, coolers that operate at lower temperatures, tend to operate with lower

cooling powers compared to those at higher temperatures. This correlation could also contribute to the fact that coolers at low temperatures have worse performance parameters, as shown in Figure 3.16, Figure 3.17,Figure 3.18, and Figure 3.19. In order to understand the influence of the cooling power on the performance parameters, independent from the cooling temperature, separate performance plots are created for different temperature ranges:

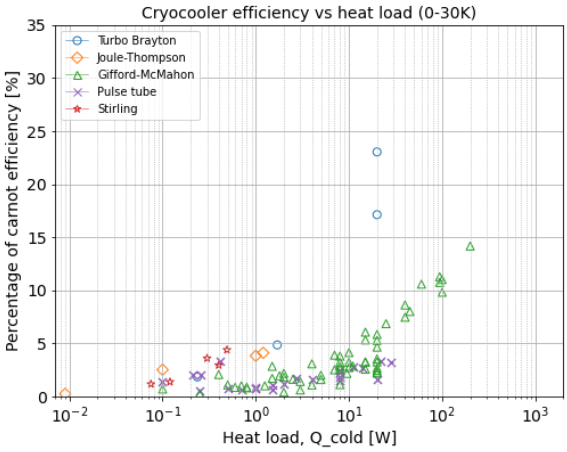


Figure 3.20: Percentage of Carnot efficiency as function of load temperature for a 0 K to 30 K temperature range.

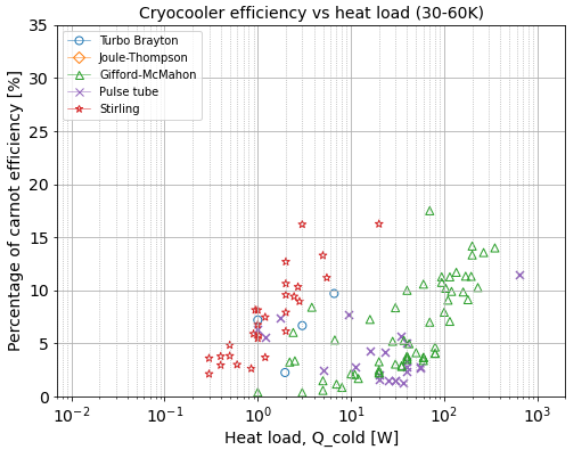


Figure 3.21: Percentage of Carnot efficiency as function of load temperature for a 30 K to 60 K temperature range.

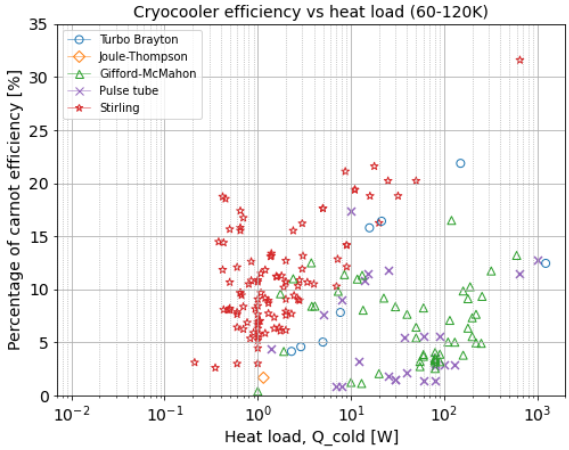


Figure 3.22: Percentage of Carnot efficiency as function of load temperature for a 60 K to 120 K temperature range.

All three plots show that there is a correlation between the percentage of Carnot efficiency and the heat load of the cooler, where lower heat loads result in lower percentages of Carnot efficiency.

For lower temperature ranges, below 30 K, the percentage of Carnot efficiency is mostly below 5%, apart from a few exceptions. The efficiencies of pulse-tube and GM coolers follow a nearly linear relation (exponential in the plot, caused by the logarithmic scale). Although only few data points are included, JT and Stirling coolers perform better than pulse-tube or GM coolers. The former two are generally restricted to low heat loads, below 2 W, for applications below 30 K. Although only very few data points are present, RTBCs show the potential to achieve much higher efficiencies at these low temperatures compared to the other types of coolers mentioned before.

For applications with load temperature between 30 K and 60 K, there is a stronger correlation between the percentage of Carnot efficiency and heat load. Stirling cooler's percentage of Carnot efficiency increases with roughly 10% for an increase in order of magnitude. For 30 K to 60 K applications, Stirling coolers have however been limited to heat loads below 6 W, with exceptions. Pulse-tube and GM coolers show a less distinct correlation between heat load and percentage of Carnot efficiency. The latter is typically lower than that of Stirling engines, however heat loads range from 1 W to over 100 W for 30 K to 60 K applications.

At temperatures above 60 K and below 120 K, percentage of Carnot efficiencies of Stirling coolers still increases with the heat load, however there is no distinct correlation between the performance of GM and pulse-tube coolers with the heat load. The percentage of Carnot efficiency for RTBCs in the 60 K to 120 K range is at the lower end of that of Stirling coolers, or at the higher end of GM or PT coolers.

| | **Low heat load (<1 W)** | **Intermediate heat load (1 W - 100 W)** | **High heat load ( >100 W )** |
|---|---|---|---|
| **Low T (0 K - 30 K)** | Stirling<br>JT<br>PT | RTBC<br>GM | |
| **Intermediate T (30 K - 60 K)** | Stirling | Stirling<br>GM<br>RTBC<br>PT | GM<br>PT |
| **High T (60 K - 120 K)** | Stirling | Stirling<br>RTBC<br>GM<br>PT | GM<br>PT |

Table 3.1: Overview of typical application range of different types of cryocoolers, based on current and past commercial devices: Stirlin, Joule-Thomson (JT), Pulse-Tube (PT), Gifford-McMahon, and reverse turbo-Brayton cryocoolers (RTBC). Cryocooler types with a higher percentage of Carnot efficiency are listed above those with a lower performance. Single outliers are not taken into account.

# 4

# Reverse Turbo-Brayton Cryocoolers (RTBC)

## 4.1. Thermodynamic cycle

A simplified, ideal cycle of an RTBC operates in four different steps: isentropic compression, isobaric heat rejection, isentropic expansion, and isobaric heat absorption. As the name implies, this cycle contains the same steps, but in reverse order, as the Brayton cycle. A heat exchanger can be included in the RTBC cycle to reduce the required pressure ratio that is necessary to achieve a minimum temperature, particularly at large temperature differences. A simplified T-s diagram of an RTBC cycle is shown in Figure 4.2, alongside with a schematic of the cycle in Figure 4.1.

It is not uncommon for RTBCs to feature multiple compressors in series due to the difficulty of achieving high pressure ratios when compressing helium. To limit the maximum temperature in the cycle, it is possible to have inter-coolers in between the compressor stages. However, for simplicity, only a single heat rejection stage is described here.

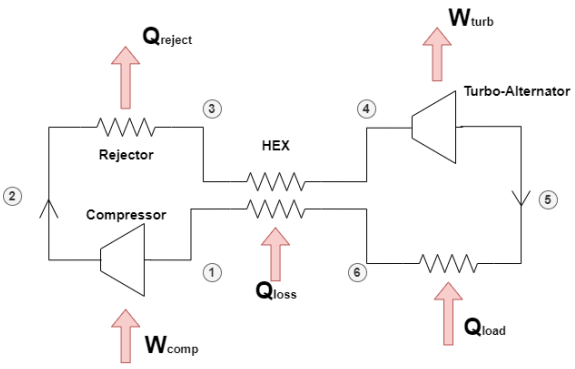


Figure 4.1: Schematic representation of the RTB cycle and its components.

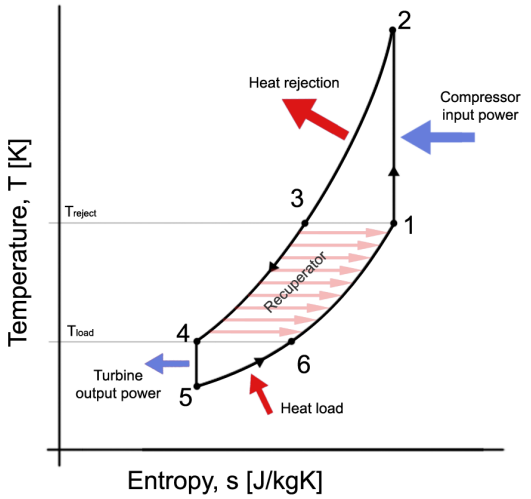


Figure 4.2: Simplified temperature-entropy diagram of an ideal RTB cycle, showing the different energy exchanges with the surroundings and the internal heat transfer of the recuperator.

The power input to drive the compressor is always larger than the heat absorption for RTBCs, especially for those that cool to cryogenic temperatures. This is a consequence of the converging isobaric lines, when decreasing the temperature of a gas. At lower temperatures, the energy that can be extracted from an isentropic pressure difference is smaller than that of the same pressure difference at a higher temperature.

Because the RTB cycle is a closed cycle, it is possible to write an energy balance where energy is entering the system as the compressor power ($\dot{W}_{comp}$), heat leak ($\dot{Q}_{loss}$), and the heat load ($\dot{Q}_{load}$). The energy sources leaving the system are the heat rejection ($\dot{Q}_{reject}$) and the turbine power ($\dot{W}_{turb}$). The energy or power balance then becomes Equation 4.1.

$$\dot{W}_{comp} + \dot{Q}_{loss} + \dot{Q}_{load} = \dot{Q}_{reject} + \dot{W}_{turb} \tag{4.1}$$

## 4.2. Existing RTBCs

Reverse turbo-Brayton coolers have been identified as a solution to cool large volumes such as fuel tanks, where cooling at a distance from the compressor assembly is needed. For such applications, traditional reciprocating cryocoolers (pulse-tube, Stirling, Gifford-McMahon) are difficult to integrate as they primarily provide localized cooling and are typically constrained by the distance between the hot and cold end. Additionally, a single point of cooling inside a fluid tank often experiences significant performance reduction due to temperature stratification. (Radebaugh, 2009)

A notable development of RTBCs for aerospace applications is the work of Zagarola et Al. at Creare Inc. Creare has been at the forefront of RTBC research and has developed the first RTBC for use in space, namely the NICMOS cryocooler that was used onboard the Hubble space telescope. Prior to the installation on the Hubble telescope in March 2002, this RTBC had been flight tested onboard the Space Shuttle in 1998. It could provide a nominal cooling power of 7 W at 80 K, requiring 400 W as input power. Additionally, Creare has been developing new technologies for improved RTBCs, particularly for space applications. Over the last 30 years, a variety of papers has been published by M. V. Zagarola et Al on the applications, design, and testing of reverse turbo-Brayton cryocoolers. Some papers cover the design of individual components of RTBCs, such as the gas bearings (M. V. Zagarola et al., 2019), compressor (Cragin et al., 2020 and Hill et al., 2011), or recuperative heat exchanger (Deserranno et al., 2016 and Hill et al., 2007). Other papers describe the development of RTBCs with different cold end temperatures are described, ranging from 4 K helium coolers up to 90 K Neon coolers (M. V. Zagarola et al., 2003, M. V. Zagarola et al., 2017).

Also the use of two-stage RTBC's for space applications has been explored by M. Zagarola et al., 2009 by development of 60 Kelvin cooler with a 100 K intermediate load, based on the NICMOS cooler. In a later publication, J. Breedlove et al., 2009 explains the testing of a more recent 2-stage RTBC by Creare with a cold end of 10 K.

Apart from the work at Creare, there have been other developments of RTBCs. For example, there are several research papers describing the performance of an RTBC developed in China: Chen et al., 2022, Yang, Fu, Hou, et al., 2019, and Yang, Fu, and Liu, 2019.

Recently, a large RTBC has been developed by Taiyo Nippon Sanso for a high-temperature superconducting cable application. During initial testing, it was capable of providing a 1.35 kW cooling load at 77 K. (K. Lee et al., 2020).

Air Liquide has also been active in the development of RTBCs for industrial applications, with cooling loads in the range of several tens of kW. (Gondrand et al., 2014)

Furthermore, Linde has developed commercial RTBC units for helium refrigeration (e.g. LR1620 and LR1420), albeit using piston compression instead of continuous flow compressors. (Linde, 2019) These cooling units have been used to achieve ZBO and thermal control of a large ground-based liquid hydrogen tank at NASA's Kennedy Space Center using an integrated heat exchanger. (Swanger et al., 2016)

## 4.3. RTBC specific power

There is a lack of literature on the specific power of RTBCs and little information on the sensitivity of an RTBC's mass with respect to their performance. Berg et al., 2015 collected specific power data on several RTBCs and proposed a correlation of the RTBC mass ($m$) as function of the compressor input power, shown in Equation 4.2. This correlation was however based on only 7 data points, of which 4 featured an input power equal or less than 400 W. Regardless of the data size, Berg et al., 2015 confirm that the specific power of RTBCs noticeably decreases with increasing input power. The study by Berg et al., 2015 is a clear example of the need for an in-depth study on the sensitivity of RTBCs' mass (or specific power) to its performance, and the performance of its components.

$$m_{RTBC} = 27.5 \cdot exp(-1.225 \cdot log_{10}(P_{comp})) \tag{4.2}$$

## 4.4. RTBC efficiency

The coefficient of performance of an RTBC is defined in the same way as any other cryocooler, namely by dividing the heating power by the input power (see subsection 3.3.1).

$$COP = \frac{\dot{Q}_{load}}{\dot{W}_{comp}} \tag{4.3}$$

Sometimes the turbine power of an RTBC is partially recovered, making it a turbo-alternator, reducing the net input power that has to be provided to the cryocooler. The turbine power is however only a relatively small fraction of the compressor input power as a consequence of the converging isobaric lines when decreasing the temperature of a gas. Assuming that all the turbine power goes to the compressor, Equation 4.3 can be rewritten to Equation 4.4.

$$COP = \frac{\dot{Q}_{load}}{\dot{W}_{comp} - \dot{W}_{turb}} \tag{4.4}$$

The useful power from the turbo-alternators is often so small compared to that of the compressor, that instead of connecting it to the compressor, it is used to power the electronics that control the RTBC instead. For the analytical performance analysis below, the turbine power is omitted from Equation 4.4, as it is assumed to power the electrical systems associated with the RTBC and not provide any reduction in net input power.

### 4.4.1. Derivation of analytical RTBC COP

It is possible to write the RTBC's coefficient of performance in function of several useful cycle variables such as the cycle pressure ratio ($PR$), heat rejection temperature ($T_{reject}$), cold load temperature ($T_{load}$), recuperator effectiveness ($\epsilon_{rec}$), aftercooler effectiveness ($\epsilon_{reject}$), turbine and compressor effectiveness ($\eta_{comp}$ and $\eta_{turb}$ respectively), and fluid properties. Several assumptions have to be made for this simplified analytical model: no pressure drop due to friction, no parasitic heat loads from the environment, and a fluid property evaluation only at two discrete points in the cycle.

First the heat load of the cycle can be expressed as the the multiplication of the thermal capacitance ($C = \dot{m} \cdot c_p$) with the temperature difference between points 5 and 6. Additionally, the compressor power can be expressed as the thermal capacitance multiplied with the temperature difference over the compressor, between points 1 and 2. Not taking into account the turbine recuperation, the COP can be expressed as Equation 4.6. Note that a discrete distinction is made between the heat capacity at constant pressure for the hot side ($c_{p,H}$) and the cold side ($c_{p,C}$) of the cycle.

$$COP = \frac{\dot{m} \cdot c_{p,C} \cdot (T_6 - T_5)}{\dot{m} \cdot c_{p,H} \cdot (T_2 - T_1)} \tag{4.5}$$

The temperature difference over the compressor can be expressed in terms of the compressor pressure ratio ($PR$), compressor isentropic efficiency ($\eta_{comp}$) and the specific heat ratio at the hot end of the cooler ($\gamma_H$).

$$COP = \frac{c_{p_C}}{c_{p_H}} \cdot \frac{[T_6 - T_5]}{\frac{T_1}{\eta_{p_C}} \cdot \left[PR^{\frac{\gamma_H - 1}{\gamma_H}} - 1\right]} \tag{4.6}$$

or

$$COP = \frac{c_{p_C}}{c_{p_H}} \cdot \frac{\eta_{comp}}{\left[PR^{\frac{\gamma_H - 1}{\gamma_H}} - 1\right]} \cdot \frac{T_6 - T_5}{T_1} \tag{4.7}$$

The effectiveness of the recuperator can be included in the expression for the RTBC's coefficient of performance.

$$\epsilon_{recup} = \frac{\dot{Q}_{recup}}{\dot{Q}_{recup,max}} \tag{4.8}$$

Knowing that the mass flow rates on both sides of the recuperator are equal and assuming an average heat capacity at constant pressure for both fluid streams, means that the recuperator can be assumed to be perfectly balanced. Therefore the effectiveness can be expressed simply by the temperature difference experienced by one of the fluids, divided by the maximum temperature difference in the recuperator, as shown in Equation 4.9.

$$\epsilon_{recup} = \frac{T_3 - T_4}{T_3 - T_6} = \frac{T_1 - T_6}{T_3 - T_6} \tag{4.9}$$

From this effectiveness, it is possible to write an expression for $T_1$, as shown in Equation 4.10.

$$T_1 = \epsilon_{recup} \cdot (T_3 - T_6) + T_6 \tag{4.10}$$

Substituting Equation 4.10 into Equation 4.7, gives:

$$COP = \frac{c_{p_C}}{c_{p_H}} \cdot \frac{\eta_{comp}}{\left[PR^{\frac{\gamma_H - 1}{\gamma_H}} - 1\right]} \cdot \frac{T_6 - T_5}{\epsilon_{recup} \cdot (T_3 - T_6) + T_6} \tag{4.11}$$

The isentropic correlations can be used to correlate $T_5$ to $T_4$ using the isentropic efficiency of the turbine in combination with the pressure ratio, being the same to that of the compressor as pressure losses are neglected.

$$T_5 = T_4 \cdot \left[1 - \eta_{turb} \cdot \left(1 - \frac{1}{PR^{\frac{\gamma_C - 1}{\gamma_C}}}\right)\right] \tag{4.12}$$

Here $T_4$ can be substituted by an expression from the recuperator effectiveness equation, Equation 4.9, leading to Equation 4.13.

$$T_5 = \left(T_3 - \epsilon_{recup} \cdot (T_3 - T_6)\right) \cdot \left[1 - \eta_{turb} \cdot \left(1 - \frac{1}{PR^{\frac{\gamma_C - 1}{\gamma_C}}}\right)\right] \tag{4.13}$$

Combining Equation 4.12 and Equation 4.11, gives an expression of the RTBC's COP as function of $T_3$, $T_6$, cycle pressure ratio $PR$, and the performance parameters of the different components of the RTBC.

$$COP = \frac{c_{p_C}}{c_{p_H}} \cdot \frac{\eta_{comp}}{\left[PR^{\frac{\gamma_H - 1}{\gamma_H}} - 1\right]} \cdot \frac{T_6 - \left(T_3 - \epsilon_{recup} \cdot (T_3 - T_6)\right) \cdot \left[1 - \eta_{turb} \cdot \left(1 - \frac{1}{PR^{\frac{\gamma_C - 1}{\gamma_C}}}\right)\right]}{T_6 + \epsilon_{recup} \cdot (T_3 - T_6)} \tag{4.14}$$

**Derivation of $T_3$**

Because the assumption was made that the heat exchanger on the cold end has 100% effectiveness, $T_6$ is equal to the heat load temperature $T_{load}$. However $T_3$ is not equal to the heat rejection temperature, as the aftercooler effectiveness is less than 100%. Therefore an expression (Equation 4.17) for $T_3$ is derived, which could be substituted in Equation 4.14. First, $T_3$ can be expressed in terms of $T_2$ and $T_{reject}$ using the expression for the aftercooler effectiveness (Equation 4.15).

$$\epsilon_{reject} = \frac{\dot{Q}_{reject}}{\dot{Q}_{reject,max}} \tag{4.15}$$

Assuming that the helium stream inside the RTBC has a lower capacitance than the external air that receives heat from the aftercooler, the aftercooler's effectiveness ($\epsilon_{reject}$) can be expressed and simplified using Equation 4.16. Here $\dot{m}$ and $c_{p_H}$ refer to the mass flow rate of the helium flow, not that of the cooling air.

$$\epsilon_{reject} = \frac{\dot{m} \cdot p_H \cdot (T_2 - T_3)}{\dot{m} \cdot p_H \cdot (T_2 - T_{reject})} = \frac{T_2 - T_3}{T_2 - T_{reject}} \tag{4.16}$$

Thus:

$$T_3 = \epsilon_{reject} \cdot T_{reject} + T_2 \cdot (1 - \epsilon_{reject}) \tag{4.17}$$

Secondly, $T_2$ can be expressed in terms of $T_1$ using the compressor's isentropic compression definition and the isentropic correlations, yielding Equation 4.18.

$$T_2 = T_1 \cdot \left[1 + \frac{1}{\eta_{comp}} \cdot \left(PR^{\frac{\gamma_H - 1}{\gamma_H}} - 1\right)\right] \tag{4.18}$$

Combining the expression for $T_2$ (Equation 4.18) with the earlier found expression for $T_1$ (Equation 4.10), yields:

$$T_2 = (\epsilon_{recup} \cdot (T_3 - T_6) + T_6) \cdot \left[1 + \frac{1}{\eta_{comp}} \cdot \left(PR^{\frac{\gamma_H - 1}{\gamma_H}} - 1\right)\right] \tag{4.19}$$

Finally, an expression of $T_3$ can be created in function of $T_6$, being the heat load temperature in this simplified model, by substituting Equation 4.19 into Equation 4.17.

$$T_3 = \epsilon_{reject} \cdot T_{reject} + (\epsilon_{recup} \cdot (T_3 - T_6) + T_6) \cdot \left[1 + \frac{1}{\eta_{comp}} \cdot \left(PR^{\frac{\gamma_H - 1}{\gamma_H}} - 1\right)\right] \cdot (1 - \epsilon_{reject}) \tag{4.20}$$

Rewriting this expression to isolate $T_3$ on one side of the equation, yields:

$$T_3 = \frac{\epsilon_{reject} \cdot T_{reject} + T_6 \cdot (1 - \epsilon_{recup}) \cdot (1 - \epsilon_{reject}) \cdot \left[1 + \frac{1}{\eta_{comp}} \cdot \left(PR^{\frac{\gamma_H - 1}{\gamma_H}} - 1\right)\right]}{1 - \epsilon_{recup} \cdot (1 - \epsilon_{reject}) \cdot \left[1 + \frac{1}{\eta_{comp}} \cdot \left(PR^{\frac{\gamma_H - 1}{\gamma_H}} - 1\right)\right]} \tag{4.21}$$

---

**Derivation of $T_6$**

Together, Equation 4.14 and Equation 4.21 express the RTBC's COP in function of the component performances and the heat rejection temperature. However the performance of the heat exchanger at the heat load is not yet incorporated into the analytical model. The temperature at station 6 ($T_6$) is not exactly equal to the load temperature, except in case of a 100% effective load heat exchanger. The effectiveness of the load heat exchanger ($\epsilon_{load}$) can be expressed using Equation 4.22.

$$\epsilon_{load} = \frac{T_6 - T_5}{T_{load} - T_5} \tag{4.22}$$

$$T_6 = \epsilon_{load} \cdot T_{load} + (1 - \epsilon_{load}) \cdot T_5 \tag{4.23}$$

The earlier derived equation for $T_5$ (Equation 4.13) can be combined with Equation 4.23, yielding Equation 4.24.

$$T_6 = \epsilon_{load} \cdot T_{load} + (1 - \epsilon_{load}) \cdot \left(T_3 - \epsilon_{recup} \cdot (T_3 - T_6)\right) \cdot \left[1 - \eta_{turb} \cdot \left(1 - \frac{1}{PR^{\frac{\gamma_C - 1}{\gamma_C}}}\right)\right] \tag{4.24}$$

By combining the expression for $T_3$ (Equation 4.21) and $T_6$ (Equation 4.24), it is possible to create an expression for $T_6$ that is independent of $T_3$ and any other temperature in the cycle:

$$\begin{cases} T_6 = \dfrac{\epsilon_{load} \cdot T_{load} + A/C}{1 - \epsilon_{rec} \cdot (1 - \epsilon_{load}) \cdot \left[1 - \eta_{turb} \cdot \left(1 - \frac{1}{PR^{\frac{\gamma_C - 1}{\gamma_C}}}\right)\right] - B/C} \\ A = T_{reject} \cdot \epsilon_{rej} \cdot (1 - \epsilon_{load}) \cdot (1 - \epsilon_{recup}) \cdot \left[1 - \eta_{turb} \cdot \left(1 - \frac{1}{PR^{\frac{\gamma_C - 1}{\gamma_C}}}\right)\right] \\ B = (1 - \epsilon_{load}) \cdot (1 - \epsilon_{recup})^2 \cdot (1 - \epsilon_{reject}) \cdot \left[1 - \eta_{turb} \cdot \left(1 - \frac{1}{PR^{\frac{\gamma_C - 1}{\gamma_C}}}\right)\right] \cdot \left[1 + \frac{1}{\eta_{comp}} \cdot \left(PR^{\frac{\gamma_H - 1}{\gamma_H}} - 1\right)\right] \\ C = 1 - \epsilon_{recup} \cdot (1 - \epsilon_{load}) \cdot \left[1 - \eta_{turb} \cdot \left(1 - \frac{1}{PR^{\frac{\gamma_C - 1}{\gamma_C}}}\right)\right] \end{cases} \tag{4.25}$$

### 4.4.2. Discussion of analytical RTBC COP

Equation 4.14, together with the analytical expression for $T_3$ (Equation 4.21) and $T_6$ (Equation 4.25), provides an approximation of the RTBC's coefficient of performance based on the heat load temperature $T_{load}$, heat rejection temperature $T_{reject}$, pressure ratio $PR$, turbomachinery isentropic efficiencies ($\eta_{comp}$ and $\eta_{turb}$), recuperator effectiveness $\epsilon_{recup}$, aftercooler effectiveness $\epsilon_{reject}$, load HEX effectiveness $\epsilon_{load}$, and fluid properties evaluated at the cold and hot end of the cycle. Friction losses, and heat losses are all neglected for this analytical model. Taking into account any of these phenomena would make this analytical equation unpractical to use or it would have to be solved numerically, defeating the purpose of this simplified model.

These equations can be simplified to arrive at the same equation for the percentage of Carnot efficiency that is proposed by M. Zagarola et al., 2014, which can be seen in Equation 4.26. Zagarola's equation assumes a 100% effective recuperator, 100% effective aftercooler, 100% effective load HEX, and constant fluid properties. It does however take into account a heat leak into the recuperator using a non-dimensional expression $\beta$, being the heat leak divided by the turbine output power. When simplifying Equation 4.14 and Equation 4.21 using the same assumptions from Zagarola and setting $\beta$ equal to zero in Equation 4.26, both equations give the exact same expression and results.

$$COP = \eta_{comp} \cdot \eta_{turb} \cdot (1 - \beta) \cdot \frac{1}{PR^{\frac{\gamma - 1}{\gamma}}} \cdot \left(1 - \frac{T_{load}}{T_{reject}}\right) \cdot \eta_{carnot} \tag{4.26}$$

The solution of the analytical model for the COP can be plotted as a function of the pressure ratio of the cycle. Therefore, a case is set up using inputs representative to those of an RTBC for the cooling of a liquid hydrogen tank onboard an aircraft:

- $T_{load}$ = 20 K
- $T_{reject}$ = 250 K
- $\eta_{comp}$ = 0.75
- $\eta_{turb}$ = 0.85
- Fluid properties on the hot side evaluated at 250 K and 20 bar
- Fluid properties on the cold side evaluated at 20 K and at 20 bar divided by the pressure ratio

In case of a 80% aftercooler effectiveness and 80% heat load HEX effectiveness, the results for a varying recuperator effectiveness can be seen in Figure 4.3 and Figure 4.4, for the COP and percentage of Carnot efficiency respectively.

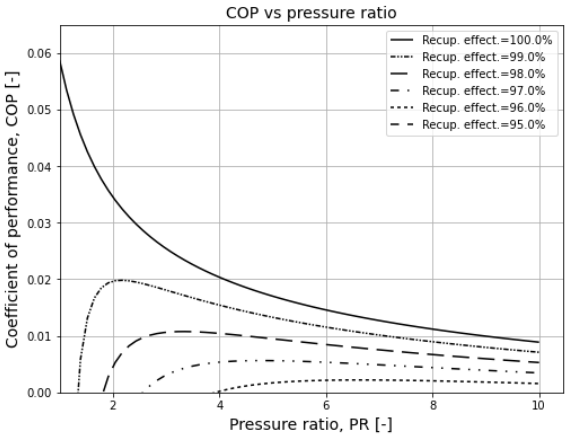


Figure 4.3: Analytical solution for the COP as function of the RTBC pressure ratio and recuperator effectiveness in case of an 80% effective aftercooler and an 80% effective load heat exchanger.

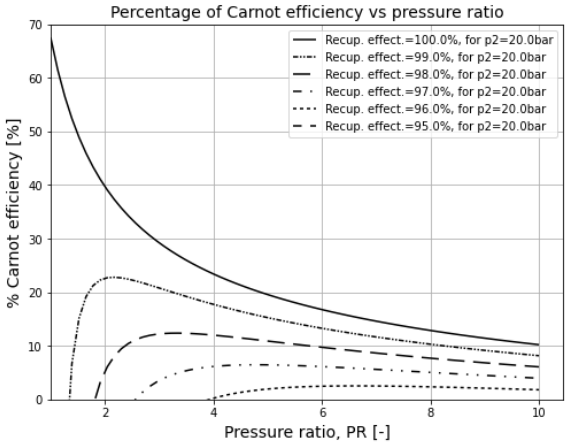


Figure 4.4: Analytical solution for the percentage of Carnot efficiency as function of the RTBC pressure ratio and recuperator effectiveness in case of a 80% effective aftercooler and 80% effective load heat exchanger.

In case of a 98% recuperator effectiveness and 80% heat load HEX effectiveness, the results for a varying aftercooler effectiveness can be seen in Figure 4.5 and Figure 4.6, for the COP and percentage of Carnot efficiency respectively.

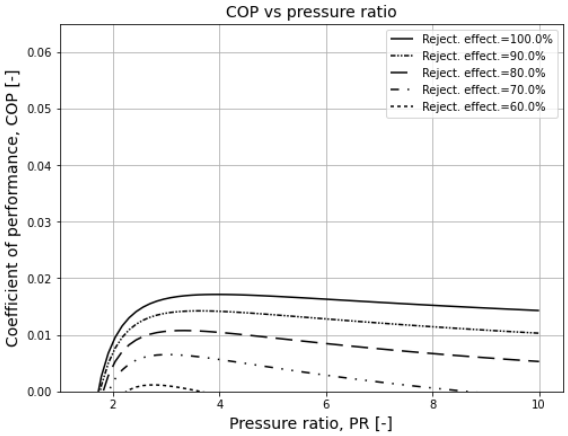


Figure 4.5: Analytical solution for the COP as function of the RTBC pressure ratio and aftercooler effectiveness in case of an 98% effective recuperator and an 80% effective load heat exchanger.

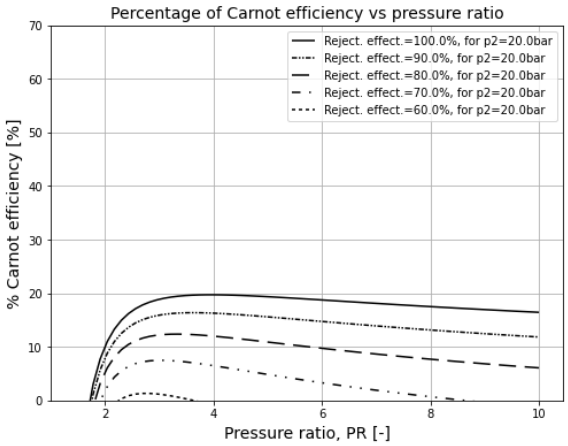


Figure 4.6: Analytical solution for the percentage of Carnot efficiency as function of the RTBC pressure ratio and recuperator effectiveness in case of a 98% effective recuperator and 80% effective load heat exchanger.

In case of a 98% recuperator effectiveness and 80% aftercooler effectiveness, the results for a varying heat load effectiveness can be seen in Figure 4.7 and Figure 4.8, for the COP and percentage of Carnot efficiency respectively.

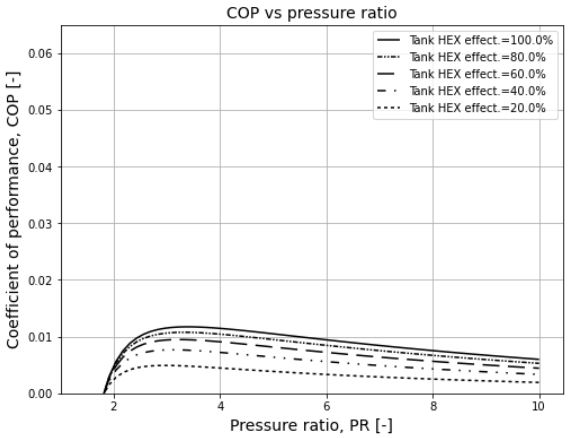


Figure 4.7: Analytical solution for the COP as function of the RTBC pressure ratio and load HEX effectiveness in case of an 98% effective recuperator and an 80% effective aftercooler.

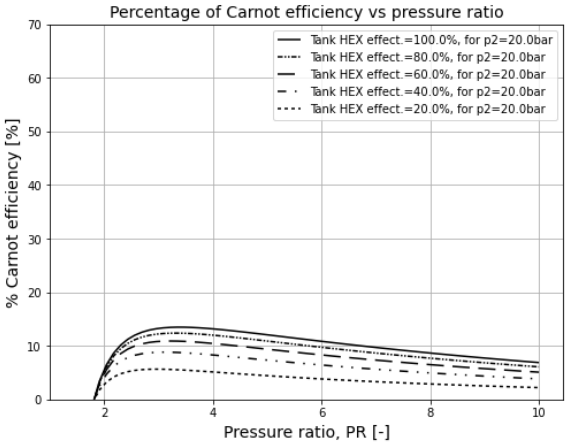


Figure 4.8: Analytical solution for the percentage of Carnot efficiency as function of the RTBC pressure ratio and load HEX effectiveness in case of a 98% effective recuperator and 80% aftercooler.

**Discussion**

From the graphs above, it is clear to see that in case of a 100% effective recuperator, RTBCs are more energy efficient for lower pressure ratios, which can also be observed from Zagarola's equation (Equation 4.26). However, with a decreasing recuperator effectiveness, the COP does not only decrease, but also becomes negative at very low pressure ratios, meaning that the cycle doesn't reach below the load temperature $T_{load}$. For non-perfect recuperators, the analytical solution shows that there is an optimum pressure ratio to maximize the RTBC's efficiency, both in terms of COP and percentage of Carnot efficiency. Lower recuperator effectiveness values will require higher pressure ratios to achieve cooling at the target temperature. These results highlight the importance of a high recuperator effectiveness towards RTBC efficiency.

The ineffectiveness of the aftercooler also has a noticeable influence on the RTBCs performance, however to a lesser degree as the recuperator, as can be seen from the graphs in Figure 4.5 and Figure 4.6. At reduced aftercooler effectiveness values, the performance decrease particularly at high pressure ratios. This can be explained by the fact that higher pressure ratios will result in a higher cycle peak temperature ($T_3$). For high pressure ratios, the larger temperature difference between point 3 and the environment will therefore also increase the temperature of point 4, which on its turn increases the temperature difference that the recuperator experiences.

Ineffectiveness of the tank heat exchanger in the RTBC seems to have the smallest influence on its coefficient of performance. For the cases shown in Figure 4.7 and Figure 4.8, tank HEX effectiveness values of 20% and lower still resulted in positive COP values. Although not shown in these graphs, the effectiveness of the tank HEX does have a significant influence on the mass flow rate of the helium working fluid, which on its turn affects the pressure drop and mass of the different RTBC components.

The results from this analytical study show that the performance of an RTBC strongly depends on the combination of pressure drop and recuperator effectiveness. Generally, lower pressure ratios result in a higher efficiency, as long as the effectiveness of the recuperator is high enough to guarantee sufficient temperature difference between the load temperature and the coldest point in the cycle ($T_5$).

The loss sources that were neglected in this simplified model are still relevant for the RTBC design as they are expected to have a significant influence on the COP. Additionally, the weight or specific

power of the RTBC is another critical aspect that should be considered, especially as the high effectiveness of the recuperator can be a significant contribution towards the RTBC's mass. Therefore the current study will focus on the development of a numerical tool that computes the performance parameters and mass of an RTBC for a set of given inputs, and in particular the contribution of the recuperator. The research question and scope of this study is explained in more detail in chapter 6.

# 5

# Heat exchangers

As the name implies, heat exchangers are made to transfer as much heat as possible between two media, often two fluid streams. This chapter aims to shed light on the functionality, modeling techniques, and current developments of heat exchangers, with a focus on the HEXs of reverse turbo-Brayton cryocoolers. Much of the information provided in this section comes from the detailed HEX design handbook from Shah and Sekulić, 2003, named ”Fundamentals of Heat Exchanger Design”. Additionally, most information presented here on the fundamentals of heat transfer (see subsection 5.2.1) comes from the book ”Basic heat and mass transfer” by Mills, 2013.

A general description of how heat exchangers can be classified is presented in section 5.1. Thereafter, in section 5.2, an overview of the modeling techniques used for heat exchanger simulations is provided. Finally, a brief discussion on the cryocooler applications of heat exchangers is covered in section 5.3.

## 5.1. Classification of heat exchangers

There are many ways to categorise heat exchangers, based on the relative flow direction, geometry, fluid phases, functionality, fluid mixing, ... In this section, a comprehensive summary is provided on the different types of heat exchangers that currently exist and how these compare to each other. This work is limited to heat exchangers with two fluid streams and excludes boilers and condensators.

### Recuperators and regenerators

First, the difference between recuperators and regenerators is addressed. The former involves two separated streams of fluid that continuously exchange energy through a solid medium such as a separating wall or tube. Regenerators features only a single flow path containing a porous structure with a high thermal capacity. A hot or cold fluid alternatingly flows over this structure in order to exchange heat with the porous structure. Regenerators rely on the thermal capacitance and thermal inertia of the porous structure in the flow path to exchange heat with the alternating flow. Because the thermal capacity of most materials is proportional to the temperature, regenerators tend to be less effective at low cryogenic temperatures.

### Flow direction

A major distinction of recuperators can be made regarding the relative direction of the fluid streams. Generally three type can be identified: co-current flow, counter-current flow, and cross-flow. In co-current flows, the two streams travel in the same direction, while in the counter-current case they flow in opposite directions. In case of cross-flow, the fluid streams are perpendicular to each other. These distinctions are however a generalization, as the flow direction can deviate locally and can be a combination of the above.

For similar operating conditions, counter-flow recuperators are more effective than co-current recuperators, as the flow arrangement allows for a larger temperature difference between either sides of the heat exchanger. In case of a balanced co-current flow recuperators, both fluid streams will tend towards a temperature close to the average between the two inlet flows. While in case of a balanced counter-flow heat exchanger, both fluid streams will tend to approach inlet temperature of the opposite flow. The latter offers a significantly larger potential to transfer heat between the two fluids.

### Fluid phase

Heat exchangers can feature fluids in both gaseous and/or liquid state. Recuperators using liquids in both fluid streams tend to be more compact, as the heat transfer coefficient of a liquid with a wall is generally larger than in case of a gas. Additionally heat exchangers can also feature phase transition, where the fluid will maintain a constant temperature during evaporation or condensation. This isothermal property can be exploited to maintain a larger temperature difference between the fluids throughout the recuperator and thereby increase the heat transfer rate for a given area. Boilers and condensers can also fall in this cathegory.

### Balanced or unbalanced

The balance of a heat exchanger refers to ratio of the heat capacity rate of both fluids. The heat capacity rate (capital $C$) is defined as the heat capacity at constant pressure ($c_p$) multiplied with the mass flow rate ($\dot{m}$) of the fluid, as shown in Equation 5.1. It denotes the energy required to increase the temperature of the fluid mass that flows through a plane during one second by 1 Kelvin.

$$C = c_p \cdot \dot{m} \tag{5.1}$$

When the heat capacity rate of the fluids is equal, the heat exchanger is said to be balanced. The opposite of a balanced heat exchanger is when one of the fluids experiences a phase change all along the heat exchanger, meaning that its heat capacity approaches infinity for this stream. The region where phase transition occurs, the temperature of that fluid will remain roughly constant at the saturation temperature, such as for example in the case of a boiler or condensator.

Practically, no heat exchanger is perfectly balanced, however it is sometimes possible to make this assumption. An example of a balanced heat exchanger is when the fluid is circulated in a closed system, hence the mass flow of both streams are identical, and no significant change in the fluid's heat capacity is experienced. As explained in chapter 2, the latter is however not always the case for cryogenic heat exchangers, as fluid constants can start to deviate at cryogenic temperatures, or close to the critical point.

### Geometry

Heat exchangers come in vastly different shapes, each with distinct advantages and disadvantages, making some heat exchangers more suitable for certain applications than others. The paragraphs below aim to provide the reader with a brief overview of several common types of heat exchangers, their characteristics, and applications. There are however numerous other types of heat exchanger geometries that are not covered in this section for brevity.

### Plate-fin heat exchangers

One of the most common type of heat exchangers is a plate-fin HEX (PFHEX), which is built using a series of parallel plates with fins in between, which fulfil both structural and heat transfer functions. Both fluids flow parallel to the plates in an alternating manner such that the cold fluid neighbours the hot fluid on both sides and vice versa. The overall geometry of a PFHEX is usually rectangular in shape with distribution manifolds for the fluids. This geometry lends itself very well for cross-flow flow arrangements. PFHEXs can be found in all types applications, ranging from car radiators, to industrial heat exchangers, to air conditioning units. A factor that contributes towards the popularity of PFHEXs is the relative ease of manufacturing.

Figure 5.1: Plate fin heat exchangers from SUMALEX, 2023

For PFHEXs, there is a wide range of design options available when it comes to fin geometry to affect the heat transfer and pressure drop performance of the heat exchanger. For example, the fins can be triangular, rectangular, straight, wavy, louvred, perforated, ... Subsequently, there is a significant amount of research dedicated to the thermodynamic and hydraulic characterization of the various fin geometries.

### Stacked plate heat exchanger

Similarly to PFHEXs, plate heat exchangers consist of a series of stacked plates on top of each other, however don't feature any fins. Instead of using fins for enhancing the heat transfer, plate heat exchangers most often include corrugations on the plates to increase the surface area and induce turbulence in the flow, which enhances both mixing and heat transfer efficiency. Plate heat exchangers are frequently used as they are modular, relatively easy to manufacture, and cost-effective. The thermodynamic and hydraulic performance of plate heat exchangers can be tuned by adjusting the geometry of the corrugations and the flow path.

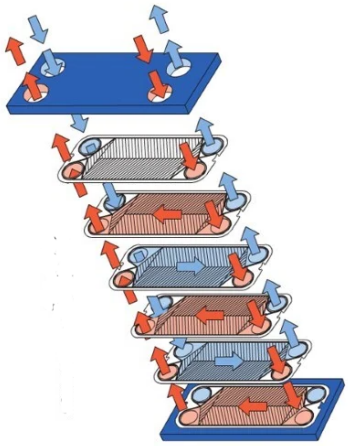

Figure 5.2: Stacked plate heat exchanger diagram by AlfaLaval, 2023

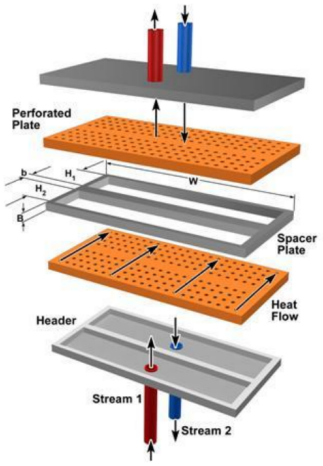


Figure 5.3: Diagram of a perforated plate HEX from Moheisen, 2009

### Perforated plate heat exchangers

As the name implies, perforated plate heat exchangers (also called matrix heat exchangers) consist of a series of stacked plates with cut-outs that allow flow to pass through. The heat transfer between the two fluids happens through in-plane conduction through the plates. Both fluids flow through the stack of plates on their respective side of the heat exchanger. This type of heat exchanger is typically characterized by a high compactness and ease of manufacturing. In contrast to the previously mentioned HEXs, the heat will flow perpendicularly through the plates, however will flow laterally through the metal plates. This means that the thermal conductivity of perforated plate heat exchangers is of particular importance during the material selection process. (Moheisen, 2009)

### Shell-tube heat exchangers

Another one of the more common types of heat exchangers is the shell-tube type, which consists of a cylindrical shell with a network of parallel tubes running inside. One fluid flows through the many tubes after being distributed in a dome, while the second fluid (also known as the shell flow) flows in the cylindrical shell over the tubes. To increase the heat transfer inside the heat exchanger, it is common to install baffles that redirect the shell-side flow such that it flows perpendicularly over the tube bundles. Other common modifications are the use of double- or multi-pass configurations for shell-tube heat exchangers, where the tube- or shell-side flow is redirected such that it passes through the HEX twice or multiple times respectively.

One of the advantages of using a shell and tube heat exchange is its ability to effectively deal with high pressure fluids. In contrast to the PFHEX or plate heat exchanger, most of the geometry consists of cylinders, which are the preferred shape to contain pressurized fluids. Therefore it is more common to us this type of HEX in industrial applications for fluid handling and processing. Shell-tube heat exchangers are however more constly to manufacture and maintain.

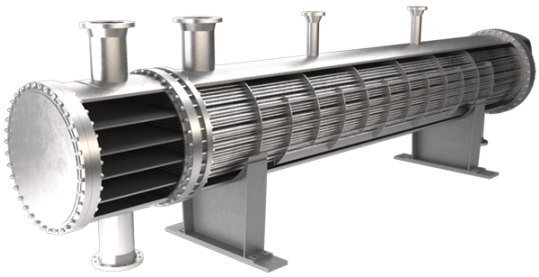

Figure 5.4: Shell and tube heat exchanger model by Aager, 2023

### Coil-wound heat exchangers

Coil-wound heat exchangers (CWHEX), spirally-wound heat exchangers, or Giauque-Hampson heat exchangers are also comprised of an outer shell through which multiple tubes run to exchange heat between the flow in the tubes and the flow in the shell. The main difference with shell-tube heat exchangers is that for CWHEXs the tubes are coiled in spirals around a core or mandrel in the center of the shell. This coiling increases the surface area between the two fluids and thereby enhances the heat transfer rate of the HEX. Typically, each layer of tubes is wound in the opposite direction to improve the heat transfer.

The coiling of the many tubes in CWHEXs makes them relatively expensive and difficult to maintain. One of the advantages of CWHEXs is that there is a long flow path through the tubes, meaning that the effects of differential thermal expansion and axial conduction through the tube walls can be significantly reduced. This makes them particularly useful for applications with large temperature differences such as cryogenics. They are often used in industrial natural gas liquefaction plants. Linde is one of the few companies that makes high-performance CWHEXs at very large scales for LNG plants and has been at the forefront of state-of-the-art CWHEX development (Linde, 2018).

Although CWHEXs already exist for many decades, there has been an increased research effort towards the design and performance evaluation of this type of HEX in recent years due to the increased us of cryogenic fluids as part of the push for an energy transition away from carbon fuel sources.

Figure 5.5: Large coil wound heat exchanger by XuyiTitan, 2023

#### Concentric tube heat exchanger

A concentric tube heat exchanger (also known as tubular heat exchangers or tube-in-tube heat exchangers) is comprised of two tubes, of which one is located inside the other. It is possible for this heat exchanger to include geometrical features that increase the heat transfer between the two fluids, such as the inclusion of fins or corrugations on the inner, outer, or both sides of the separating wall. Alternatively, it is also possible to use a coiled inner tube, non-circular inner tube, or multiple tubes to increase the heat transfer and surface area for a given length.

#### Topology-optimized heat exchangers

The opportunities for the design of complex heat exchanger geometries significantly increased with the advent of additive manufacturing of metals in the last decade. As a consequence, the increased amount of studies and demonstrators for topology-optimized heat exchangers matured this new type of heat exchangers. The large geometrical design freedom of topology-optimized heat exchangers allows for the maximization of the surface area for a given volume and pressure drop of both flows, for example by using 3-dimensional sinusoidal channel walls, also known as gyroids or triply periodic minimal surfaces. (Mahmoud et al., 2023) This leap in manufacturing capabilities has proven to allow for increased heat exchanger compactness, efficiency, and manufacturing cost. However, this technology is currently still limited by the size of metal 3D printing devices.

Figure 5.6: Topology optimized HEX by PTC, Advanced Engineering Solutions, and EOS PTC, 2021

#### Regenerators

Because regenerators are almost exclusively used in reciprocating cryocoolers and not particularly relevant for the use in RTBCs, the different geometrical distinctions for regenerative heat exchangers is not treated here.

## 5.2. Modeling of heat exchangers

This chapter provides an overview of the typical methods that have been used to simulate and model the performance of heat exchangers in general. First an overview of the fundamentals of heat transfer modeling is provided in subsection 5.2.1, where the three modes of heat transfer (conduction, convection, and radiation) are treated, as well as the concept of thermal resistivity. Secondly, subsection 5.2.2 explains the different methods of modeling a heat exchanger in its entirety, including the lumped parameter, distributed parameter, and stream evolution HEX models. Thereafter, subsection 5.2.3 gives an overview of the different performance parameters that can be used to asses a heat exchanger's functionality, followed by subsection 5.2.4 which explains the effect of several loss phenomena that reduce the performance of heat exchangers. This chapter is concluded with a brief overview of what types of heat exchangers have been used in cryocoolers, particularly those in reverse turbo-Brayton cryocoolers in section 5.3.

### 5.2.1. Fundamentals of heat transfer modeling

Generally, heat transfer is modelled with three phenomena: conduction, radiation and convection. Conduction occurs when thermal energy is transfered through an object via the vibration of molecules. Convective heat transfer however, happens via the transport of molecules with different thermal energy from one place to another. Radiative heat transfer is related to the emission and absorption of electromagnetic waves and requires no medium. In this subsection, a brief summary is provided of the typical methods used to model heat transfer between or through media.

The book "Basic Heat and Mass transfer" by Mills, 2013 has been the main reference and source of information for this section.

#### Heat capacity

The thermal or heat capacity ($c$) of a material can be used in unsteady simulations to model the temperature change of matter over time. The discrete change of internal energy ($\Delta Q$) can be written in function of the density ($\rho$), heat capacity ($c$) (or heat capacity at constant pressure ($c_p$) for a gas), and change in temperature.

$$\Delta Q = \rho \cdot c_p \cdot \Delta T \tag{5.2}$$

The time derivative equivalent of Equation 5.2 can be written in Equation 5.3, assuming the density and heat capacity are constant over time. This equation allows one to calculate the change of temperature over time, for a given thermal power, which can be in the form of conduction, radiation, convection, internally generated energy, or a combination of the above. For steady state systems, the right hand side of Equation 5.3 will be equal to zero, meaning that the sum of the thermal power sources will cancel each other out.

$$\dot{Q} = \rho \cdot c_p \cdot \frac{dT}{dt} \tag{5.3}$$

#### Conduction

The most general form of the heat conduction equation is shown in Equation 5.4. It relates the heat flux ($q$) to the thermal conductivity of the material and the temperature gradient.

$$q_{cond} = -k \cdot \nabla T \tag{5.4}$$

In a one dimensional case, Equation 5.5 is commonly used to describe the heat flow through a material with thermal conductivity $k$, at steady state conditions.

$$q_{cond} = -k \cdot \frac{dT}{dx} \tag{5.5}$$

The temperature profile through the material ($dT/dx$) is often not known beforehand. However when assuming steady state conduction through a 1-dimensional homogeneous material, the temperature will have a linear profile, which simplifies Equation 5.5 to Equation 5.6. Here the temperature difference between point 1 and point 2, divided by the distance between the two points ($d$), is used to express the temperature derivative.

$$q_{cond} = -k \cdot \frac{(T_2 - T_1)}{d} \tag{5.6}$$

The thermal energy transfered by conduction ($Q_{cond}$) is then calculated by multiplying the heat flux with the area ($A$) perpendicular to the flux.

$$Q_{cond} = A \cdot q_{cond} \tag{5.7}$$

These conduction equations can be combined with the heat capacity equation to model the transient temperature behaviour of a material. Here the net change of internal energy is substituted with the difference between heat leaving and entering a control volume through conduction. For a one-dimensional

case, this results in Equation 5.8, and for a three-dimensional case with cartesian coordinates x, y, and z, this gives Equation 5.9.

$$\frac{d^2T}{dx^2} \cdot k = \rho \cdot c_p \cdot \frac{dT}{dt} \tag{5.8}$$

$$\left(\frac{d^2T}{dx^2} + \frac{d^2T}{dy^2} + \frac{d^2T}{dz^2}\right) \cdot k = \rho \cdot c_p \cdot \frac{dT}{dt} \tag{5.9}$$

An additional term can be included on the left hand side in case internal heat is generated inside the material. This can be expressed as the rate internal heat generation per unit volume, $\dot{q}_{int}$. In this case, Equation 5.8 will become Equation 5.10.

$$\frac{d^2T}{dx^2} \cdot k + \dot{q}_{int} = \rho \cdot c_p \cdot \frac{dT}{dt} \tag{5.10}$$

When assuming a steady state case and no internal heat generation, the previous equations are reduced to simply the Laplace equation (Equation 5.11.

$$\nabla T = 0 \tag{5.11}$$

## Radiation

When considering two bodies in direct line of sight, both will radiate heat towards each other. The net radiative heat transfer between object 1 and object 2 ($\dot{Q}_{rad,A\to B}$) can be written as shown in Equation 5.12. The viewing factor, $F_{A\to B}$ (radiating from object A to B), is a scaling parameter that is used to indicate how much of body 1 effectively radiates towards body 2. The radiating areas of both objects are denoted with $A$.

$$\dot{Q}_{rad,1\to 2} = A_1 \cdot F_{1\to 2} \cdot E_1 - A_2 \cdot F_{2\to 1} \cdot E_2 \tag{5.12}$$

The emissive power ($E$) is often approximated by assuming that the objects are black bodies. The black body emissive heat flux ($\dot{E_b}$) is a function of the surface temperature to the power of four, as can be seen in Equation 5.13.

$$E_b = \sigma_{boltzmann} \cdot T^4 \tag{5.13}$$

When assuming a grey body model, an object emits radiation with an emissivity factor ($\epsilon$) and absorbs incoming radiation with an absorptivity factor ($\alpha_{surf}$). In such a way, the radiative energy balance of a surface can be expressed in function incoming radiation, called irradiance ($G$), and outgoing radiation, radiance ($J$), as shown in Equation 5.14, assuming the body is non-transparent.

$$E_{rad,net} = \alpha_{surf} \cdot G - \epsilon_{surf} \cdot J = \alpha_{surf} \cdot G - \epsilon_{surf} \cdot E_b \tag{5.14}$$

This relation is often simplified for objects that are placed in an environment with temperature $T_{env}$. The object is assumed to have no effect on the environment, hence the irradiance is purely a function of the environmental temperature, shown in Equation 5.15.

$$E_{rad,net} = \alpha_{surf} \cdot \sigma_{boltzmann} \cdot T_{env}^4 - \epsilon_{surf} \cdot \sigma_{boltzmann} \cdot T_{surf}^4 \tag{5.15}$$

A distinction can be made by discretizing the environmental temperature into different elements, such as for example the sky and the ground, where each has a different temperature. Additionally, there is a variety of modeling efforts on solar irradiance, of which the simplest assumes a constant solar heat flux. More elaborate modeling tools, such as the SMARTS (Simple Model of the Atmoshperic Radiative Transfer of Sunshine) computer model (C. Gueymard, 2006), take more phenomena into account, such as for example atmospheric scattering of light, ground reflectance, and solar emission for different wavelengths.

The black body emissive power ($E$) of a surface is an average of the emissive power of the surface in all wavelengths. The average can be calculated by integration, as shown in Equation 5.16.

$$E_b = \int_0^\infty \frac{dE_b}{d\lambda} \cdot d\lambda \tag{5.16}$$

A body has different emissive power values at different wavelengths ($\lambda$), which is taken into account in Equation 5.16. Additionally, the emissive power of a surface changes according to the cosine law, with regards to the direction it emits to, as shown in Equation 5.17. The angle with respect to a surface's normal vector ($n$) is denoted as $\psi$.

$$E_\psi = E_n \cdot cos(\psi) \tag{5.17}$$

## Convection

Convection is achieved by mass transfer of a fluid over a surface or body. This form of heat transfer can be challenging to model because it is coupled to the fluid dynamics of the medium. A generalized expression for the convective heat transfer towards a surface is shown in Equation 5.18. The convective thermal power ($\dot{Q}_{conv}$) is a function of the exposed surface area ($A$), average heat transfer coefficient ($h_{conv}$), surface temperature, and a reference temperature ($T_{ref}$) that corresponds to that used to calculate the heat transfer coefficient. For internal flows, the reference temperature is often defined as the bulk average temperature of the flow at a specific position.

$$\dot{Q}_{conv} = A \cdot h_{conv} \cdot (T_{surf} - T_{ref}) \tag{5.18}$$

The heat transfer coefficient can be expressed as a function of the fluid thermal conductivity ($k$), the Nusselt number ($Nu$), and a reference length ($x$), that corresponds to the one used to calculate the Nusselt number.

$$h_{conv} = \frac{Nu_x \cdot k}{x} \tag{5.19}$$

The Nusselt number is defined as the ratio of convective to conductive heat transfer of a fluid and is a parameter that is usually retrieved from experiments, empirical relations, or CFD models. Many Nusselt number relations are written as a function of other non-dimensional flow and fluid coefficients, such as the Reynolds number ($Re$), Rayleigh number ($Ra$), and Prandtl number ($Pr$). Nusselt numbers are calculated using a reference dimension ($x$), which should correspond to the same reference length in Equation 5.19. A distinction between forced and natural convection can be made, where the primary method of mass and heat transfer of the former is driven by flow from the surroundings. For natural convection, the temperature difference between the body and the surrounding air causes a density gradient to exist, resulting in a buoyancy-driven flow.

The non-dimensional Rayleigh number ($Ra_x$) is primarily important for natural convection, or also called free convection. It is used as an indication whether the buoyancy-driven flow around a body will be turbulent, laminar, or if there will be no buoyancy driven flow at all, but rather solely conductive heat transfer through the fluid medium. The Rayleigh number is defined as the ratio of the timescale for thermal transport by diffusion and by convection. It can be expressed as the product of the Prandtl ($Pr$) and Grashof ($Gr_x$) non-dimensional numbers, as shown in Equation 5.20.

$$Ra_x = Gr_x \cdot Pr \tag{5.20}$$

The Prandtl number is a non-dimensional fluid property that denotes the ratio of momentum diffusivity and thermal diffusivity of a fluid. It is calculated using the heat capacity at constant pressure ($C_p$), dynamic viscosity ($\mu$), and thermal conductivity of the fluid, as shown in Equation 5.21.

$$Pr = \frac{C_p \cdot \mu}{k} \tag{5.21}$$

The Grashof number is used to denote the ratio of the buoyancy force and the viscous force acting on a fluid. As presented in Equation 5.22, it is calculated using the gravitational constant ($g$), coefficient

of thermal expansion ($\beta$), temperature difference ($\Delta T$) between the surface and a reference temperature (typically the bulk fluid temperature), a characteristic reference dimension ($x$), fluid density ($\rho$), and dynamic viscosity ($\mu$). By providing an indication which of the two forces is dominant, it can be used to determine if the temperature difference between a body and the surrounding air is large enough to induce a flow and thereby also convective heat transfer.

$$Gr_x = \frac{g \cdot \beta \cdot \Delta T \cdot x^3 \cdot \rho^2}{\mu^2} \tag{5.22}$$

In this equation, the thermal expansion coefficient ($\beta$) is defined as the change in volume that results from an increase in temperature of 1 Kelvin, during an isobaric process. The expression of the thermal expansion coefficient in function of the fluid density, and its derivative, can be seen in Equation 5.23).

$$\beta = \frac{-1}{\rho} \cdot \left(\frac{d\rho}{dT}\right)_p \tag{5.23}$$

For ideal gasses, the expansion coefficient is typically approximated by the equation 1/T. This can be demonstrated by substituting the ideal gas equation of state, Equation 2.2, and its derivative $d\rho/dT$ into Equation 5.23.

$$\beta = \frac{-R \cdot T}{p} \cdot \frac{-p}{R \cdot T^2} = \frac{1}{T} \tag{5.24}$$

This approximation generally holds well for gasses at low pressure and at temperatures higher than the critical point. An example of the relationship between the thermal expansion coefficient of Hydrogen as function of temperature and pressure is provided in Figure 5.7. Below 100 K, the expansion coefficient of hydrogen starts to deviate from $1/T$, particularly at higher pressures. Also note that the thermal expansion coefficient will be infinitely large at saturated conditions, which occur below the critical point. Additionally, as one can expect, the ideal gas assumption for the thermal expansion coefficient is not accurate for liquids or supercritical fluids close to the liquid line.

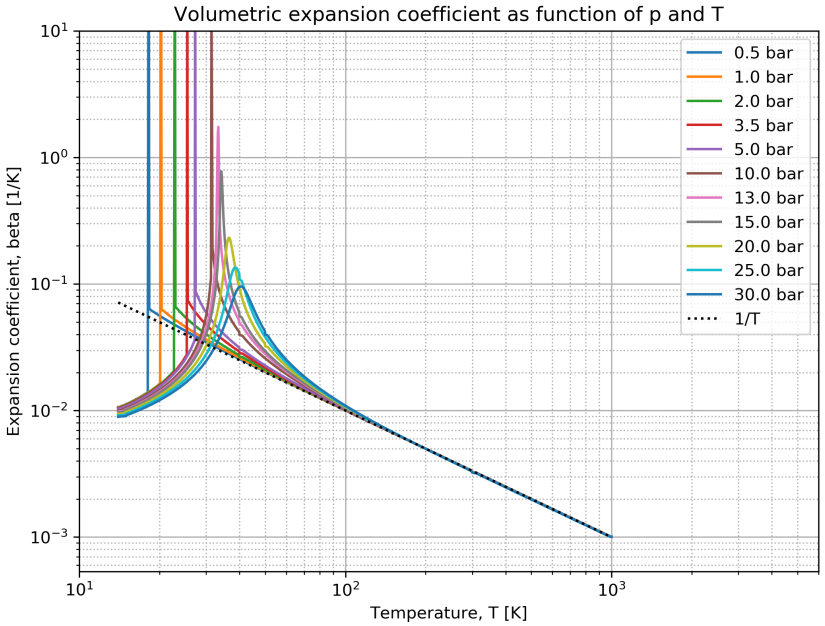


Figure 5.7: Thermal expansion coefficient ($\beta$) of Hydrogen as a function of pressure and temperature. Additionally the ideal gas assumption of $\beta = 1/T$ is included. (Density data was retrieved from NIST, Linstrom and Mallard, 2023)

In order to determine whether the heat transfer of a system is driven primarily by natural convection or by forced convection, the Richardson number ($Ri$) is used. It is defined as the ratio of buoyancy and shear in a flow. It can be calculated with Equation 5.25, or alternatively it is also equal to the Grashof number ($Gr$) divided by the square of the Reynolds number ($Re$). It is however important to use the same reference dimension ($x$) for both Grashof and Reynolds number. If this ratio is close to 1, both natural and forced convection have a roughly equal contribution regarding heat transfer. When $Ri$ is much larger than 1, natural convection is dominant. When $Ri$ is much smaller than 1, forced convection is dominant.

$$Ri = \frac{g \cdot d\rho/dz}{\rho \cdot (dV/dz)} \tag{5.25}$$

$$Ri = \frac{Gr_x}{Re_x^2} \tag{5.26}$$

The Reynolds number is often used to calculate the Nusselt number to calculate the convective heat transfer for forced convective flows. It is defined as the ratio of inertial to viscous forces, and can be expressed in function of the flow velocity ($V$), density ($\rho$), dynamic viscosity ($\mu$), and a reference dimension ($x$), as shown in Equation 5.27. The Reynolds number can be used to characterise the flow behaviour, such as for example whether the flow will be laminar or turbulent. For internal flows, the hydraulic diameter of a channel is typically used for the reference dimension.

$$Re_x = \frac{V \cdot \rho \cdot x}{\mu} \tag{5.27}$$

The Reynolds number is often used in empirical relations together with the Prandtl number to compute the Nusselt number for forced convective flows, similarly to the use of the Grashof and Prandtl number for natural convection.

## Method of resistivity

A method to calculate the heat transfer in a system with radiation, conduction, and convection, is by using the concept of thermal resistivity, which can be considered as an analogue to electrical resistivity. This method is particularly useful in case of complex systems where multiple heat transfer mechanisms are present, for example when both convection, conduction, and radiation take place.

The thermal resistivity ($R$) can be used to calculate the heat transfer ($\dot{Q}$) between two points if the temperature difference is known using Equation 5.28.

$$\dot{Q} = \frac{\Delta T}{R} \tag{5.28}$$

In case there are multiple heat transfer means in series, the total resistivity can be computed simply by taking the sum of the individual resistivities, as shown in Equation 5.29

$$R_{tot} = \sum R_i \tag{5.29}$$

In case there are multiple heat transfer means in parallel, the total resistivity can be computed using the individual resistivities with Equation 5.30.

$$\frac{1}{R_{tot}} = \sum \frac{1}{R_i} \tag{5.30}$$

With these rules, it is possible to solve relatively complex thermodynamic systems by setting up a system of equation using temperature nodes and heat transfer connections using the thermal resistivity. Thereafter, the system of equations can be solved in a similar fashion as is done for electrical systems.

The thermal resistivity of conductive, convective, and radiative heat transfer is calculated using Equation 5.31, Equation 5.32, and Equation 5.33. Here $\Delta x$ represents the distance over which thermal conduction takes place and $A$ represents the heat transfer surface area.

$$R = \frac{\Delta x}{k \cdot A} \tag{5.31}$$

$$R = \frac{1}{h_{conv} \cdot A} \tag{5.32}$$

$$R = \frac{1}{h_{rad} \cdot A} \tag{5.33}$$

Note that the radiative heat transfer coefficient ($h_{rad}$) depends on the temperature difference as well because of its non-linearity, as shown by Equation 5.12. The equivalent radiative heat transfer coefficient for two grey diffuse surfaces (1 and 2) with each their own emissivity can be calculated using Equation 5.34.

$$h_{rad} = \frac{\sigma_{bolzmann} \cdot (T_1^2 + T_2^2) \cdot (T_1 + T_2)}{\frac{1}{\epsilon_{surf,1}} + \frac{1}{\epsilon_{surf,2}} - 1} \tag{5.34}$$

### 5.2.2. Heat exchanger modeling approaches

Many modeling approaches exist to design or evaluate the performance of heat exchangers, with a varying degree of accuracy and computational cost. A classification in three different categories is described by Pacio and Dorao, 2011: lumped parameters, distributed parameters, and stream evolution. Apart from the overview paper by Pacio and Dorao, 2011, the "Fundamentals of Heat Exchanger Design" handbook has been a major source of information that was used to compile this section. An overview of the modeling approaches for each of these three methods is presented in the paragraphs below.

#### Lumped parameter HEX models

The lumped parameter modeling approach is used for the overall performance of a heat exchanger by solving the set of equations (Equation 5.35). Here, the temperature change of the hot and cold flow are expressed in function of the overall heat transfer coefficient ($h_{overall}$), heat transfer area ($A$) and temperature difference between hot and cold flow, denoted with 'h' and 'c' respectively.

$$\dot{m}_c \cdot c_{p,c} \cdot dT_c = h_{overall} \cdot dA \cdot (T_h - T_c) \tag{5.35}$$

$$\dot{m}_h \cdot c_{p,h} \cdot dT_h = h_{overall} \cdot dA \cdot (T_h - T_c)$$

These equations can be solved by integration and defining two parameters. The choice of these parameters is arbitrary for the solution, however some parameters are more useful for certain applications. A list of typical combinations of parameters from Pacio and Dorao, 2011 is provided below:

- $\epsilon$ - $NTU$: The ratio of heat capacity rates ($C^* = C_{min}/C_{max}$) and number of thermal units (NTU) are used to calculate the non-dimensional effectiveness of the heat exchanger ($\epsilon$). Alternatively, the NTU can be calculated from $C^*$ and $\epsilon$.
- $P$ - $NTU$: For both fluid streams, the NTU and heat capacity rate ratio ($R_C = C_1/C_2$) are used to calculate the temperature effectiveness ($P$) of the streams individually. The thermal effectiveness is defined as $P = \dot{Q}/(C \cdot dT_{max})$ and can be related to the HEX effectiveness by $P = \epsilon \cdot C_{min}/C$
- $\Psi$ - $P$: This method is similar to the previous, with the difference that a non-dimensional effective mean temperature difference ($\Psi = \Delta T_m/\Delta T_{max}$) is used, which can be related to the other parameters using $\Psi = \epsilon/NTU$. (Mueller, 1967)

More methods exist that solve the same equations, all with very similar assumptions and results. The use of the lumped parameter modeling approach is however limited to steady state cases where phenomena such as axial conduction, environmental heat losses, flow distribution and varying fluid properties are not taken into account.

The number of transfer units (NTU) in the equations above is a non-dimensional number that describes the heat exchanger's ability to transfer heat from one fluid to the other and can be related to its effectiveness depending on the HEX's configuration.

For lumped parameter HEX models it is common to use the log mean temperature difference (LMTD) instead of the average temperature difference between two fluids, as it more accurately approaches the logarithmic decline in $\Delta T$ between the fluids, especially when the fluids experience a large change in temperature through the HEX. The LMTD is defined by Equation 5.36, where the subscripts 1 and 2 refer to two distinct points in the HEX.

$$LMTD = \frac{\Delta T_1 - \Delta T_2}{ln(\Delta T_1 / \Delta T_2)} \tag{5.36}$$

### Distributed parameter HEX models

In a distributed parameter model, the heat exchanger is divided into distinct segments. Then the lumped parameter model is applied to each of the segments. This allows for a more accurate representation of the changing fluid or flow properties throughout the heat exchanger, which are not captured by the lumped parameter HEX model. This also means that the distributed parameter model is computationally more expensive, as the system of equations has to be solved for each of the segments. (Pacio and Dorao, 2011)

Additionally, the distributed parameter model also lends itself well for modeling heat exchangers with phase change (boilers or condensators), where the fluid and flow properties drastically change between their phase change.

### Stream evolution HEX models

Stream evolution HEX models apply three one-dimensional conservation equations to each fluid stream: mass, energy, and momentum conservation. By doing so, the model takes into account the pressure drops and phase compositions of the streams inside the heat exchanger.

## 5.2.3. Heat exchanger performance parameters

A typical parameter used to express the performance of heat exchangers is the effectiveness, $\epsilon$, which is defined as the actual heat transfer between the two fluids in the heat exchanger, divided by the maximum possible heat transfer between the two fluids. This can be written in terms of the overall heat transfer coefficient ($h_{overall}$), heat transfer area ($A$), average temperature difference over the heat exchanger ($\Delta T_{mean}$), minimum heat capacity rate ($C_{min}$), cold flow inlet temperature ($T_{c,in}$), and hot flow inlet temperature ($T_{h,in}$), as shown in Equation 5.37.

$$\epsilon = \dot{Q} / \dot{Q}_{max} = \frac{h_{overall} \cdot A \cdot \Delta T_{mean}}{C_{min} \cdot (T_{h,in} - T_{c,in})} \tag{5.37}$$

Two alternative heat exchanger performance parameters were proposed by Clayton, 1974: the HEX efficiency ($\eta_{HEX}$) and new effectiveness ($\epsilon_n$). The first is defined as the actual heat transfer rate between the two fluids, divided by the heat transfer rate between the two assuming an infinite specific heat. $\eta_{HEX}$ can be calculated using the heat transfer coefficient ($h_{overall}$), heat transfer area ($A$), average temperature difference over the HEX ($\Delta T_{mean}$), hot flow inlet temperature ($T_{h,in}$), and cold flow inlet temperature ($T_{c,in}$) as shown in Equation 5.38. This equation favours small heat exchangers with small NTUs, as $\eta_{HEX}$ goes to 100% at 0 NTU.

$$\eta_{HEX} = \dot{Q} / \dot{Q}_{c \to \infty} = \frac{h_{overall} \cdot A \cdot \Delta T_{mean}}{h_{overall} \cdot A \cdot (T_{h,in} - T_{c_{in}})} \tag{5.38}$$

The second performance parameter proposed by Clayton is the new effectiveness, $\epsilon_n$. It is defined as the heat transfer rate between the two fluids, divided by the heat transfer rate in case both fluids were allowed to fully mix with each other. It can be calculated using Equation 5.39.An expression of the new effectiveness in terms of the conventional effectiveness is provided in Equation 5.40 This equation is very similar to the standard definition of the HEX effectiveness, however can have values larger than unity, up to a maximum of 2 for counterflow heat exchangers. This performance parameter emphasises the negative effect of heat capacity flow rate imbalances in heat exchangers.

$$\epsilon_n = \dot{Q}/\dot{Q}_{mixed} = \frac{h_{overall} \cdot A \cdot \Delta T_{mean}}{C_{min} \cdot (T_{h,in} - T_{c_i n})/(1 + C^*)} \tag{5.39}$$

$$\epsilon_n = \epsilon \cdot (1 + C^*) \tag{5.40}$$

Apart from the thermodynamic performance of heat exchangers, its volumetric performance can be measured by means of the compactness (also referred to as area density), being the ratio of heat transfer area to the total HEX volume.

Last but not least, the pressure drop of the fluid streams through the heat exchangers is often an equally as important performance parameter as the thermodynamic performance. The pressure drop in a heat exchanger has to be compensated by the compressor or pump that drives the cooling fluid. Simply put, a system that features a heat exchanger with a high pressure drop will either require a more capable pump to achieve the same mass flow rate or will experience a lower mass flow rate for a given pump. The pressure drop of a heat exchanger can dictate the size of a heat exchanger as it is related to the flow velocity, which on its turn is inversely proportional to the flow's crossectional area.

### 5.2.4. Loss sources in heat exchangers

There are several flow phenomena that contribute to performance losses in heat exchangers, such as heat transfer with the environment, longitudinal heat conduction, changing fluid properties along the heat exchanger, and flow maldistribution. The effect of these phenomena on the HEX performance is dependent on the operating conditions and geometry of the heat exchanger. The first three are especially relevant for cryogenic heat exchangers due to the large temperature change experienced by the fluids. In the paper "A review on heat exchanger thermal hydraulic models for cryogenic applications", Pacio and Dorao, 2011 describes the effects of different loss sources on the performance of cryogenic HEXs in more detail. This section provides a brief summary of the loss sources experienced in HEXs and their relevance for cryogenic HEXs specifically.

#### Longitudinal heat conduction

Longitudinal or axial conduction as a loss phenomena refers to the decrease in heat exchanger effectiveness caused by thermal conduction through the solid wall parallel to the flow direction. This The significance of axial conduction is primarily determined by the thermal conductivity of the wall material, length of the conductive heat transfer path (often the HEX length), and the crossectional area for thermal conduction (wall thickness). Additionally, the performance of high effectiveness heat exchangers is affected more strongly compared to those with a lower effectiveness. The effect of axial conduction in co-current flow heat exchangers is typically much less strong than that in counter-flow heat exchangers, especially in case they are well balanced.

Axial conduction will tend to reduce the temperature gradients in the HEX walls and consequently also in the fluid streams. Thereby the heat transfer between the fluids is decreased, resulting in a lower effectiveness. In case of infinite thermal conductivity, the wall temperature will be constant through the heat exchanger, and therefore the effectiveness of such a counter-flow heat exchanger will approach that of a co-current flow.

The boundary conditions of the wall that separates the fluid also have a significant effect on the performance reduction due to axial conduction. For example, the temperature profile of a heat exchanger

will be affected differently by axial conduction if this separating wall has an adiabatic boundary condition instead of a constant temperature boundary conditions. Deciding which boundary condition is the most representative depends on the attachments at the ends of the heat exchanger.

For cryogenic applications, the thermal conductivity of the metal walls can often not be assumed constant as the thermal conductivity drops considerably at lower temperatures, as shown in Figure 5.8.

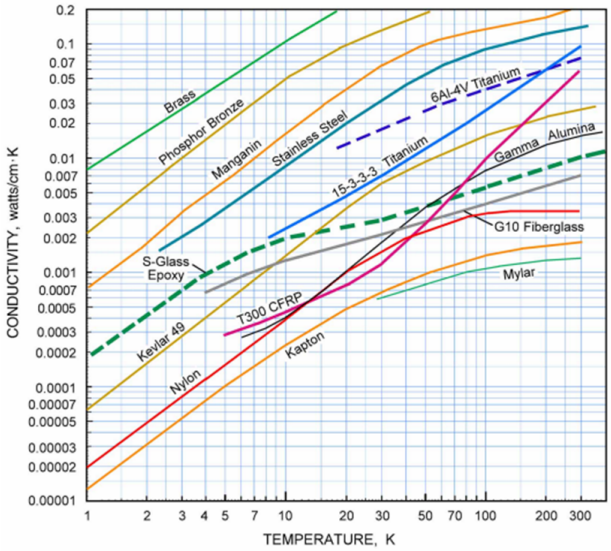


Figure 5.8: Thermal conductivity of several materials at cryogenic temperatures.

## Environmental heat transfer

As the fluid temperature deviates more from the ambient, heat transfer losses associated to environmental heating or cooling affect the performance of the HEX. Heat transfer with the environment generally decreases the potential of the HEX to transfer heat between the two fluids and thereby decreases its effectiveness. The relevance of this effect can be evaluated by comparing the magnitude of the environmental heat transfer to the heat transfer between the two fluids. Heat transfer to the environment is often minimized by using insulation material, particularly for cryogenic or high-temperature applications.

## Change of fluid properties

The fluid properties of the streams in heat exchanger can change significantly when experiencing large temperature changes or when approaching a fluid's vapor dome. The change of fluid properties can on its turn affect the fluid behaviour, and thus affect the heat exchanger's performance. For example, the . This is not always necessarily a loss source, but something to take into account when relevant, particularly for cryogenic heat exchangers. A high effectiveness heat exchanger experiences smaller local temperature differences between the fluids, leading to a smaller local difference of the fluid properties. However the heat exchanger will still be affected by the overall change of fluid properties throughout the heat exchanger. It should also be noted that the change in fluid properties is also coupled to the pressure of the fluids through the HEX, especially when close to the saturation or critical point. The effect of temperature on the fluid properties of several fluids is discussed in more detail in chapter 2.

## Flow maldistribution

The fluids in heat exchangers are nearly never perfectly distributed in a heat exchanger. Variations in hydraulic resistance in sections of the heat exchanger give rise to different mass flow rates and thus different heat transfer rates. This effect reduces the effectiveness of a heat exchanger. This loss phenomenon is difficult to account for in heat exchanger modeling tools as it can require computational fluid dynamics (CFD) simulations to determine the flow maldistribution. For example, the flow maldistribution caused by an asymmetrical inlet manifold is not trivial to quantify using analytical equations.

As stated by Pacio and Dorao, 2011, there are only few existing heat exchanger modeling tools that take this effect into account.

## 5.3. Heat exchangers for cryocoolers

This section provides an overview of the characteristics and type of heat exchangers for cryocooler applications. First, the use of regenerators for cryocoolers is briefly covered in subsection 5.3.1.

### 5.3.1. Regenerators for cryocoolers

Most cryocoolers that use a working fluid, will feature one or more heat exchangers. Reciprocating coolers such as pulse-tube, Stirling, or Gifford-McMahon cryocoolers often make use of aregenerator, that acts as a temporary thermal storage with which the working fluid cyclically interacts. The fluid repeatedly flows through the regenerator in alternating flow directions. Commonly, a fine mesh-type structure is used to maximise the surface area with the fluid. For such regenerative heat exchangers, materials with high heat capacities are desired, to maximise the amount of thermal energy that can be stored in the mesh. The heat capacity of most materials decreases notably at low cryogenic temperatures. This works counter-productive for the efficiency of regenerative cryocoolers at low temperatures.

Due to the cyclic way of operating, regenerators are typically used in reciprocating cryocoolers that rely on a pulsating or cyclic fluid motion, such as Stirling, pulse-tube, and GM coolers. The reduced effectiveness of regenerators at low cryogenic temperatures is the primary reason why pulse-tube, Stirling, and GM coolers are mainly used at higher cryogenic temperatures and have a low performance at lower temperatures, as described in section 5.1 and subsection 3.3.2.

### 5.3.2. Recuperators for cryocoolers

Recuperators on the other hand are often used in cryocoolers that use a continuous cycle, such as reverse turbo-Brayton and Joule-Thompson cryocoolers. The high effectiveness of heat exchangers for cryogenic applications is particularly crucial to achieve large temperature differences between the cold end and hot end of the cryocooler. For example, RTBC recuperator effectiveness values are often in the higher end of the 90 percentages, sometimes even reaching above 99.5% such as the micro-tube shell-tube heat exchanger described by Deserranno et al., 2016, albeit that five recuperators in series were used to achieve this effectiveness.

Multiple types of recuperators have been used for non-reciprocating cryocoolers. Creare, who has been at the forefront of RTBC development for the last decades, has used PFHEXs (J. J. Breedlove et al., 2008), shell-tube HEXs (Deserranno et al., 2016), coil-wound heat exchangers (Christie et al., 2011), and stacked plate radial flow heat exchangers (M. V. Zagarola et al., 2003) in their RTBCs. Additionally, a study by Hill et al., 2007 at Creare focused on the potential of a silicon micro-machined slotted plate heat exchanger as a recuperator for RTBCs, which offer a high compactness for their tactical RTBC application. (M. V. Zagarola et al., 2017)

In a survey on HEX for cryogenics, Qian et al., 2017 noted that the existing RTBCs have primarily used PFHEXs and CWHEXs as recuperators. Examples of plate-fin recuperators in RTBCs are those mentioned by K. Lee et al., 2020 and Yang, Fu, and Liu, 2019 In their study, they emphasized the challenge of dealing with longitudinal conduction in these recuperators due to the large temperature gradients. Careful material selection is key to minimize longitudinal conduction while also maximizing transverse conduction to allow maximal heat transfer between the two fluid streams.

Large-scale coil-wound heat exchangers have been used extensively within the LNG production industry, where Linde has been one of the main commercial providers with an extensive heritage on coil-wound heat exchangers or cryogenics in general. (Linde, 2018)

### 5.3.3. Tank cooling heat exchangers

Multiple studies and technical demonstrations have been conducted on the different approaches to use cryocoolers to cool down the contents of a large tank. For example, the use of reciprocating coolers for

ZBO has been demonstrated by NASA, however is not recommended for large fuel tanks as reciprocating coolers provide localized cooling. (Plachta, 1999, Hastings et al., 2010, and Plachta, 2004) The low thermal conductivity of cryogenic fluids prevent effective temperature diffusion throughout the tank, resulting in temperature stratification. The introduction of a mixer in the tank to prevent stratification would not necessarily be a solution as it will add to the cooling power the cryocooler has to provide. Instead, a distributed cooling system is required to effectively cool the bulk fluid volume, for example using an RTBC. A study by Christie et al., 2011 provides an overview of the methods of cooling a broad area on a fuel tank, primarily by using fluid loops that run along the tank perimeter.

A noteworthy demonstration of cryogenic tank cooling is the IRAS experiment by NASA. An existing 125000 liter liquid hydrogen tank was retrofitted with a distributed heat exchanger in the tank, attached to an RTBC by Linde (Linde, 2019). This set-up was used to test and validate the system's capabilities for zero boil-off, temperature control, and pressure control. The heat exchanger inside the tank consisted of a distributing and collecting manifold that spanned the full length of the almost 20 meter long tank. 40 smaller tubes connected the two manifolds to provide distributed cooling of the liquid hydrogen. Orifices at each tube were installed to prevent flow maldistribution and guarantee a relatively equal mass flow rate through each of the 40 tubes.

### 5.3.4. Cryocooler aftercoolers

Apart from a recuperator and a heat exchanger on the cold end, RTBCs also need an aftercooler to reduce the temperature of the working fluid after the compression stage. The heat that is rejected by the aftercooler is roughly equivalent to the compressor input power, although typically less depending on the ineffectiveness of the aftercooler. This design of this heat exchanger isn't necessarily different from common room-temperature heat exchangers.

The cold stream fluid in the aftercooler is often air, as it is readily available for ground applications. It is however also possible to use a different heat rejection medium, such as for example a liquid nitrogen reservoir to reduce the temperature difference that the RTBC has to achieve.

Heat exchangers have been used on aircraft for a long time, primarily to reject heat from cooling oil that on its turn cools parts of an engine. For this purpose, plate-fin heat exchangers have been most common. By careful design of the inlet, outlet, and geometry of the heat exchanger, it is possible to offset the drag penalty of the heat exchanger by acceleration of the heated flow. This concept is also known as the Meredith effect. An example of the use of an RTBC onboard an aircraft is the onboard air liquefaction device that Creare developed, using a shell-tube ram-air heat exchanger as aftercooler. (J. J. Breedlove et al., 2008)

# 6

# Research scope

The literature study that was summarized in this document, identified a knowledge gap within the scientific community regarding the specific power and performance parameters of a reverse turbo-Brayton cryocooler for airborne applications, particularly to achieve zero boil-off in a liquid hydrogen system. Multiple authors and studies have claimed that RTBCs are the preferred choice of cryocooler to provide the broad area cooling required to achieve ZBO in a large fuel tank. Although ZBO for liquid hydrogen fuel tanks using RTBCs has already been demonstrated on ground systems there is currently no existing cryocooler that, to the author's knowledge, has been designed or optimized for reduced/zero boil-off for an airborne cryogenic fuel tank. Therefore the research question that this study will aim to answer is:

**"What are the expected power density and coefficient of performance for a reverse turbo-Brayton cryocooler for a zero boil-off liquid hydrogen fuel tank onboard a future aircraft?"**

From this research question it is possible to deduce sub-question that will partially answer the main research question. The performance and mass of an RTBC are dependent on those of the RTBC's individual components. The effect of the component performance on the overall RTBC's COP has been identified to some degree using the analytical equation described in this literature study (see subsection 4.4.1). Literature has identified that the recuperator generally is the heaviest component for RTBCs. The contributions of the different components on the mass of an RTBC have however not been quantified. Therefore a sub-question of this study will be: "How sensitive is the mass of an RTBC towards the performance towards its components, being the recuperator, aftercooler, load HEX, compressor, and turbine?"

Because the recuperator is identified to be the heaviest RTBC component, there will be a stronger focus on the development of a heat exchanger model. The relevance of the different loss phenomena in the RTBC recuperator (described in subsection 5.2.4) is to be evaluated, particularly their relevance towards the recuperator mass. Thus the second research sub-question becomes: "What design parameters of a coil-wound heat exchanger have the largest influence on the effectiveness and mass of an airborne RTBC's recuperator?"

A third research question can be formulated based on the performance and mass of a heat exchanger for a distributed cooling system for a liquid hydrogen tank heat exchanger: "How significant is the mass of a distributed cooling heat exchanger for an airborne liquid hydrogen fuel tank towards the total mass of a reverse turbo-Brayton cryocooler?"

Based on these research questions, the scope of this study is defined as:

**"Sensitivity analysis on the specific power and energy efficiency of a reverse turbo-Brayton cryocooler to achieve zero boil-off for an airborne liquid hydrogen fuel tank application**

by

**development of a steady state numerical simulation tool for a reverse turbo-Brayton cycle and its heat exchangers."**

# 7

# Conclusion

Through this literature study, a summary of the key research and technologies of cryogenic fluids and cryocoolers has been presented. The characteristics of helium and hydrogen at cryogenic temperatures were investigated in chapter 2, together with several methods that are used to model the real or ideal fluid properties. Because of its low boiling point, helium was identified to be the most suitable working fluid an a cryocooler to provide cooling inside a liquid hydrogen tank.

In chapter 3, the different types of cryocoolers were described alongside with their typical applications. Cryocoolers have had many applications for ground systems and a reasonable number of space applications in recent decades. However the use of cryocoolers for aircraft and zero boil-off applications has been very limited. Special attention was paid to reverse turbo-Brayton cryocoolers that have a larger potential for broad area cooling of cryogenic fuel tanks compared to reciprocating cryocoolers. A survey of currently available cryocoolers was also performed in chapter 3, which identified the typical operational regimes and conventional performance metrics of several cryocooler types. This review identified the current state-of-the-art percentage of Carnot efficiency for cryocoolers at 20 Kelvin lies below 25%, while the vast majority of coolers achieve less than 10% of Carnot efficiency at this temperature.

The thermodynamic cycle and previously developed reverse turbo-Brayton cryocoolers is discussed in chapter 4 in more detail as this cryocooler cycle will be the main focus of the study. An analytical equation for its coefficient of performance was derived to assess the sensitivity of the cycle's performance to the performance of the individual components. An RTBCs heat exchangers was found to be the largest contribution towards its mass, particularly the high effectiveness recuperator. For this reason, there will be a strong focus on the development of heat exchanger simulation tools during the subsequent study. chapter 5 therefore provides an overview of the different types of heat exchangers that exist and their applications in cryocoolers. Additionally, this chapter provides an overview of the modeling methods that are used to simulate different heat transfer mechanisms and the performance of heat exchangers specifically.

Finally, chapter 6 shows the research questions and topic of the subsequent thesis study.

# Bibliography


Aager. (2023). Heat exchangers [Last retrieved on 10/11/2023]. %5Curl%7Bhttps://aager.de/ergil/heat-exchangers/%7D

AlfaLaval. (2023). Gasketed plate-and-frame heat exchangers [Last retrieved on 10/11/2023]. %5Curl%7Bhttps://www.alfalaval.sg/products/heat-transfer/plate-heat-exchangers/gasketed-plate-and-frame-heat-exchangers/heat-exchanger/how-plate-heat-exchanger-work/%7D

Bar-Cohen, Y. (Ed.). (2016). *Low temperature mechanisms and material, chapter 6: Refrigeration systems for achieving cryogenic temperatures*. CRC press, Boca Raton, FL.

Berg, F., Palmer, P., Miller, P., Husband, M., & Dodds, G. (2015). Hts electrical system for a distributed propulsion aircraft. *IEEE Transactions on Applied Superconductivity*, *Vol.25*(No.3).

Bowman, R. C. (1997). Brilliant eyes ten-kelvin sorption cryocooler experiment (betsce): Final report, pp. 833–839.

Breedlove, J., Cragin, K., & Zagarola, M. (2009). Testing of a two-stage 10 k turbo-brayton cryocooler for space applications. *Cryocoolers*, *Vol.18*.

Breedlove, J. J., Magari, P. J., & Miller, G. W. (2008). Cryocooler for air liquefaction onboard large aircraft. *Advances in cryogenic engineering*, *Vol.33*, pp.838–845. https://doi.org/10.1063/1.2908678

C. Gueymard, S. C. S. (2006). Smarts user manual, version 2.9.5.

Chen, L., Zhang, X., Xiao, R., Zhang, Z., Chen, S., & Hou, Y. (2022). A reverse turbo-brayton cycle cryocooler for zbo storage of liquid hydrogen in space. *Applied Energy Symposium*. https://doi.org/APEN-MIT-2022_7117

Christie, R. J., Tomsik, T. M., Elchert, J. P., & Guzik, M. C. (2011). Broad area cooler concepts for cryogenic propellant tanks. *Thermal Fluids Analysis Workshop*.

Clayton, D. G. (1974). New concepts for heat exchanger performance. *Heat Mass Transfer*, *7*, 107–112.

Collaudin, B., & Rando, N. (2000). Cryogenics in space: A review of the missions and of the technologies. *Cryogenics, Boulder (USA)*, *21*, 797–819.

Cragin, K., McCormick, J., & Zagarola, M. V. (2020). Development of a cryogenic compressor for airborne cryocoolers. *IOP Publishing*. https://doi.org/10.1088/1757-899X/755/1/012032

Cryomech. (2023). Cryomech products [Last retrieved on 10/11/2023]. %5Curl%7Bhttps://bluefors.com/products/cryomech-products/%7D

CryoTel. (2023). Cryotel stirling cryocoolers [Last retrieved on 10/11/2023]. %5Curl%7Bhttps://www.sunpowerinc.com/products/stirling-cryocoolers/cryotel-cryocoolers%7D

Deserranno, D., M., Z., Craig, D., Garehan, R., Giglio, T., Smith, J., Sanders, J., & Day, M. (2016). Performance testing of a high effectiveness recuperator for high capacity turbo-brayton cryocoolers. *Cryocoolers*, *Vol.19*.

Deserranno, D., Zagarola, M. V., Li, X., & Mustafi, S. (2014). Optimization of a brayton cryocooler for zbo liquid hydrogen storage in space. *Cryogenics*, *Vol.64*. https://doi.org/10.1016/j.cryogenics.2014.04.025

Duband, L., Duval, J., & Luchier, N. (2012). Development status of 50 mk hybrid coolers for space applications at cea-sbt. *Cryocoolers*, *Vol.17*, pp.479–486.

ESA. (2017). Zero-boil off propulsion system feasibility demonstration. %5Curl%7Bhttps://www.esa.int/Enabling_Support/Space_Engineering_Technology/Shaping_the_Future/Zero-Boil_Off_Propulsion_System_Feasibility_Demonstration%7D

Estrada-Torres, R. e. A. (2007). Boyle temperatures for pure substances. *Fluid Phase Equilibria*, *258*, 148–154. https://doi.org/10.1016/j.fluid.2007.06.004

Franck, R. A., Gurele, A. P., Brinckerhoff, P. A., McCallan, T. R., & Renbarger, A. A., M. Brown. (2016). High performance cryogenic radiators for james webb space telescope. *International Conference on Environmental Systems, Vienna (Austria)*, *46*.

Friedlander, A., Zubrin, R., & Hardy, T. L. (1991). Benefits of slush hydrogen for space missions [Last retrieved 14/4/2022]. *NASA Technical Memorandum*. https://doi.org/10.18434/T4D303

Gondrand, C., Durand, F., Delcayere, F., Crispel, S., & Gistau Baguer, G. M. (2014). Overview of air liquide refrigeration systems between 1.8 k and 200 k. *Advances in Cryogenic Engineering*, *Vol.13*, pp.949–956. https://doi.org/10.1063/1.4860807

Hastings, L. J., Bryant, C., Flachbart, R., Holt, K., Johnson, E., Hedayat, A., Hipp, B., & Plachta, D. W. (2010). Large-scale demonstration of liquid hydrogen storage with zero boiloff for in-space applications. https://doi.org/NASA/TP—2010–216453

Hastings, L. J., Plachta, D. W., Salerno, S., & Kittel, P. (2002). An overview of nasa efforts on zero boiloff storage of cryogenic propellants. *Cryogenics*, *41*, pp. 833–839.

Hill, R. W., Izenson, M. G., Chen, W. B., & Zagarola, M. V. (2007). A recuperative heat exchanger for space-borne turbo-brayton cryocoolers. *Cryocoolers*, *Vol.14*.

Hill, R., Hilderbrand, J., & Zagarola, M. (2011). An advanced compressor for turbo-brayton cryocoolers. *Cryogenics*, *Vol.16*.

Jha, A. R. (2011). *Cryogenic technologies and applications*. Elsevier.

Jones, J., Bard, S., Schember, H., & Rodriquez, J. (1990). Sorption cooler technology development at jpl. *Cryogenics*, *Vol.30*. https://doi.org/10.1016/0011-2275(90)90084-P

Kimball, M. O. (Ed.). (2014). *Gsfc adiabatic demagnetization refrigerator*. NASA Goddard Space Flight Center, Greenbelt. https://cryo.gsfc.nasa.gov/ADR/ADR.html

Lee, B. I., & Kesler, M. G. (1975). A generalized thermodynamic correlation based on three-parameter corresponding states. *NASA Technical Memorandum*, *21*, 510–527. https://doi.org/10.1002/aic.690210313

Lee, K., Koh, D., Ko, J., Yeom, H., Son, C., & Yoon, J. (2020). Design and performance test of 2 kw class reverse brayton cryogenic system. *Energies*, *Vol.13*. https://doi.org/10.3390/en13195089

LeTehnica. (2022). Study on the coupling characteristics of sub-kelvin sorption cooler and 4 k stirling-type pulse tube cryocooler with small cooling capacity. *Journal of Low Temperature Physics*, *210*, pp.376–392. https://doi.org/10.1007/s10909-022-02894-7

LeTehnica. (2023). Joule-thomson cryogenic cooler [Last retrieved on 10/11/2023]. %5Curl%7Bhttps://cryocoolers.eu/joule-thomson-cryocoolers-fast-cool-down/%7D

Linde. (2018). Experimental turbofan using liquid hydrogen and liquid natural gas as fuel. *AIAA/SAE/ASME/ASEE 26th Propulsion Joint Specialist Conference*. %5Curl%7Bhttps://www.linde-engineering.com/en/images/Coil-wound-heat-exchangers_tcm19-407186.pdf%7D

Linde. (2019). Standard helium refrigerator lr1420/lr1620 [Last retrieved on 7/11/2023]. %5Curl%7Bhttps://www.linde-kryotechnik.ch/wp-content/uploads/2016/10/Datasheet-LR1420-LR1620-Helium-Refrigerator.pdf%7D

Linstrom, P., & Mallard, W. (2023). Nist standard reference database number 69 [Last retrieved 12 Nov 2023]. *NIST Chemistry WebBook*. https://doi.org/10.18434/T4D303

LTL. (2003). Helium. *LTL, Helsinki University of Technology*.

Mahmoud, D., Tandel, S., Yakout, M., Elbestawi, M., Mattiello, F., Paradiso, S., Ching, C., Zaher, M., & Abdelnabi, M. (2023). Enhancement of heat exchanger performance using additive manufacturing of gyroid lattice structures [Last retrieved on 10/11/2023]. *International Journal of Advanced Manufacturing Technology*, *Vol.126*. https://doi.org/10.1007/s00170-023-11362-9

Martin, F., Vermeulen, G., Camus, P., & Benoit, A. (2010). A closed cycle 3he–4he dilution refrigerator insensitive to gravity. *Elsevier Cryogenics*, *50*, 623–627. https://doi.org/10.1016/j.cryogenics.2010.02.014

Melgaard, S. D., Albrecht, A. R., Hehlen, M. P., & Sheik-Bahae, M. (2016). Solid-state optical refrigeration to sub-100 kelvin regime. *Scientific Reports*, *6*. https://doi.org/10.1038/srep20380

Michot Foss, M. (2007). An overview on liquefied natural gas (lng), its properties,organization of the lng industry and safety considerations.

Mills, A. F. (Ed.). (2013). *Basic heat and mass transfer, second edition*. Pearson.

Moheisen, R. M. (2009). Transport phenomena in fluid dynamics: Matrix heat exchangers and their applications in energy systems. *Air Force Research Laboratory*.

Mueller, A. C. (1967). New charts for true mean temperature difference in heat exchangers. *AIChE National Heat Transfer Conference*, *9*.

Mullie, J., Arts, R., Tanchon, J., & Trollier, T. (2016). Lpt 6510 pulse-tube cooler for 60-150 k applications.

NASA. (1978). Liquid hydrogen as a propulsion fuel, 1945-1959. *National Aeronautics and Space Administrations*, *SP-4404*.

Pacio, J. C., & Dorao, C. A. (2011). A review on heat exchanger thermal hydraulic models for cryogenic applications. *Cryogenics*, *51*(7), 366–379. https://doi.org/10.1016/j.cryogenics.2011.04.005

Plachta, D. W. (1999). Hybrid thermal control testing of a cryogenic propellant tank. *Cryogenic Engineering and International Cryogenic Materials Conference*. https://doi.org/NASA/TM-1999-209389

Plachta, D. W. (2004). Results of an advanced development zero boil-off cryogenic propellant storage test. https://doi.org/NASA/TM—2004-213390

Poling, B. E., Prausnitz, J. M., & O'Connel, J. P. (Eds.). (2001). *The properties of gases and liquids, fifth edition*. McGraw-Hill. https://doi.org/10.1036/0070116822

PTC. (2021). Award winning design: Heat exchanger [Last retrieved on 10/11/2023]. *Parametric Technology Corporation*. %5Curl%7Bhttps://www.ptc.com/en/blogs/cad/award-winning-design-heat-exchanger-cool-part%7D

Qian, S., Yu, J., & Yan, G. (2017). A review of regenerative heat exchange methods for various cooling technologies. *Renewable and Sustainable Energy Reviews*, *Vol.69*, pp.535–550. https://doi.org/10.1016/j.rser.2016.11.180

Radebaugh, R. (2009). Cryocoolers: The state of the art and recent developments. *21*(16). https://doi.org/10.1088/0953-8984/21/16/164219

Richards, W. L., Meyer, M. L., Feller, J. R., Rhodes, A. C., Rosner, S., Stefanovic, D., & Kashani, A. (2020). Cryogenic technologies for the stratospheric observatory for infrared astronomy (sofia) science instruments. *NASA Technical Report Server*.

Rosner, S., Helvensteijn, B., Kashani, A., Hofland, L., Wang, J., Pichay, F., Rowan, R., Gee, A., Brown, J., & Risacher, J. (2016). Testing of a closed-cycle cryocooler compressor for deployment aboard sofia aircraft. *International Cryocooler Conference*, *Cryocoolers Vol.19*.

Shah, R. K., & Sekulić, D. P. (Eds.). (2003). *Fundamentals of heat exchanger design*. John Wiley Sons, INC.

Sosounov, V., & Orlov, V. (1990). Experimental turbofan using liquid hydrogen and liquid natural gas as fuel. *AIAA/SAE/ASME/ASEE 26th Propulsion Joint Specialist Conference*.

Stockholm, J. G. (1997). Current state of peltier cooling. *16th International Conference on Thermoelec!rics*. https://doi.org/10.1109/ICT.1997.666972

Strobridge, T. (1974). Cryogenic refrigerators: An updated survey [Last retrieved on 7/11/2023]. *National Institute of Standards and Technology*. https://doi.org/10.6028/NBS.TN.655

SUMALEX. (2023). Plate fin heat exchanger [Last retrieved on 10/11/2023]. *SUMALEX products*. %5Curl%7Bhttps://www.spp.co.jp/netsu/en/products/smalex/%7D

Swanger, A. M., Notardonato, W. U., Johnson, W. L., & Tomsik, T. M. (2016). Integrated refrigeration and storage for advanced liquid hydrogen operations. *NASA Technical Report Server*.

ter Brake, H., & Wiegerinck, G. (2002). Low-power cryocooler survey. *Cryogenics*, *Vol.42*(No.11), pp. 705–718. https://doi.org/10.1016/S0011-2275(02)00143-1

Vidas, L., Castro, R., & Pires, A. (2022). A review of the impact of hydrogen integration in natural gas distribution networks and electric smart grids. *Energies*, *Vol.15*. https://doi.org/10.3390/en15093160

XuyiTitan. (2023). High efficiency spiral coil-wound heat exchanger [Last retrieved on 10/11/2023]. %5Curl%7Bhttps://www.xuyititan.com/product/high-efficiency-spiral-coil-wound-heat-exchanger%7D

Yang, S., Fu, B., Hou, Y., Chen, S., Liu, Z., & Wang, S. (2019). Transient cooling and operational performance of the cryogenic part in reverse brayton air refrigerator. *Energy*, *Vol.167*, pp.921–938. https://doi.org/10.1016/j.energy.2018.11.016

Yang, S., Fu, B., & Liu, Z. (2019). Simulation and evaluation on the dynamic performance of a cryogenic turbo-based reverse brayton refrigerator. *Energy*, *Vol.167*, pp.921–938. https://doi.org/10.1016/j.energy.2018.11.016

Zagarola, M., Desserano, D., Li, X., & Mustafi, S. (2014). Optimization of a brayton cryocooler for zbo liquid hydrogen storage in space. *Cryogenics*.

Zagarola, M. V., Cragin, K., & McCormick, J. (2019). Operation of gas bearings at cryogenic temperatures. *Cryogenics*. https://doi.org/10.1016/j.cryogenics.2019.103001

Zagarola, M. V., Cragin, K., McCormick, J., & Hill, R. (2017). A 4 k tactical cryocooler using reverse-brayton machines. *IOP Publishing*. https://doi.org/10.1088/1757-899X/279/1/012015

Zagarola, M. V., Swift, W. L., Sixsmith, H., McCormick, J. A., & Izenson, M. G. (2003). Development of a turbo-brayton cooler for 6 k space applications. *International Cryocooler Conference*, *Vol.12*. https://doi.org/10.1007/0-306-47919-2_75

Zagarola, M., Breedlove, J., Kirkconnell, C., Russo, J., & Chiang, T. (2009). Demonstration of a two-stage turbobrayton cryocooler for space applications. *Cryocoolers*, *Vol.15*. https://doi.org/10.1.1.629.1103